universität wien

DISSERTATION / DOCTORAL THESIS

Titel der Dissertation / Title of the Doctoral Thesis

„Crystalline supermirrors for infrared applications“

verfasst von / submitted by

Mag. Lukas Perner, BSc

angestrebter akademischer Grad / in partial fulfilment of the requirements for the degree of

Doktor der Naturwissenschaften (Dr. rer. nat.)

Wien, 2023 / Vienna 2023

Studienkennzahl lt. Studienblatt / degree programme code as it appears on the student record sheet:	UA 796 605 411
Dissertationsgebiet lt. Studienblatt / field of study as it appears on the student record sheet:	Physik
Betreut von / Supervisor:	Ass.-Prof. Dipl.-Phys. Dr. Oliver H. Heckl

Preface

> A thesis has to be presentable… but don't attach too much importance to it. If you do succeed in the sciences, you will do later on better things and then it will be of little moment. If you don't succeed in the sciences, it doesn't matter at all.
>
> *(Paul Ehrenfest)*

Like for many doctoral candidates, the path from first setting foot in the lab to finalizing this dissertation was far from direct. It was also a bit longer than anticipated. Initially, I joined the Heckl lab for my diploma thesis, as well as a bachelor's thesis in a non-consecutive curriculum. Instead of leaving academia after successfully concluding my master's, I was offered a doctoral position by my supervisor, which I accepted with enthusiasm.

During this time, I had the opportunity to contribute to many different projects in optics and photonics. These experiments were largely successful and culminated in several publications and subsequent citations. A large part of the experiments on Yb:fiber single and dual-frequency combs and their foundations are detailed at length in Jakob Fellinger's doctoral thesis.

However, my main project during all these years was centered around highly-reflective substrate-transferred crystalline mirrors. While these mirrors had been invented a few years before I joined the research group, I was just in time to join an effort to extend this technology towards the mid-infrared. This provided the perfect environment for graduate student research. As this push for longer wavelengths was a joint effort between academia and industry from the get-go, it exposed me to both a private company and a university research lab. This allowed for a great amount of collaboration, which—among other great things—lead to the invention of a novel coating paradigm, the so-called hybrid mirrors. Gladly, the COVID-19 pandemic eased just in time to allow research visits during my project. These trips took me to Thorlabs Crystalline Solutions in Santa Barbara, California and a facility of the Université de Neuchâtel in Regensdorf, Switzerland. This thesis details the progress of this main effort of my years at the Heckl lab.

Nevertheless, the development of mid-infrared crystalline mirrors is far from completed. The project will continue, and the design and fabrication of hybrid mirrors at wavelengths beyond 7 µm is already underway. I'm looking forward to seeing these efforts bear fruit.

Acknowledgements

First, I would like to thank my supervisor, Oliver H. Heckl, for providing this academic opportunity. The years I spent in his lab were certainly challenging, but even more rewarding. Oliver's guidance, leadership, and support were essential for the success, not only of this thesis, but also of the research group as a whole. His unique style provides the freedom, encouragement, and support to going down the rabbit whole every scientific question seems to be. He also made sure that I would re-emerge with enough concrete answers to write this thesis. This allowed for the challenges I needed to grow and thrive as a researcher and as a human being. Still, I am aware that I owe one crucial apology to my supervisor: Sorry I finished my bachelor's degree before wrapping up my doctorate, Oliver! – I know you would have loved to see me submitting the documents with the *Dr.* already attached to my name. I hope the fact that I wrote a bachelor's, diploma, and now this doctoral thesis under your supervision is a small consolation.

As everything in the Heckl lab is a team effort, these thanks also go to my former and present colleagues at the Christian Doppler Laboratory for Mid-Infrared Spectroscopy and Semiconductor Optics (CDL Mid-IR): Georg, Jakob, Laurin, Aline, Willi, Valentina, Vito, Collin, Dido, Max, Michi, Jonas, and Ulli, as well as all other students, visitors, and collaborators that joined the lab at various stages of my research. The countless times they provided me with scientific and moral support cannot be discounted.

The CDL Mid-IR exposed me to collaborations with brilliant scientists almost from day one. Particularly, I benefited from the expertise of Gar-Wing Truong, Garrett D. Cole, and others at Thorlabs Crystalline Solutions (formerly Crystalline Mirror Solutions). The crystalline mirror project also allowed for two collaborations with the Optical Measurements Group at NIST Gaithersburg. There, especially Adam J. Fleisher and D. Michelle Bailey facilitated the success of the projects presented in this thesis. Last but not least, thanks to Valentin Wittwer at Université de Neuchâtel. Working with him on the hybrid mirrors has been a pleasure. I look forward to collaborations with all of them in anticipation.

Furthermore, I would like to thank my parents, Betina and Wolfgang, as well as their respective partners, Robert and Petra. Their various forms of unwavering support made this dissertation a reality. To all of my friends – thank you for your continued friendship and encouragement along the way.

Finally, my wholehearted thanks go to Melanie, the love of my life. Words cannot express how thankful I am for her support and understanding. She endured, mostly patiently, all the late evenings, weekends, and even holidays I spent working on the results presented in this thesis. I am glad we are on this journey together and I cannot wait for the adventures we will share in the future!

Vienna, September 2023 Lukas W. Perner

Contents

1 Introduction: Advancing mid-infrared optical coatings

Optical coatings, single or multiple layers of material deposited on optical elements, have been instrumental in the evolution of optical technologies. Their ability to tailor the reflection R, transmission T, and absorption A of light at material interfaces, often with minimal scatter S, has been key for enhancing the performance of various modern optical systems.

From their rudimentary beginnings as thin layers of metal on glass to produce simple mirrors, via first scientific exploration in the 18^{th} and 19^{th} century, to modern consumer and scientific use, optical coatings have undergone a transformative evolution [1]. Today, they are used at the forefront of science, with sophisticated multilayer designs being used in high-tech applications in fields as diverse as telecommunications [2], trace gas sensing [3–5], gravitational wave detection [6–10] and white-light generation from blue light-emitting diodes [11–14].

Many of these high-tech optical coatings rely on dielectric rather than metallic thin films. In such designs, many layers of alternating transparent materials are stacked on top of each other to exploit interference effects between reflections at individual material interfaces. These effects are governed by the difference in refractive index among the used materials via the Fresnel equations. As these interference effects rely on superposition of electromagnetic waves, optimal performance—i.e., minimal excess loss $A + S$—is usually achieved with film thicknesses comparable to the design wavelength. Thus, depending on the spectral region, layer thicknesses usually range from tens or hundreds of nanometers (nm) in the visible (VIS) and near-infrared (NIR) to several microns (µm) in the mid-infrared (MIR) for typical designs. Therefore, such multilayers are also known as thin-film coatings. These coatings, in turn, are frequently subdivided in two major categories, anti-reflective (AR) and highly-reflective (HR) coatings [1].

However, not only high-tech applications benefit from a constant evolution of optical coatings. The anti-reflective coatings on eyeglasses, which improve vision by minimizing glare and unwanted reflections, are a testament to the pervasive influence of these coatings in our daily lives [1, 15, 16]. Also, modern photographic objectives, from the smallest smartphone camera to big telezoom lenses, rely on complicated multi-lens assemblies that would suffer from flare without advanced optical coatings [17–20]. So-called *fast lenses*—extremely efficient lenses that allow higher shutter speeds even in challenging light conditions—would hardly be feasible without AR coatings. In fact, AR coatings on camera lenses were one of the first uses of thin-film interference coatings, when Alexander Smakula, then an engineer at Zeiss developed one of the first modern coatings in 1935 [1, 21]. More recently, rapid communication and vast data transfer owes much to optical coatings. They play an indispensable role in fiber optics, ensuring efficient signal transmission and minimizing signal loss, thus keeping the world interconnected [2].

In contrast, Section 2.1 underscores the significance of highly-reflective (HR) optical coatings in scientific applications. Specialized HR coatings optimize the performance of spectroscopic setups such as those in [4, 5, 22–27], enabling accurate monitoring of pollutant levels, atmospheric conditions, and more. As global challenges like climate change take center stage, the ability to detect such minute differences in gas composition becomes paramount.

Furthermore, everything from fundamental physics research to the development of cutting-edge optical clocks benefits immediately from advanced optical coatings. Hence, HR optical coatings are key in a plethora of state-of-the-art applications. Among those is precision interferometry, a technique pivotal for high-resolution measurements in physics. As an example, HR coatings are a vital part of gravitational wave detectors like Advanced LIGO [6], Advanced VIRGO [7], KAGRA [8, 28], or the proposed Einstein telescope [9]. Here, the development of improved HR coatings is a field of vigorous research [10, 29] and paramount for improved sensor performance. This is owing to the fact that the mirrors currently used in the operational facilities, fabricated via traditional ion beam sputtering [30], contribute significantly to the respective overall noise budgets via their excess coating Brownian noise (see, e.g., Fig. 2 in [6] and Fig. 2 in [7]), which is substantially reduced in substrate-transferred crystalline coatings [10, 31].

Still, many of the above uses are well-established only at visible and near-infrared wavelengths. This is also the case for the aforementioned substrate-transferred crystalline mirrors that are in the focus of this thesis. They were initially developed for the NIR region due to their promisingly low Brownian noise for use in reference cavities [31]. Grown on flat gallium arsenide (GaAs) seed wafers via molecular-beam epitaxy [32], these GaAs/$Al_xGa_{1-x}As$ (aluminium gallium arsenide) distributed Bragg reflectors (DBRs, stacks of alternating high-index GaAs and low-index $Al_xGa_{1-x}As$, each with quarter-wave thickness at a certain design wavelength) are transferred to curved optical substrates to facilitate the use in optical cavities. In the NIR, these high-reflector stacks are pivotal in different applications like optical lattice and ion clocks, quantum-limited optical interferometry and ultra-narrow-linewidth laser systems [31]. Also, the feasibility of large-area substrate-transferred crystalline coatings in gravitational wave detectors is actively discussed and explored [10, 29].

More recently, however, the mid-infrared (MIR) range has emerged as a hotbed of scientific and technological innovation. Spanning wavelengths from approximately 2.5 µm to 25 µm, the MIR range is uniquely positioned for a plethora of applications. As elucidated in Sections 2.1, 3.1, and 4.1, this range is significant for fields as diverse as environmental sensing [22, 25, 33, 34], as well as spaceborne [35], earthborne and laboratory astrophysics [3]. This is due to the inherent properties of light in the MIR range, as its resonance with specific molecular vibrations. Part of the MIR spectrum (ca. 6 µm to 20 µm) is even called the molecular fingerprint region [36], as several chemical compounds exhibit characteristic absorption features in this spectral range (mainly due to bending vibrations). As outlined in Chapter 4, also the detection of $^{14}CO_2$, important in the differentiation between biogenic and petrogenic origin of carbon-containing products, is usually done at MIR wavelengths [4, 24, 37]. Many of these applications rely on mid-infrared AR and HR coatings to crucially enhance the throughput and performance of optical systems. This is even more crucial in a wavelength range where high powers in laser sources are traditionally hard to obtain [38, 39]. All of the above applications will benefit immediately from advanced HR coatings with increased reflectivity R while maintaining useful levels of cavity transmission (see Section 2.1 for a detailed discussion). This underscores the importance of the ongoing research into improving optical coatings for this spectral range.

1.1 Challenges for mid-infrared optical coating technologies

While the MIR range is a particularly interesting spectral region for scientific discovery, it comes with several challenges for established optical coating technologies. One major problem is that many materials deposited via traditional physical vapor deposition tech-

niques suffer from excess loss when compared to the VIS and NIR. This prohibits record-high reflectivities—as demonstrated in the VIS and NIR [40–42]— in the MIR with current all-amorphous HR coatings. This includes technologies such as evaporation (electron beam and thermal) or sputtering (e.g., magnetron or ion beam). For example, silica (SiO_2) and tantala (Ta_2O_5)—two low- and high-refractive-index materials widely used in VIS–NIR ion-beam-sputtered coatings—both suffer from excess absorption above ca. 3 µm [43, 44]. Even the choice of substrate material becomes more challenging above ca. 2.6 µm, as many traditional low-index glasses become opaque at or below this wavelength, necessitating the use of (usually higher-index) substrates, e.g. fluorides, silicon (Si), or germanium (Ge).

In contrast to above thin film materials, $Al_xGa_{1-x}As$ demonstrates extremely low losses at wavelengths up to the reststrahlen region (ca. 20 µm in pure GaAs [45, p. 316]). Combined with superpolished monocrystalline silicon substrates, the advantage of GaAs/$Al_xGa_{1-x}As$ multilayers above ca. 2.6 µm is less subtle than the improved Brownian noise in the NIR. In principle, the material system allows for extremely low-loss Bragg mirrors, surpassing the performance of all-amorphous designs substantially in reflectivity R by drastically reducing the absorption A.

The initial foray of substrate-transferred crystalline GaAs/$Al_xGa_{1-x}As$ HR coatings into the mid-infrared is outlined in [46]. In this paper, MBE-grown DBR structures at ca. 3.3 µm and ca. 3.7 µm were presented. These mirrors, by design, allowed only for a moderate finesse of 10 700 and 4110, respectively. Still, due to their low excess loss $A + S$, a majority of the total optical loss $1 - R$ was caused by relatively high transmittance T, allowing for high throughput in a two-mirror optical cavity configuration. This mirror performance was instrumental in the detection of the highly reactive OD + CO → DOCO kinetics in Ref. [27] via direct frequency comb spectroscopy.

However, this study also showed the limitations of the technology at that time. As the quarter-wave design requires increasingly thick structures at longer wavelengths, gradually amounting growth defects and unintentional doping (i.e., pollution of the superlattice with other atoms) in molecular-beam epitaxy (MBE) limited the production process to wavelengths <4 µm. Furthermore, the authors pointed out the pertinent technological challenges for all-crystalline substrate-transferred coatings. Among those is the required ultrapure, low-defect-density crystal growth, which becomes more challenging with increasing thickness, i.e. for quarter-wave stacks with longer design wavelengths. This is exacerbated by the fact that GaAs and $Al_xGa_{1-x}As$, while being ideal materials for crystalline growth due to their matching lattice constants, have a relatively similar refractive indices [47]. This low refractive index contrast requires a higher number of layers to reach a target reflectivity R, driving total thickness and reducing the mirror bandwidth [1, 46].

1.2 Optical characterization and metrology in the mid-infrared

Based on the above results and challenges, we realized the study presented in Chapter 2. The primary objective was the development and characterization of mid-infrared interference coatings with minimized optical losses, as well as the extension of the crystalline coating technology to wavelengths above 4 µm. This work aimed to enable unique research in the mid-infrared spectrum, included the applications in precision interferometry and trace gas detection mentioned above, leveraging the expected improvements in cavity finesse and transmission due to the expected higher reflectivity R and lower absorption A, respectively.

To conclusively achieve and demonstrate these superior optical properties, several experimental methods had to be developed, improved, or extended to the mid-infrared. On

the one hand, mirror fabrication techniques had to be improved to ensure the precision and consistency of the coatings. The research delved into subdividing the optical coating into so-called *half stacks*, allowing to limit MBE-growth thickness by forming the final mirror of two halves. On the other hand, rigorous characterization methodologies, including broadband cavity ring-down (CRD) reflectometry and photothermal common-path interferometry (PCI), had to be extended into the MIR region to precisely and accurately distinguish all loss components, specifically transmittance T and Absorption A. This allowed to assess the performance of the developed coatings (see Table 2.1). While the study achieved significant advancements, these findings underscored the need for further research to address the identified limitations and optimize the coatings for broader applications and even longer wavelengths.

The results highlighted challenges, particularly in material behavior and technological constraints at the mid-infrared range. Specifically, the optical response of GaAs and $Al_xGa_{1-x}As$ high reflectors, especially when tailored for the mid-infrared range, was not fully understood. This highlighted the need for a deeper investigation into the basic optical properties of these two materials in the transparent wavelength range above 2 µm. These efforts culminated in the results presented in Chapter 3, where we developed a novel approach that allows for the simultaneous measurement of two refractive indices in a multilayer structure. Additionally, existing fabrication and characterization techniques, while advanced, had limitations when applied to the unique challenges of the mid-infrared spectrum. This necessitated the refinement of growth and bonding techniques and methodologies to achieve the desired coating performance, even at extreme reflectivity, as is outlined in Chapter 4.

1.3 The chapters ahead

Ludwik Fleck observed that scientific research often follows an iterative approach, highlighting the constant evolution and necessary reinterpretation of scientific findings over time based on new data and insights, allowing the formation of scientific facts [48]. The following chapters of this thesis exemplify such an iterative process, illustrating how initial challenges frequently lead to further investigations and subsequent advancements.

As outlined in this introduction, the sequence of articles in this thesis provides a comprehensive overview of the structured progression of substrate-transferred crystalline optical coatings in the mid-infrared. Subsequent chapters will provide a detailed analysis of crystalline optical coatings in the mid-infrared, discussing the specific material system, fabrication techniques, and characterization methods employed.

In short, the main part of this thesis begins with an initial feasibility study and foundational development of characterization techniques in Chapter 2, demonstrating the first substrate-transferred crystalline mid-infrared mirrors with excess loss $A + S$ below 10 ppm and giving a detailed description of the characterization setups we developed for this purpose. It then transitions to the foundational simultaneous measurement of refractive indices of thin-film $GaAs/Al_xGa_{1-x}As$ presented in Chapter 3, using a novel method that was developed in-house and yields relative uncertainties of 10×10^{-4} for both refractive idices. The thesis culminates in the demonstration of substrate-transferred crystalline and *hybrid* amorphous-crystalline HR coatings in Chapter 4, setting a new state-of-the-art in this wavelength range and establishing a new optical coating paradigm via the recently-invented hybrid coatings [49]. The demonstrated respective total loss values $1 - R$ of 13.60 ppm and 7.70 ppm brings these mirrors on-par with comparable HR coatings in the NIR and VIS region. Finally, a conclusion and outlook in Chapter 5 will explore the implications of these

findings, both in terms of further advancements and their contribution to the broader scientific field.

References

[1] H. A. Macleod, *Thin-Film Optical Filters* (CRC Press, Boca Raton; London; New York, 2018).

[2] L. Eldada, "Optical communication components", Rev. Sci. Instrum. **75**, 575 (2023).

[3] G. Gagliardi and H.-P. Loock, eds., *Cavity-Enhanced Spectroscopy and Sensing*, Vol. 179, Springer Series in Optical Sciences (Springer, Berlin, Heidelberg, 2014).

[4] A. J. Fleisher, D. A. Long, Q. Liu, L. Gameson, and J. T. Hodges, "Optical Measurement of Radiocarbon below Unity Fraction Modern by Linear Absorption Spectroscopy", J. Phys. Chem. Lett. **8**, 4550 (2017).

[5] G. Giusfredi, S. Bartalini, S. Borri, P. Cancio, I. Galli, D. Mazzotti, and P. De Natale, "Saturated-absorption cavity ring-down spectroscopy", Phys. Rev. Lett. **104**, 1 (2010).

[6] The LIGO Scientific Collaboration, J. Aasi, B. P. Abbott, R. Abbott, T. Abbott, M. R. Abernathy, K. Ackley, C. Adams, T. Adams, P. Addesso, et al., "Advanced LIGO", Class. Quantum Grav. **32**, 074001 (2015).

[7] F. Acernese, M. Agathos, K. Agatsuma, D. Aisa, N. Allemandou, A. Allocca, J. Amarni, P. Astone, G. Balestri, G. Ballardin, et al., "Advanced Virgo: a second-generation interferometric gravitational wave detector", Classical Quantum Gravity **32**, 024001 (2015).

[8] KAGRA collaboration, T. Akutsu, M. Ando, K. Arai, Y. Arai, S. Araki, A. Araya, N. Aritomi, H. Asada, Y. Aso, et al., "KAGRA: 2.5 generation interferometric gravitational wave detector", Nat. Astron. **3**, 35 (2019).

[9] M. Punturo, M. Abernathy, F. Acernese, B. Allen, N. Andersson, K. Arun, F. Barone, B. Barr, M. Barsuglia, M. Beker, et al., "The Einstein telescope: a third-generation gravitational wave observatory", Classical Quantum Gravity **27**, 194002 (2010).

[10] G. D. Cole, S. W. Ballmer, G. Billingsley, S. B. Cataño-Lopez, M. Fejer, P. Fritschel, A. M. Gretarsson, G. M. Harry, D. Kedar, T. Legero, et al., "Substrate-transferred GaAs/AlGaAs crystalline coatings for gravitational-wave detectors", Appl. Phys. Lett. **122**, 110502 (2023).

[11] I. Akasaki, "Nobel lecture: Fascinated journeys into blue light", Rev. Modern Phys. **87**, 1119 (2015).

[12] H. Amano, "Nobel lecture: Growth of GaN on sapphire via low-temperature deposited buffer layer and realization of p-type GaN by Mg doping followed by low-energy electron beam irradiation", Rev. Modern Phys. **87**, 1133 (2015).

[13] S. Nakamura, "Nobel lecture: Background story of the invention of efficient blue InGaN light emitting diodes", Rev. Modern Phys. **87**, 1139 (2015).

[14] P. Pust, P. J. Schmidt, and W. Schnick, "A revolution in lighting", Nat. Mater. **14**, 454 (2015).

[15] F. Samson, "Ophthalmic lens coatings", Surf. Coat. Technol. **81**, 79 (1996).

[16] C. A. Paulson, J. J. Price, K. W. Koch, C.-G. Kim, J.-H. Oh, L. Lin, A. N. Subramanian, B. Zhang, J. Amin, A. Mayolet, et al., "Industrial-grade anti-reflection coatings with extreme scratch resistance", Opt. Lett. **44**, 5977 (2019).

[17] T. Steinich and V. Blahnik, "Optical design of camera optics for mobile phones", aot **1**, 51 (2012).

[18] A. Dodoc, "Toward the global optimum in zoom lens design", in Zoom Lenses IV, Vol. 8488, edited by E. I. Betensky and T. Yamanashi, Proceedings of SPIE (2012), p. 848802.

[19] J. Sasián, *Introduction to lens design*, 1st ed. (Cambridge University Press, Cambridge, 2019).

[20] H. K. Raut, V. A. Ganesh, A. S. Nair, and S. Ramakrishna, "Anti-reflective coatings: A critical, in-depth review", Energy Environ. Sci. **4**, 3779 (2011).

[21] "Verfahren zur Erhöhung der Lichtdurchlässigkeit optischer Teile durch Erniedrigung des Brechungsexponenten an den Grenzflächen dieser optischen Teile", German pat. 685767C (Fa. Carl Zeiss, 1939).

[22] D. A. Long, A. J. Fleisher, Q. Liu, and J. T. Hodges, "Ultra-sensitive cavity ring-down spectroscopy in the mid-infrared spectral region", Opt. Lett. **41**, 1612 (2016).

[23] J. Tian, G. Zhao, A. J. Fleisher, W. Ma, and S. Jia, "Optical feedback linear cavity enhanced absorption spectroscopy", Opt. Express **29**, 26831 (2021).

[24] I. Galli, S. Bartalini, S. Borri, P. Cancio, D. Mazzotti, P. De Natale, and G. Giusfredi, "Molecular Gas Sensing Below Parts Per Trillion: Radiocarbon-Dioxide Optical Detection", Phys. Rev. Lett. **107**, 270802 (2011).

[25] M. G. Delli Santi, S. Bartalini, P. Cancio, I. Galli, G. Giusfredi, C. Haraldsson, D. Mazzotti, A. Pesonen, and P. De Natale, "Biogenic Fraction Determination in Fuel Blends by Laser-Based $^{14}CO_2$ Detection", Adv. Photonics Res. **2**, 2000069 (2021).

[26] A. Foltynowicz, P. Masłowski, A. J. Fleisher, B. J. Bjork, and J. Ye, "Cavity-enhanced optical frequency comb spectroscopy in the mid-infrared application to trace detection of hydrogen peroxide", Appl. Phys. B **110**, 163 (2013).

[27] B. J. Bjork, T. Q. Bui, O. H. Heckl, P. B. Changala, B. Spaun, P. Heu, D. Follman, C. Deutsch, G. D. Cole, M. Aspelmeyer, et al., "Direct frequency comb measurement of OD + CO → DOCO kinetics", Science **354**, 444 (2016).

[28] The KAGRA Collaboration, Y. Aso, Y. Michimura, K. Somiya, M. Ando, O. Miyakawa, T. Sekiguchi, D. Tatsumi, and H. Yamamoto, "Interferometer design of the KAGRA gravitational wave detector", Phys. Rev. D **88**, 043007 (2013).

[29] J. Steinlechner, P. G. Murray, M. Granata, and R. Bassiri, "Coatings for Gravitational Wave Detectors", in Optical Interference Coatings Conference (OIC) 2022 (2022), WA.4.

[30] J. R. Sites, P. Gilstrap, and R. Rujkorakarn, "Ion Beam Sputter Deposition Of Optical Coatings", Opt. Eng **22**, 447 (1983).

[31] G. D. Cole, W. Zhang, M. J. Martin, J. Ye, and M. Aspelmeyer, "Tenfold reduction of Brownian noise in high-reflectivity optical coatings", Nat. Photonics **7**, 644 (2013).

[32] U. W. Pohl, *Epitaxy of Semiconductors: Physics and Fabrication of Heterostructures*, 2nd ed., Graduate Texts in Physics (Springer International Publishing, Cham, 2020).

[33] P. Cancio, S. Bartalini, S. Borri, I. Galli, G. Gagliardi, G. Giusfredi, P. Maddaloni, P. Malara, D. Mazzotti, and P. De Natale, "Frequency-comb-referenced mid-IR sources for next-generation environmental sensors", Appl. Phys. B **102**, 255 (2011).

[34] G. B. Rieker, F. R. Giorgetta, W. C. Swann, J. Kofler, A. M. Zolot, L. C. Sinclair, E. Baumann, C. Cromer, G. Petron, C. Sweeney, et al., "Frequency-comb-based remote sensing of greenhouse gases over kilometer air paths", Optica **1**, 290 (2014).

[35] G. H. Rieke, G. S. Wright, T. Böker, J. Bouwman, L. Colina, A. Glasse, K. D. Gordon, T. P. Greene, M. Güdel, Th. Henning, et al., "The mid-infrared instrument for the *James Webb Space Telescope* , I: introduction", Publ. Astron. Soc. Pac. **127**, 584 (2015).

[36] N. Picqué and T. W. Hänsch, "Frequency comb spectroscopy", Nat. Photonics **13**, 146 (2019).

[37] R. Terabayashi, K. Saito, V. Sonnenschein, Y. Okuyama, K. Iwamoto, K. Mano, Y. Kawashima, T. Furumiya, K. Tojo, S. Ninomiya, et al., "V-cavity stabilized quantum cascade laser-based cavity ringdown spectroscopy for rapid detection of radiocarbon below natural abundance", J. Appl. Phys. **132**, 083102 (2022).

[38] F. Adler, K. C. Cossel, M. J. Thorpe, I. Hartl, M. E. Fermann, and J. Ye, "Phase-stabilized, 1.5 W frequency comb at 2.8–4.8 μm", Opt. Lett. **43**, 1330 (2009).

[39] A. Foltynowicz, P. Masłowski, T. Ban, F. Adler, K. C. Cossel, T. C. Briles, and J. Ye, "Optical frequency comb spectroscopy", Faraday Discuss. **150**, 23 (2011).

[40] G. Rempe, R. Lalezari, R. J. Thompson, and H. J. Kimble, "Measurement of ultralow losses in an optical interferometer", Opt. Lett. **17**, 363 (1992).

[41] N. Jin, C. A. McLemore, D. Mason, J. P. Hendrie, Y. Luo, M. L. Kelleher, P. Kharel, F. Quinlan, S. A. Diddams, and P. T. Rakich, "Micro-fabricated mirrors with finesse exceeding one million", Optica **9**, 965 (2022).

[42] C. A. McLemore, N. Jin, M. L. Kelleher, J. P. Hendrie, D. Mason, Y. Luo, D. Lee, P. Rakich, S. A. Diddams, and F. Quinlan, *Thermal noise-limited laser stabilization to an 8 mL volume Fabry-Pérot reference cavity with microfabricated mirrors*, (2022) arXiv:2203 . 15915v1, preprint.

[43] J. Kischkat, S. Peters, B. Gruska, M. Semtsiv, M. Chashnikova, M. Klinkmüller, O. Fedosenko, S. Machulik, A. Aleksandrova, G. Monastyrskyi, et al., "Mid-infrared optical properties of thin films of aluminum oxide, titanium dioxide, silicon dioxide, aluminum nitride, and silicon nitride", Appl. Opt. **51**, 6789 (2012).

[44] T. J. Bright, J. I. Watjen, Z. M. Zhang, C. Muratore, A. A. Voevodin, D. I. Koukis, D. B. Tanner, and D. J. Arenas, "Infrared optical properties of amorphous and nanocrystalline Ta_2O_5 thin films", J. Appl. Phys. **114**, 083515 (2013).

[45] S. Adachi, *Properties of Semiconductor Alloys*, red. by P. Capper, S. Kasap, and A. Willoughby, Wiley Series in Materials for Electronic & Optoelectronic Applications (John Wiley & Sons, Ltd, Chichester, UK, 2009).

[46] G. D. Cole, W. Zhang, B. J. Bjork, D. Follman, P. Heu, C. Deutsch, L. Sonderhouse, J. Robinson, C. Franz, A. Alexandrovski, et al., "High-performance near- and mid-infrared crystalline coatings", Optica **3**, 647 (2016).

[47] W. Heiss, T. Schwarzl, J. Roither, G. Springholz, M. Aigle, H. Pascher, K. Biermann, and K. Reimann, "Epitaxial Bragg mirrors for the mid-infrared and their applications", Prog. Quantum Electron. **25**, 193 (2001).

[48] L. Fleck, *Entstehung und Entwicklung einer wissenschaftlichen Tatsache. Einführung in die Lehre vom Denkstil und Denkkollektiv*, 9th ed., Suhrkamp Taschenbuch Wissenschaft 312 (Suhrkamp, Frankfurt am Main, 2012).

[49] G. D. Cole, V. Wittwer, L. W. Perner, G. Winkler, A. S. Mayer, O. H. Heckl, and D. Follman, "Substrate-transferred stacked optical coatings", U.S. pat. 20220187515A1 (Thorlabs, Inc., 2022).

2 Mid-infrared interference coatings with excess optical loss below 10 ppm

G. Winkler[1,a], **L. W. Perner**[1,a], G.-W. Truong[2,3], G. Zhao[4], D. Bachmann[2], A. S. Mayer[1], J. Fellinger[1], D. Follman[2,3], P. Heu[2], C. Deutsch[2], D. M. Bailey[4], H. Peelaers[5], S. Puchegger[6], A. J. Fleisher[4], G. D. Cole[2,3], O. H. Heckl[1]

[1]Christian Doppler Laboratory for Mid-IR Spectroscopy and Semiconductor Optics, Faculty Center for Nano Structure Research, Faculty of Physics, University of Vienna, Boltzmanngasse 5, 1090 Vienna, Austria

[2]Crystalline Mirror Solutions, Santa Barbara, CA and Vienna, Austria

[3]Thorlabs Crystalline Solutions, 114 E Haley St., Suite G, Santa Barbara, California 93101, USA

[4]Material Measurement Laboratory, National Institute of Standards and Technology, 100 Bureau Drive, Gaithersburg, Maryland 20899, USA

[5]Department of Physics & Astronomy, University of Kansas, 1251 Wescoe Hall Dr., Lawrence, Kansas 66045, USA

[6]Faculty Center for Nano Structure Research, Faculty of Physics, University of Vienna, Boltzmanngasse 5, 1090 Vienna, Austria

[a]These authors contributed equally to this work.

Wie lange kann das jetzt noch dauern? – Ein oder zwei Wochen vielleicht!

(Oliver H. Heckl, 2019)

Bibliographic information

The contents of this chapter were originally published in *Optica* as

> G. Winkler et al., "Mid-infrared interference coatings with excess optical loss below 10 ppm", Optica **8**, 686 (2021), DOI: 10.1364/OPTICA.405938.

including a supplementary document (see Section 2.5) and the following publication notes:

> Received 9 September 2020; revised 18 March 2021; accepted 22 March 2021 (Doc. ID 405938); published 14 May 2021

The contents of the article remain unchanged in this reprint. The formatting has been carefully adapted to the overall style of the doctoral thesis. The original title and authors correspond to the chapter title and authors. Author affiliations are given as they appear in the original publication.

Author contributions

For the here-presented results, I co-developed and built various iterations of the cavity ring-down reflectometer in Vienna and lead the development of the direct transmission measurement apparatus. Together with Georg Winkler, I took lead in the effort to generate the data presented in Fig. 2.6, except for the total loss measurements conducted at NIST. Furthermore, I supported the development and operation of the photothermal common-path interferometer, especially when the setup was adapted for polarization-dependent measurements. Georg Winkler, Gar-Wing Truong, and I co-developed the method to generate accurate transmittance data based on measurements of layer thicknesses via scanning-electron microscopy and an transmittance spectra via Fourier-transform infrared spectroscopy, as well as refractive index data from literature. I then spearheaded the necessary data analysis via transfer-matrix modeling, using Monte Carlo-type error propagation to estimate the uncertainty of this approach. Georg Winkler and I organized the writing of the manuscript, contributing substantial parts and incorporating the various inputs of the other co-authors.

Abstract

Low excess optical loss, combined absorption and scatter loss, is a key performance metric for any high-reflectance coating technology and is currently one of the main limiting factors for the application of optical resonators in the mid-infrared spectral region. Here we present high-reflectivity substrate-transferred single-crystal GaAs/AlGaAs interference coatings at a center wavelength of 4.54 µm with record-low excess optical loss below 10 parts per million. These high-performance mirrors are realized via a novel microfabrication process that differs significantly from the production of amorphous multilayers generated via physical vapor deposition processes. This new process enables reduced scatter loss due to the low surface and interfacial roughness, while low background doping in epitaxial growth ensures strongly reduced absorption. We report on a suite of optical measurements, including cavity ring-down, transmittance spectroscopy, and direct absorption tests to reveal the optical losses for a set of prototype mirrors. In the course of these measurements, we observe a unique polarization-orientation-dependent loss mechanism which we attribute to elastic anisotropy of these strained epitaxial multilayers. A future increase in layer count and a corresponding reduction of transmittance will enable optical resonators with a finesse in excess of 100,000 in the mid-infrared spectral region, allowing for advances in high-resolution spectroscopy, narrow-linewidth laser stabilization, and ultrasensitive measurements of various light–matter interactions.

2.1 Introduction

High-performance mirrors are employed for the construction of optical resonators in a variety of applications in optics and photonics. Stable resonators are routinely used to narrow the linewidth of continuous-wave lasers, thereby creating optical references for frequency comb stabilization and precision molecular spectroscopy [1–3]. Stable interferometers can be very small or very large in size, enabling scientific discovery in fields as seemingly unrelated as microcavity sensing [4] and gravitational wave detection [5]. Emerging applications in chemical sensing [6], discrete imaging [7], ultracold chemistry [8, 9], and even fundamental physics [10] would benefit immediately from high-performance mirrors at mid-infrared (mid-IR) wavelengths (loosely defined here as the spectral range from 3 µm to 8 µm) to probe new and interesting phenomena with increased precision. A long-standing goal is the development of low-loss mirrors such as those readily available throughout the near-infrared (near-IR) spectral region.

Traditional physical vapor deposition (PVD) techniques for the fabrication of high-reflectivity (HR) "supermirrors" such as ion-assisted evaporation or ion-beam sputtering are not widely available in the mid-IR or have not been optimized for the use of materials transparent in this spectral range. The predominant process used for such optics is traditional electron beam or thermal evaporation. Thus, the excess optical loss, that is the combined optical power absorption and scattering losses ($L = A + S$), of mid-IR mirrors is generally >100 parts per million (ppm) [11], with only rare exceptions: e.g., Zhao *et al.* reported on a mirror pair with a per-mirror power transmission coefficient $T = 69.9$ ppm and excess optical loss $L = 68.3$ ppm, resulting in a calculated finesse $\mathcal{F} = 22\,730 \pm 160$ near 4.5 µm [12]. High-quality near-IR mirrors on the other hand are routinely capable of excess optical loss at the <10 ppm level [13].

Excess optical loss strongly influences the on-resonance transmission T_{cav} of a cavity [14], and thereby the signal-to-noise ratio (SNR) in cavity-enhanced spectroscopy efforts, according to

$$T_{\mathrm{cav}} = \frac{T^2}{(T+L)^2}. \tag{2.1}$$

Here we assume equal power transmission coefficients T for both mirrors of a linear cavity and perfect mode matching. Simultaneously, one typically tries to maximize the cavity finesse,

$$\mathcal{F} = \frac{\pi}{T+L}, \tag{2.2}$$

which is inversely proportional to the cavity total loss $T + L$. Total loss can also be written as $1 - R$, with R denoting the power reflection coefficient of a mirror, as a direct consequence of conservation of energy $R + T + A + S = 1$. While T is a design parameter that is controllable via the layer count of an interference coating, L is fundamentally limited by the choice of materials and fabrication technology. If L is non-negligible in comparison to T, it is therefore necessary to strike a compromise in the maximization of both the above figures of merit. Sacrificing T for lower total losses then often results in cavities of both moderate $\mathcal{F}$ around 25,000–30,000 and T_{cav} well below 10%.

For cavity ring-down spectroscopy (CRDS) at a fixed coupled incident power and fixed cavity finesse, the shot-noise-limited standard error $\sigma(k)$ in the fitted CRDS rate k scales inversely with the mirror transmission T [15], i.e., inversely with the square root of the cavity transmission. For two-photon cavity ring-down spectroscopy (TP-CRDS) under the same conditions, the standard error on the two-photon rate scales inversely with T^2, i.e., inversely with the cavity transmission [16]. Particularly in the mid-IR (where scatter losses are negligible), absorption therefore remains the crucial performance parameter for any HR mirror technology.

Substrate-transferred monocrystalline interference coatings are a promising solution to these challenges in the mid-IR spectral region. With a room-temperature transparency window that extends from approximately 0.87 µm to beyond 10 µm, alternating multilayers of high refractive index gallium arsenide (GaAs) and low refractive index ternary aluminum gallium arsenide ($Al_xGa_{1-x}As$) alloys can, in principle, be used to create HR coatings over a broad wavelength window without fundamental adjustments in the manufacturing process. Crystalline coatings were originally developed as a means to overcome the Brownian-noise limit in precision interferometry [17], having simultaneously achieved ppm levels of optical losses and elastic loss angles in the 10^{-5} range [18]. Capabilities for high-power handling are yet another advantage of this technology, owing to the relatively high thermal conductivity of

the epitaxial multilayer when compared with more traditional amorphous structures. While enabling record-low levels of excess optical losses, minimal elastic losses, and high thermal conductivity, the GaAs/AlGaAs material system, however, exhibits a relatively low-index contrast. This results in the need for more layers to obtain coatings with a certain reflectance while still yielding a smaller bandwidth-to-wavelength ratio (both in terms of reflectivity and acceptable dispersion), when compared to PVD mirrors. Substrate-transferred crystalline coatings are currently limited to the well-established GaAs/AlGaAs material system because of high demands in uniformity and purity. It is important to note that this is not a fundamental limit, as epitaxial multilayers can, in principle, be manufactured from a diverse range of materials with potentially much larger index contrast [19, 20]. The outstanding challenge is to realize sufficiently high structural and optical quality in these less mature material combinations, while maintaining the requisite lattice matching conditions, such that the increased optical bandwidth of respective HR coatings does not come at the expense of increased excess optical losses.

Rather than relying on direct deposition onto the final optical substrate, our crystalline coatings are generated using an epitaxial layer transfer process. Initially, a monocrystalline heterostructure is grown on a lattice-matched GaAs base wafer via molecular beam epitaxy (MBE). Following the crystal growth process, a microfabrication procedure is employed in order to transfer the epitaxial multilayer to arbitrary optical substrates, including curved surfaces, via direct bonding. This technique yields monocrystalline interference coatings with high purity, low defect density, abrupt interfaces, and low surface roughness, which in turn enables HR coatings with state-of-the-art optical absorption of $A < 1\,\mathrm{ppm}$ from $1.0\,\mu\mathrm{m}$ to $1.6\,\mu\mathrm{m}$, with optical scatter of $S < 3\,\mathrm{ppm}$ in the same near-IR wavelength range [21]. This has led to rapid advancements in a diverse suite of state-of-the-art optical systems, ranging from millihertz-linewidth cavity-stabilized lasers for optical atomic clocks to prototype quantum-limited interferometers for noise abatement and squeezed light generation in gravitational wave detectors [22–24]. Similar advancements should be expected from crystalline coatings in the mid-IR spectral region.

In practice, however, extending the performance of monocrystalline coatings further into the infrared spectral region is not trivial. The first prototype mid-IR mirrors at design wavelengths of $3.3\,\mu\mathrm{m}$ and $3.7\,\mu\mathrm{m}$ exhibited promising excess optical loss levels of 159 ppm and 242 ppm, respectively [21]. These results were on par with other state-of-the-art mid-IR coatings, but still not comparable to their state-of-the-art near-IR counterparts capable of $A + S < 10\,\mathrm{ppm}$. Regardless, owing to the relatively low losses, these prototype mirrors helped enable the first detection and characterization of the transient intermediate radical trans-DOCO in the atmospheric-pressure reaction of the deuterated hydroxyl radical, OD, with carbon monoxide, CO [25]. Despite their vital role in studying real-time atmospheric chemical kinetics, however, the excess optical losses of these initial mid-IR mirrors were limited by excess scatter driven by structural defects in the very thick (20–30 μm) epitaxial multilayers.

Following significant improvements in the mid-IR crystalline coating production process as outlined in this work, we report on monocrystalline interference coatings with $A + S \leq 10\,\mathrm{ppm}$ at a wavelength of $4.54\,\mu\mathrm{m}$, thus demonstrating ultralow-loss mirrors with breakthrough performance in the mid-IR. These mirrors now realize the full performance potential predicted for the level of crystal purity feasible in a state-of-the-art MBE process (see Fig. 7 in [21]), at the longest wavelength demonstrated to date. In the course of this work, we independently characterize the wavelength- and polarization-dependent mirror metrics using a comprehensive suite of advanced, custom-built optical metrology tools. Several of those setups have been explicitly designed to work with a single broadband Fabry-Perot quantum cascade laser (FP-QCL) as an optical probe, being low-cost and available over a very wide range of mid-IR wavelengths, such that the characterization can be easily extended to future mirrors with different design wavelengths (a similar approach for ring-down measurements in the near-IR was presented in [26]). The presented methodical characterization of all optical loss channels has so far been lacking in the literature for similar mid-IR mirrors. The effort to develop new characterization techniques in this traditionally challenging spectral region should therefore help to overcome this major obstacle to realizing improvements in this field.

The demonstration of mid-IR mirrors with a reduction in $A + S$ by an order of magnitude, compared to

the current record in this wavelength range [12], will allow for improved sensitivity in a variety of linear and non-linear cavity-enhanced spectroscopy techniques. Specifically, the ultralow-loss mirrors reported here were designed for a target wavelength of 4500 nm to explore next-generation benchtop optical instruments for the detection of radiocarbon dioxide ($^{14}CO_2$) and rare clumped isotopic substitutions of nitrous oxide (N_2O). To date, optical detection of $^{14}CO_2$ by saturated absorption cavity ring-down spectroscopy has achieved sensitivity levels comparable with accelerator mass spectrometry facilities [27], and several competing linear absorption sensor architectures have also been demonstrated with known positive and negative trade-offs related to sensitivity [28, 29], accuracy [30], and portability [31, 32]. Recently, a scheme for Doppler-free TP-CRDS of $^{14}CO_2$ was demonstrated at 4.53 µm with a projected detection limit that was substantially better than currently available commercial gas analyzers [12] and its application to the sensitive and selective detection of $^{14}CO_2$ has also been proposed [16]. These immediate applications in trace gas and rare isotope detection using high-finesse optical resonators, as well as the previously mentioned potential applications in time-resolved spectroscopy, ultracold chemistry, and fundamental physics, make the advanced fabrication of ultralow-loss mid-IR mirrors of broad interest to the optics and photonics community.

2.2 Experimental details

As this was a first attempt at fabricating crystalline HR coatings with a center wavelength longer than 4.0 µm, as well as using an improved production process for minimizing excess optical losses, we undertook a comprehensive investigation of the mirror performance. In the course of our characterization efforts, we have determined the mirror reflectance R via cavity ring-down (CRD); the transmittance T by directly probing the transmission through the mirror (complemented by detailed calculations); and the polarization-dependent relative absorption ΔA employing photothermal common-path interferometry (PCI) [33]. This enabled us to extract each individual loss component, as the magnitude of A can be inferred via the aforementioned expression $R + T + A + S = 1$. For these mirrors, scatter S is assumed to be negligible based on the observation of $S + A < 3$ ppm of similar crystalline mirrors in the near-IR [21] and decreasing scatter loss with increasing wavelength. For example, a surface roughness below 0.2 nm, as is routinely achieved with these optimized coatings, results in a calculated scatter loss of ∼0.3 ppm at 4540 nm [34].

2.2.1 Mirror design and transmission model refinement

The reflectance and transmittance of multilayer thin-film structures can readily be calculated via transfer matrix methods (TMMs) [35, 36]. The quarter-wave layer structure of the crystalline mid-IR mirrors under study was designed for a stop band center wavelength of 4500 nm with a target transmittance of 140 ppm, comprising 34.5 periods of GaAs/$Al_{0.92}Ga_{0.08}As$ with individual layer thicknesses of 340.0 nm and 388.6 nm, respectively, based on refractive index values taken from Afromowitz [37]. Deposition of the crystalline interference coating was carried out in a multiwafer MBE system employing a 14×4 in. wafer configuration with on-axis (100)-oriented 100 mm diameter semi-insulating GaAs base wafers. For these mirrors, we employed a novel fabrication process to minimize the limiting optical scatter. This was realized by reducing the total thickness of the grown heterostructure by using stacked optical coatings [38]. In this process we bond two "half mirrors," halving the epitaxial multilayer thickness and significantly improving the material surface quality. In this process the potentially defective surface of the as-grown crystal is embedded in the middle of the multilayer and the face of the mirror that directly interacts with the optical field exhibits a substantially improved surface quality, as with our flipped optical coatings described in [21]. Following the MBE growth process, we ran a wafer-scale GaAs-to-GaAs bonding process, followed by substrate and etch stop removal on one of the wafer pairs, to generate the full coating stack. The 12 mm diameter coating discs were then lithographically patterned and selectively etched through the stacked epitaxial multilayer in preparation for the substrate transfer process. Finally, the coating discs were transferred via a second direct bonding process to 25.4 mm diameter silicon (Si) substrates with a concave 1 m radius of curvature and 6.35 mm thickness. The planar backside of each substrate was coated with a broadband (standard PVD) anti-reflection (AR) coating over the range of 3 µm to 5 µm ($R = 0.3\%$ at 4.5 µm). Both standalone

coating discs and completed mirrors on Si substrates were used for the characterization efforts described in the course of this paper.

To begin the analysis process, variations in the deposition rate during the MBE growth process necessitate correction of these nominal layer thicknesses to more accurately represent the as-grown samples. These corrections were determined using a combination of x-ray diffraction (XRD), Fourier transform spectrometry (FTS, Bruker VERTEX 80), and cross-sectional scanning electron microscopy (SEM, Zeiss Supra 55VP). In addition to providing guidance on the layer thicknesses, by probing the material lattice constant, XRD measurements also provide an estimate of the alloy composition of the low-index ternary AlGaAs alloy with relative error bounds of the order of 1%.

Cross-sectional SEM imaging of a cleaved interference coating stack prior to the substrate transfer process allowed us to determine the as-grown layer thicknesses (see Fig. 2.1) by means of digital post-processing using an edge-detection and peak-finding routine (ImageJ, IJ BAR package). It is expected that the derived layer thicknesses differ among mirrors of the same production batch by a global scaling factor, depending on the exact lateral position inside the MBE chamber, while the relative layer thicknesses are expected to be very similar over a wide area [39]. The relative error in SEM length measurement calibration was estimated to be 1%, determined by measuring a calibration sample (Raith CHESSY). Additionally, edge detection introduced an error of ±4 nm due to the limited resolution of the SEM images.

Broadband FTS measurements generated transmission spectra of the mirrors under test with spectral resolution of 0.5 nm and were recorded in a nitrogen atmosphere at ambient pressure. While the FTS does not allow for direct measurement of the mirror transmittance close to the mirror center wavelength due to its limited sensitivity and low SNR, the stop band width and characteristic structure of the sidelobes in these spectra enable a precise extrapolation to the center wavelength through a model fit. The TMM model was fitted to the FTS spectra using the SEM-determined layer thicknesses as starting values, with the aforementioned global scaling factor, and the Al concentration in the low-index layers (bounded by XRD error intervals) as free parameters.

To obtain an error estimate of the derived mirror transmittance at the center wavelength, the following

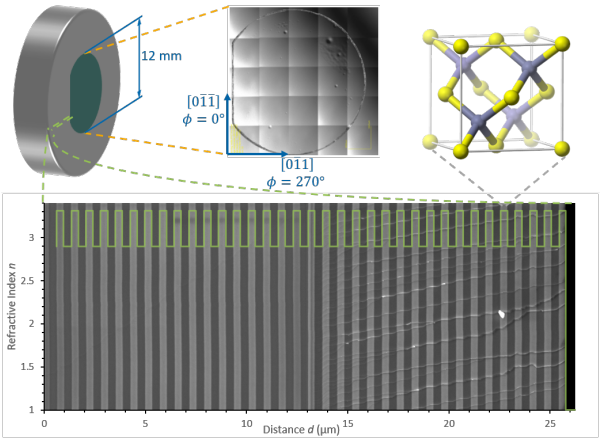

Fig. 2.1. Details of the prototype mirror structure. Top left: schematic of the 12 mm diameter crystalline coating bonded onto a Si substrate of 25.4 mm diameter with a concave 1 m radius of curvature. The flat is aligned with the [0$\bar{1}\bar{1}$] crystal axis. Top middle: stitched optical micrographs of the 12 mm diameter coating surface following the substrate transfer process. The values for ϕ refer to the relative polarization angle as defined later in 2.8. Top right: zincblende structure of the crystalline coating (Ga in yellow, As in gray). Bottom: cross-sectional SEM images of the layer stack consisting of 34.5 periods of alternating GaAs (light gray) and AlGaAs (dark gray) layers. The full coating was fabricated by stacking two intermediate structures grown with 17 periods capped with a 1/8th wave GaAs layer prior to substrate transfer. The bonding line is faintly visible in the middle of the centermost GaAs layer. Abrupt interfaces allow for precise measurements of individual layer thicknesses via edge detection (the green line indicates the refractive index profile). The terraced cracks in the cleaved coating (visible in the right half of the multilayer) result from a minute mismatch in crystal axis orientation from the stacking process, leading to an imperfect cleave of the top half of the mirror.

Monte Carlo-style procedure was employed: starting from the above initial fit values, we performed further forward model calculations to sample the space of reasonable transmission spectra. Candidate spectra were generated for random variations of the best-fit parameters (within their respective relative error bounds). From these candidates, we expunged all those where center wavelength and FWHM of the mirror stop band deviated by more than ±0.5 nm from the best initial fit, thereby excluding input parameter combinations that lead to an unphysical deviation from FTS measurements. The set of remaining spectra was then used to determine mean and standard error (at the ppm level) of the minimum transmittance. Note that in this procedure we have assumed abrupt interfaces and no variation in Al content over the full structure, as well as a perfect AR coating on the backside of the Si substrate. The refractive indices for the epitaxial materials were taken from [37], while for the Si substrate

the dispersion data was taken from [40]. A refractive index of $n = 1$ was assumed for the incident and exit media.

2.2.2 Cavity ring-down measurements

We constructed a linear resonator from two mirrors of the same production batch and implemented two variations of the well-established CRD technique [41] to infer the total loss $1-R$, independent of laser source amplitude fluctuations, by measuring the cavity decay time constant τ and cavity length d and using the equation $(1 - R) = d/(c\tau)$, where c is the speed of light.

At the Christian Doppler Laboratory for Mid-IR Spectroscopy and Semiconductor Optics (CDL) in Vienna, Austria, a low-cost broadband FP-QCL (TL QF4550CM1) was coupled into multiple longitudinal modes of the cavity by exploiting direct passive feedback in a simple linear configuration (Fig. 2.2). To the best of our knowledge, this is the first demonstration of such a passive feedback scheme for an FP-QCL. It features the advantages of a broad useable bandwidth (of at least 150 nm in the present case) in a low-complexity setup without high-bandwidth, active electronic control loops. The sample mirrors were mounted 30.6 ± 0.2 cm apart as end elements of a custom vacuum chamber, which was first purged with nitrogen, then evacuated to typical pressures of 0.5 kPa to 1.0 kPa using an oil-free roughing pump. Ring-down time-traces were recorded using an amplified InAsSb detector (TL PDA10PT-EC). A custom microcontroller-based threshold detection circuit was used to detect on-resonance cavity transmission, shutter the laser, and trigger data capture [42]. Spectral coverage extends from about 4520 nm to 4720 nm (2119 cm^{-1} to 2212 cm^{-1}), with a monochromator (Spectral Products Digikröm CM 110, grating 300 G/mm, blaze wavelength 2.5 µm) enabling measurements at 5 nm spectral resolution. The peak of the overall FP-QCL emission bandwidth was steered via additional external grating feedback (first order reflected backwards) and monitored by a custom low-resolution FTS instrument. With the FP-QCL and sample mirrors forming a coupled cavity system, a delay stage between the source and backside of the first mirror was tuned to find resonance conditions causing power buildup in the cavity formed by the sample mirrors to occur within the spectral transmission window of the monochromator. During measurements, the transmitted TEM_{00} transverse cavity modes were monitored on a mid-IR microbolometer camera (Visimid Phoenix) to restrict sampling to the smallest possible area on the mirrors and to avoid transversal mode beating. Given the cavity length resulting in a free spectral range of $\nu_{\mathrm{FSR}} = 490 \pm 5$ MHz, beat notes between multiple longitudinal modes could not be resolved in the measurements.

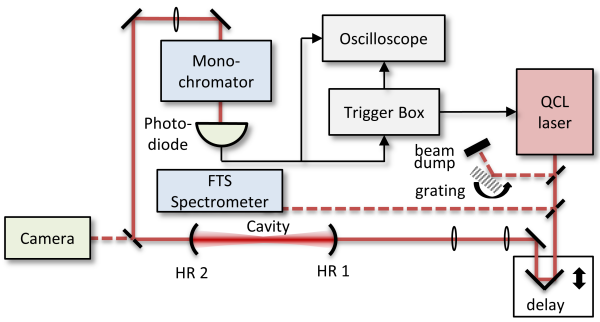

Fig. 2.2. Schematic of the FP-QCL-based ring-down setup at CDL. In this setup a FP-QCL without internal stabilization is utilized for excitation, with a custom trigger circuit initiating the ring-down process. This architecture allows for significant flexibility in mirror characterization via changes in the laser source. This system is similar to that described in [26] with additional wavelength monitoring, while operating in the mid-IR and without raster-scanning capabilities. To control the center of the emission spectrum, additional feedback to the FP-QCL is provided via a reflection grating in Littrow configuration.

To avoid birefringence-induced polarization mode beating, the linear polarization of the FP-QCL was aligned parallel to the net slow or fast axis of the ring-down cavity and exponential fits to decay curves checked for clean modulation-free residuals. Since the monochromator grating acted as a fixed polarization analyzer, it was not possible to study polarization-dependent effects at arbitrary input polarization angles.

We analyzed the theoretical possibility of a systematic bias of the measured ring-down times through correlations between the intracavity power spectrum and etalon resonances. We experimentally verified that influences of a potential etalon between the FP-QCL end facet and ring-down cavity are in fact averaged out through the broadband excitation, by introducing varying levels of additional losses (up to 50%) in between these two elements, without observing systematic effects.

An independent experiment at the National Institute of Standards and Technology (NIST) in Gaithersburg, Maryland, USA was performed to cross-check the FP-QCL-based broadband measurements at CDL

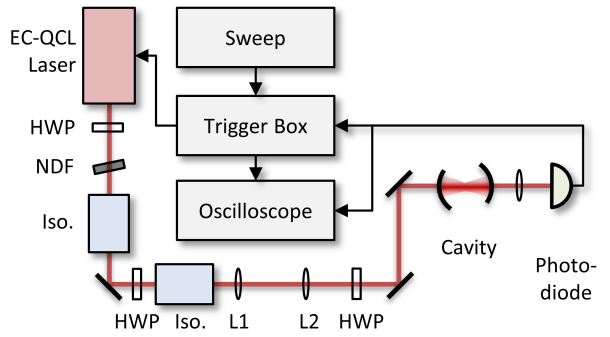

Fig. 2.3. Schematic of the ring-down setup at NIST. EC-QCL, external-cavity quantum cascade laser; HWP, half-wave plate; NDF, neutral density filter; Iso., optical isolator.

and to evaluate potential systematic errors in the experimental determination of the quantity $1-R$. There, a continuous-wave external-cavity QCL (EC-QCL) with linewidth $<$10 MHz, capable of exciting individual longitudinal modes of a linear cavity, was used to measure $1-R$ as a function of wavelength from 4480 nm to 4600 nm (2174 cm^{-1} to 2232 cm^{-1}) with high resolution, as illustrated in Fig. 2.3. At NIST, the EC-QCL was passively coupled to a single mode of the cavity by dithering the laser current, an operation which also acted as an optical shutter to initiate decay events. Finally, using either a quarter-wave or halfwave plate and a linear polarization analyzer, the EC-QCL system also probed for polarization-dependent losses in the single-crystal optical coatings.

To construct the cavity at NIST, each mirror was secured at the center of a vacuum viewport using a 25.4 mm diameter retaining ring and isolated from the laboratory environment using wedged CaF_2 vacuum windows. The mirrors were tested under vacuum while experiencing zero pressure difference between their AR- and HR-coated faces. Nominal mirror separation defining the optical cavity length was estimated from machine drawings to be $d = 15.6 \pm 0.6$ cm and confirmed by caliper measurements of the individual components prior to assembly. The cavity free spectral range was therefore $\nu_{\mathrm{FSR}} = 960 \pm 40$ MHz.

Frequency-dependent total losses were measured by coarse temperature tuning of the continuous-wave output of the EC-QCL. At each unique frequency ν, cavity transmission during laser current dithering was monitored by a liquid-nitrogen-cooled InSb photodetector. Once transmission reached a user-defined threshold, the laser current was further shifted by summing a square-wave signal with the dither signal to rapidly extinguish the pumping laser field, thus yielding a single decay event which was amplified and fitted for the exponential decay time constant τ.

Optical components shown in Fig. 2.3 were placed at etalon immune distances [43] (whenever possible) and tilted relative to the incident laser beam to effectively eliminate the coupling of scattered light with the optical cavity mode. To avoid the coupling of spurious reflections from the AR-coated face of the mirrors into the optical cavity mode, the two-mirror cavity was aligned to create an effectively wedged surface at the flat AR-coated face relative to the HR-coated concave mirror surface. Detailed methods of cavity alignment are reported in Supplement 1.

2.2.3 Direct transmission measurements

To experimentally decompose the individual mirror total loss components summarized in $1-R$, we used a ratiometric, lock-in amplified method to directly probe mirror transmittance (DIRT). The underlying principle of this measurement is to compare the incident and transmitted intensities for a single mirror using the same FP-QCL source as in the CDL ring-down measurements. The key elements of this setup are the high sample irradiance offered by the laser source, lock-in detection to increase the SNR and dynamic range of the detector, as well as ratiometric detection to account for power fluctuations of the laser during acquisition. Given the high output power, spectrally resolved measurements could be achieved by using the grating monochromator.

The experimental apparatus is based on a FP-QCL in quasicontinuous wave (QCW) mode (refer to Fig. 2.4 for abbreviations), controlled by the diode controller's (TL ITC4002QCL) internal QCW modulation. The QCW square-wave signal was used as a reference for the digital multichannel lock-in amplifier (LIA, Zurich Instruments HF2LI). The monochromator was used to narrow the measurement range to a passband of $<$2.5 nm for each measurement. This output was then divided into two separate beam paths by a plate beam splitter (BS) to allow monitoring of intensity fluctuations at the measurement wavelength. A half-wave plate and a polarizer (ISP Optics POL-1.5-5-SI) in front of the BS were used to set p polarization with respect to the BS, thereby avoiding any changes in its splitting ratio. In the sample path, leading to D1, we used a $2\times$ beam reducer to obtain a smaller beam diameter when probing the HR sample.

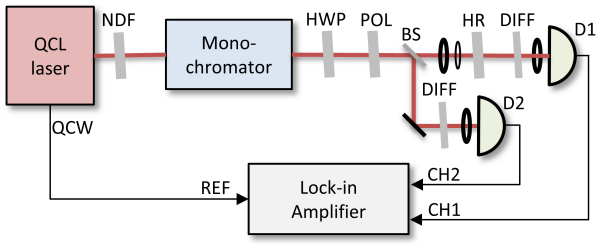

Fig. 2.4. Block diagram of the direct transmission setup. QCW, quasi-continuous wave modulation signal; NDF, reflective neutral density filter; HWP, half-wave plate; POL, polarizer; BS, 50/50-coated beam splitter; HR, sample under test; DIFF, ground glass diffusor; D1/D2, detectors.

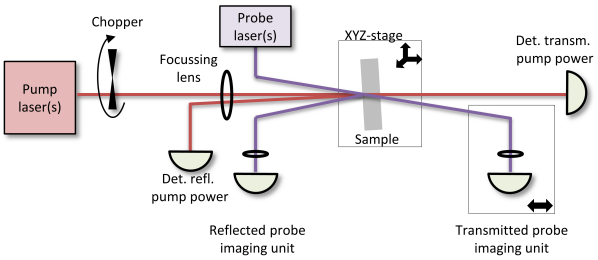

Fig. 2.5. Block diagram of the photothermal interferometer for absorption measurements (PCI). A slight angle between pump and probe beams allows dumping of the pump and pickup of either the transmitted or reflected probe beam.

The two identical detectors (TL PDA20H) were connected to separate channels of the LIA and simultaneously recorded during the measurement. By dividing the respective demodulated amplitudes CH1/CH2 we suppressed any common fluctuations of the input, obtaining a time trace with drastically reduced variations. Following this approach at each measurement wavelength, a pair of measurements with and without the HR sample was taken. By dividing the mean value of each, we obtained the intensity transmission coefficient in the monochromator bandpass.

Care was taken to avoid any perturbation of the monitor path or the FP-QCL by placing the HR sample at a slight angle to avoid systematic errors in T due to backreflections. Two ground glass diffusers were placed in front of the detectors to suppress the influence of spatial variation of responsivity across the active area of the detector [44]. To ensure linear detector response over the measurement range of 5 orders of magnitude at the targeted uncertainty levels, the QCL output was attenuated via neutral density filters while the LIA served to sufficiently increase detector sensitivity and dynamic range.

Accuracy in these measurements was largely limited by beam steering effects related to the insertion of the mirror sample and estimated to be ± 12 ppm. Comparative relative measurements (e.g., as a function of input polarization) could, however, benefit from the significantly better precision of ± 2 ppm.

2.2.4 Direct absorption measurements

For independent absorption measurements, the FP-QCL was again used as a pump laser (capable of 450 mW output power) in a PCI system (Stanford Photo-Thermal Solutions) modified for mid-IR operation. In this setup (Fig. 2.5), absorption in the thin-film coating at the pump wavelength was measured indirectly by probing the thermal lens induced in the non-absorbing substrate via a second probe laser [45]. Both pump and probe lasers were focused onto the same spot of the sample coating (with waist diameters of about 70 µm and 200 µm, respectively). The localized "hot spot" induced by the more tightly focused pump imprints a phase distortion on the central part of the more loosely focused probe beam, causing interference with the undisturbed outer probe wavefront (which acts as the reference arm of the common-path interferometer). The resulting interference pattern appears in the near field of the interaction region, the central maximum of which is then imaged onto a detector. Using lock-in detection referenced to the chopped pump laser, the relative intensity modulation depth $\Delta I/I$ of the probe signal was recorded. Normalized by the incident pump power P, the signal is proportional to absorption α over several orders of magnitude, with proportionality constant R_c denoting the system responsivity: $\Delta I/(IP) = \alpha R_c$. PCI absorption measurements are a common characterization technique in the near-IR. Extending this technique to the mid-IR, however, involved overcoming numerous challenges related in part to the substrate response, probe wavelength, detection path of the probe (i.e., in transmission or reflection), and calibration technique.

In the near-IR, R_c is determined by measuring a calibration sample of known absorption. This calibration step requires that the substrate material as well as the absorbing surface layer thickness match the sample under study to assure a comparable thermal response. Typically, a metallic coating with broadband absorption of a few tens of percent serves as such a reference sample. However, as a consequence of mid-IR HR coatings being rather thick (owing to the long wavelength and corresponding increase in the individual quarter-wave layer thicknesses), the thermal lens in

the coating layer itself becomes non-negligible, making it challenging to fabricate a calibration sample with comparable thermal response. It is for this reason that we resorted to a novel *in situ* calibration technique employing a more strongly absorbed "proxy pump" laser [45] with a wavelength of 532 nm (above the GaAs bandgap) in combination with the sample itself, to provide the reference absorption measurement. In either case, the high reference absorption can be independently determined via direct measurements of incident, transmitted, and reflected power, with the relative error of the calibration measurement transferring to the measurement of the actual sample of much lower (typically ppm-level) absorption. Care was taken to focus the proxy pump to the same diameter as the primary pump, to ensure the same geometry of the thermal lens. This was confirmed by assuring that the same value of R_c is deduced for both pumps when using a custom-made calibration sample of similar known high absorbance for both pump wavelengths (broadband 7 nm Cr overcoat on a CaF2 substrate).

Using fused silica (FS) as a substrate material typically offers a high system responsivity R_c and therefore high sensitivity, owing to its low thermal conductivity and the strong temperature dependence of the refractive index. Although a dedicated sample with the 4.54 µm crystalline coating bonded to FS was available, it was found that the heating contribution from substantial absorption of the transmitted mid-IR pump light within the FS substrate itself was not sufficiently distinguishable from pump absorption within the actual coating. For this reason, we resorted to the use of Si substrates (transparent at the pump wavelength) in all further measurements, at the expense of lower SNR (given the high thermal conductivity of the substrate). Keeping in mind that PCI is an interferometric method, the use of short wavelength probe light is favored for high system responsivity. Measurements were therefore conducted with a HeNe probe at 633 nm in reflection (exhibiting higher sensitivity than alternative attempts using telecom-wavelength IR probes detected in reflection or transmission). However, with a probe photon energy (1.96 eV) exceeding the GaAs bandgap energy of 1.42 eV, the measured pump absorption is distorted by additional probe-induced absorption via free carriers. We therefore took several measurements at decreasing probe power and extrapolated to zero probe power to determine the absorption [21].

The crystalline mirror coatings were repeatedly purged with dry nitrogen between measurements to mitigate influences of surface contamination. To perform measurements at the required ppm-level precision, it was necessary to ensure a heat-up time of the QCL pump laser of around 15 minutes to maintain a constant power level and beam profile.

2.3 Results

2.3.1 Total loss and transmittance

Our measurement results, summarized in Fig. 2.6 and Table 2.1, show excellent performance for these prototype mirrors at 4.54 µm. The refined transmission model derived from XRD, cross-sectional SEM, and FTS is shown as the solid red curve in Fig. 2.6 (top). The above-described routine allows for an estimate of the center wavelength $\lambda_{0,T} = 4538 \pm 1$ nm and an expected mirror transmittance $T(\lambda_{0,T}) = 144 \pm 2$ ppm at the stop band center, with the error bands obtained by the same procedure. The shift of the measured center wavelength from the design target of 4500 nm is due to unavoidable deviation in layer thicknesses by a small global scaling factor during MBE growth ($<1\%$ for the studied samples). It can be readily seen from Fig. 2.6 (top) that our model, based on the as-grown layer geometry derived from SEM imaging (capturing thickness variations of different high- and low-index layers with a relative standard deviation of 2%), captures modulations in the sidelobes observed in FTS much better than a model assuming a strictly periodic layer structure (dashed red design curve). Although we assumed an error of 1% for XRD measurements of the Al alloy composition, our evaluation suggests a much lower uncertainty of 0.2%, with best-fit values for the Al composition ranging only from 0.9229 to 0.9247. Comparing these results with our direct transmission measurements [brown triangles in Fig. 2.6 (mid) and Fig. 2.6 (bottom)], we observe excellent agreement within the error bounds (reflecting the full uncertainty budget).

Total loss values (measured with the incident linear polarization state set to $\phi = 90°$) extracted from the CRD measurements at CDL (dark blue curve, minimum of 153 ± 1 ppm at $\lambda_{0,\mathrm{CDL}} = 4534 \pm 1$ nm) and NIST (light blue data points, minimum of 149 ± 6 ppm at $\lambda_{0,\mathrm{NIST}} = 4533 \pm 1$ nm) are also included. For

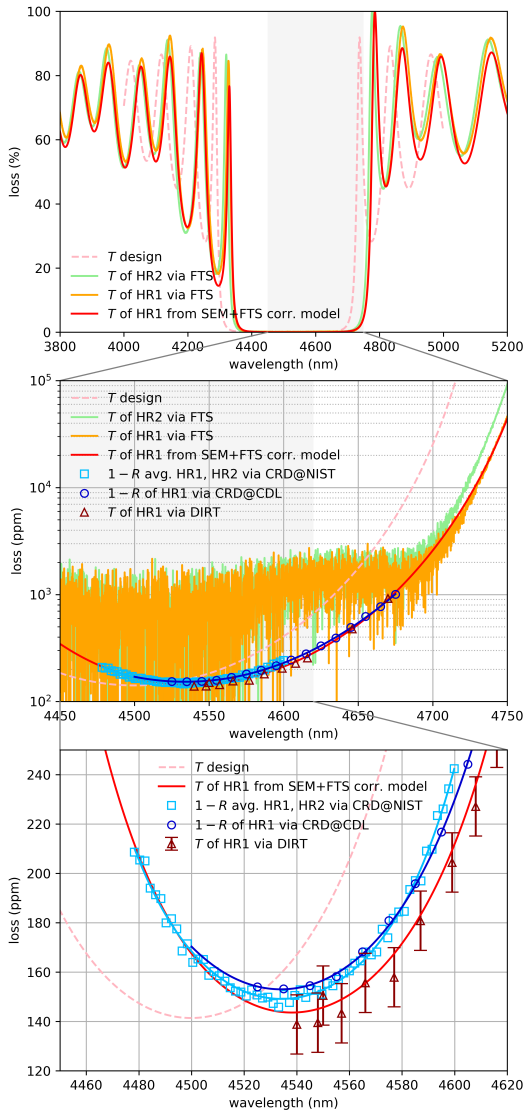

Fig. 2.6. Summary of spectrally resolved results for total loss $1-R$ and transmittance T. All measurements were performed for incident linear polarization angle $\phi = 90°$ relative to the $[0\bar{1}\bar{1}]$ crystal axis. Top panel: the two sample mirrors are distinguished according to their broadband transmission spectra (labeled HR1 and HR2) and differ by a slight shift of center frequency (likely due to inhomogeneities during layer growth). The solid red line represents a model for the as-grown layer structure of HR1, based on a fit to the FTS results, and layer thicknesses derived from SEM images, accurately reproducing the asymmetric structure of side-maxima outside the stop band. The thin dashed line shows the model calculation for uniform target layer thicknesses for comparison. Middle panel: zoom in to the stop band center showing the low SNR of the FTS results. The derived model (red line) shows good agreement with all other high-precision loss measurements. Bottom panel: a detailed look at the total loss and transmittance. The total loss (plotted in shades of blue) was independently measured by two separate teams using different realizations of a cavity ring-down (CRD) scheme and combinations of mirrors with nominally identical minimum transmittance from the same production batch. Datasets are fitted with fourth-order polynomials to guide the eye (solid lines). The transmittance was determined from the model calculation (red line) and verified by direct transmission measurements (DIRT, brown triangles).

Table 2.1. Comparison of Design and Experimental Values for Cavity End-Mirrors with Mid-Infrared Crystalline Coatings[a,b,c]

Parameter	Design	Measured	Uncertainty	Units
λ_0	4500	4535	1	<nm
$1-R$	<162	151	3	ppm
T	142	144	2	ppm
S	<1	—	—	ppm
A	<20	7	4	ppm

[a] For total loss $1-R$ and central wavelength λ_0, the mean value of different measurements of Fig. 2.6 is presented.
[b] As mentioned in the introduction, optical scatter is negligible in this case and thus its absolute value and uncertainty is ignored.
[c] Design values for absorption A are taken from Fig. 7 in [21]. Actual sample absorption is inferred from all other losses.

both, the relative standard uncertainty in the total optical losses, $u_r = \sigma_{1-R}/(1-R)_{\min}$, was estimated from a quadrature sum of reproducibility and a conservative estimate of dominating systematic uncertainty (mainly dictated by the cavity length uncertainty). The standard uncertainty at the center wavelength of ± 1 nm was taken to equal the accuracy of monochromator calibration (CDL) and accuracy specified by the laser manufacturer (NIST).

From the average value of $(1-R)_{\min}$, presented in Table 2.1, we infer a cavity finesse of $\mathcal{F} = 20\,805 \pm 413$. This is a $5\times$ improvement over the first mid-IR monocrystalline mirror coatings with $\lambda_0 = 3.7\,\mu$m [21], and the maximum cavity transmission is now improved to $T_{\text{cav}} > 92\%$ from a value of 24% that would result from the assumption of $L = 160$ ppm, based on that previous work. Thus, we achieve a cavity finesse on par with the best currently available PVD-coated alternatives, while using an intentionally conservative multilayer design for these prototype mirrors. In this same comparison, the cavity transmission is enhanced by a factor of 4, owing to the extremely low level of excess optical losses of the revised crystalline coatings. This foundational work paves a path to achieving cavity finesse values beyond 100,000 in subsequent efforts by further increasing the number of deposited layers, while simultaneously maintaining tens of percent of cavity transmission.

2.3.2 Mirror birefringence

The NIST setup was used to measure mirror birefringence by performing frequency-swept CRD at an incident linear polarization of $\phi = 45°$, exciting both orthogonal birefringence modes during the frequency sweep [46]. To observe beating from the orthogonal

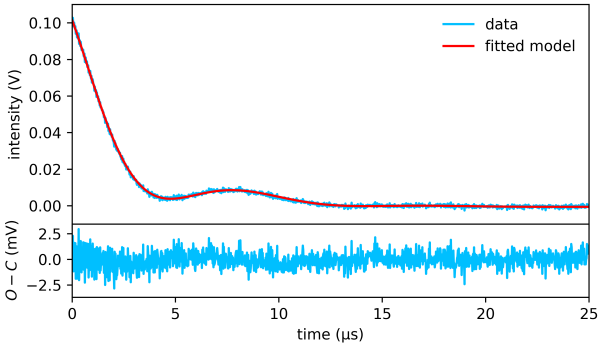

Fig. 2.7. Typical cavity ring-down (CRD) trace with visible polarization mode beating, recorded at NIST for an input polarization angle of $\phi = 45°$. An associated birefringence splitting of $\Delta\nu_{\text{beat}} = 110 \pm 5\,\text{kHz}$ is extracted from the fitted model (corresponding residuals shown at the bottom).

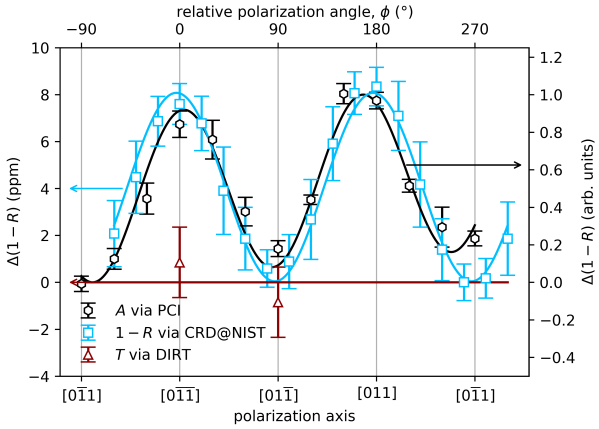

Fig. 2.8. Change in optical losses plotted versus linear polarization angle ϕ relative to the $[0\bar{1}\bar{1}]$ crystallographic plane. About 8 ppm peak-to-peak variation is measured in total loss $(1 - R)$ cavity ring-down (CRD) measurements between orthogonal input polarization states, reproducing the qualitative behavior observed for absorption A via photothermal common-path interferometry (PCI). Direct transmission measurements (DIRT) suggested no polarization dependence in coating transmittance.

birefringence modes, a linear polarization analyzer was placed after the cavity and before the photodetector at a matching relative angle of $\phi = 45°$. The resulting decays deviated strongly from exponential behavior, as evidenced by the representative cavity decay plotted in Fig. 2.7. Birefringence mode beating is clearly a large perturbation on the single-mode decay, and its frequency is resolved by our detection system with >10 MHz of bandwidth. Using the most general mode beating equations discussed in [46], we fitted the cavity decay event at $\phi = 45°$ to yield a birefringence splitting of $\Delta\nu_{\text{beat}} = 110 \pm 5\,\text{kHz}$, a value larger than the inferred cavity mode linewidth of $\delta\nu_{\text{cav}} = 45.6 \pm 1.8\,\text{kHz}$. The observed birefringence is presumably induced by anisotropic strain in the crystalline multilayer as discussed below.

2.3.3 Observation of polarization-dependent absorption loss

While sources of systematic error in the current mid-IR PCI setup prohibit absolute absorption measurements at the desired few-ppm level of sensitivity, we were still able to observe a very distinct and unexpected relative change of absorption loss as a function of incident pump laser polarization. As shown in Fig. 2.8, absorption reaches a minimum for linear pump polarization oriented at a relative angle of $\phi = 90°$ with respect to the $[0\bar{1}\bar{1}]$ crystal axis (represented by the coating flat) and a maximum for $\phi = 0$. It was verified that such an effect is only observed for crystalline coatings (by comparison to standard PVD-coated mid-IR HR mirrors). We excluded that the effect is an artifact of the measurement geometry by verifying that rotation of the sample produced the same effect as rotating the pump polarization. It was also observed that the effect has no appreciable dependence on small changes to the pump angle of incidence.

As evidenced by the blue data points in Fig. 2.8, the same polarization dependence could subsequently be observed for total loss, measured via CRD at NIST, with relative peak-to-peak variation quantified to be 8.3 ppm. No dedicated polarization analyzer was used between the cavity and the detector to avoid the previously discussed effect of birefringence mode beating. A complete second wavelength-dependent set of $1 - R$ values was also calculated from CRD measurements with the incident linear polarization state $\phi = 0°$. Compared to the orthogonal configuration plotted in Fig. 2.6, the $\phi = 0°$ dataset yielded a slightly higher value of $(1 - R)_{\text{min}} = 158 \pm 6\,\text{ppm}$ at a nearly identical center wavelength of $\lambda_0 = 4532\,\text{nm}$, in good agreement with the polarization-dependent changes in total losses observed in Fig. 2.8. A similar trend also seemed observable in high-finesse 1550 nm crystalline coatings; however, given the low absorption in those coatings (at the ≤1 ppm level), the contribution of absorption to the effect is difficult to accurately quantify in this case (T. Legero, PTB, Germany, personal communication, February 2019).

No such polarization dependence was observed in direct transmission measurements (brown triangles in Fig. 2.8). Since scatter is expected to be bounded to the single ppm level (as determined for comparable near-IR crystalline mirrors), and direct ab-

sorption measurements are insensitive to scatter, all observations suggest that the observed polarization-dependent loss can be solely attributed to absorption.

2.3.4 Theoretical modeling of polarization-dependent absorption and refractive index

From our current understanding of these novel low-loss monocrystalline mirrors, free-carrier absorption is the limiting mechanism for absorption loss for below-bandgap illumination. This is supported by theoretical estimates of the limiting loss for acceptor-dominated materials with relevant background impurity levels [27]. Initially, it was assumed that lattice-mismatch-mediated strain was the driving force behind both the birefringence ($\mathrm{Re}\{\Delta n\}$) and the orientation-dependent absorption (governed by $\mathrm{Im}\{\Delta n\}$). However, owing to the cubic nature of the zincblende unit cell, an in-plane biaxial strain for (100)-oriented GaAs, as implemented here, will lower the symmetry from cubic to tetragonal. The optical axis will be along the illumination direction, so that no birefringence or absorption differences are possible. Nevertheless, birefringence occurs in our crystalline mirrors at a variety of wavelengths [14, 27] with apparently repeatable magnitude. It is assumed that a similar underlying process drives the anisotropy in both the index and free-carrier absorption.

A potential candidate for causing the observed polarization-dependent absorption is anisotropic strain relaxation as observed in InGaP-based materials [47] which breaks the system symmetry. To test this hypothesis, we simulated the free-carrier absorption caused by an additional 1% strain along the $[0\bar{1}1]$ direction. While we do not expect that such large additional strains are present in this system, the large imparted strain value facilitates the convergence of the simulations.

For these simulations we used density functional theory with the PBEsol exchange-correlation functional [48], as implemented in the Quantum-ESPRESSO package [49]. The electron-phonon matrix elements were modeled by a Fröhlich model, which has been shown to work well within the infrared region [50–52]. We used a rotated conventional unit cell, an energy cutoff of 100 Ry, and a $14 \times 20 \times 20$ **k**-point grid. Spin-orbit coupling was not included. The refractive index was determined using

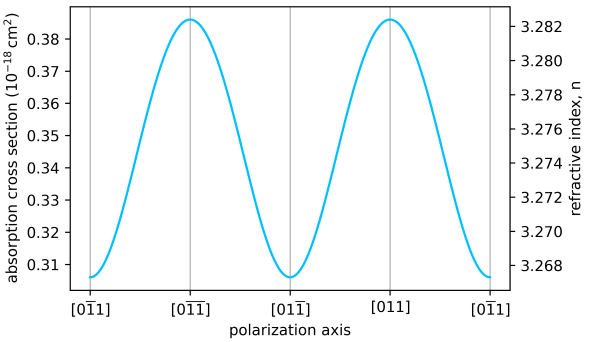

Fig. 2.9. Simulation of the orientation dependence of the photon absorption cross section and refractive index of uniaxially strained GaAs as a function of linear polarization direction. Results are given for a photon energy of 1.2 eV and in-plane compressive strain of 1% along the $[0\bar{1}1]$ direction. These values are chosen to expedite these proof of principle calculations.

a $50 \times 50 \times 50$ Wannier interpolated [53] **k**-point grid as implemented in the WANNIER90 package [54]. The underlying electronic structure was calculated using the HSE06 [55] hybrid functional, as implemented in the VASP package [56].

Figure 2.9 shows the calculated absorption cross section (the absorption coefficient divided by the free-carrier concentration) as a function of the illumination angle for photons with an energy of 1.2eV (corresponding to a wavelength of approximately 1.0μm). As with the large uniaxial strain value, a higher energy is probed to simplify these proof of principle calculations. Note that similar behavior is observed for other photon energies. The calculations show a polarization dependence similar to Fig. 2.8, indicating that anisotropic strain can cause the observed effect.

2.4 Conclusions and outlook

We successfully fabricated and optically characterized state-of-the-art substrate-transferred crystalline interference coatings at 4.54 µm. Optical losses were determined using a variety of experimental approaches to ultimately decompose coating transmittance, absorption, and scatter. Two independent CRD systems were used to determine the total loss, while an extension of the PCI measurement scheme to the mid-IR using a novel *in situ* "proxy pump" calibration technique was used to analyze absorption loss.

Transmittance was measured directly and calculated using a transmission matrix model based on SEM measurements of as-grown layer thicknesses and broadband FTS spectra.

The fact that many of the outlined measurement methods are based on a single FP-QCL makes the measurements easily extendable to a wide variety of wavelength regions. This lays the groundwork for their routine application in a production environment and will speed up extension of crystalline coating technology into the molecular fingerprint region.

In the course of our efforts, we observed a polarization dependence of absorption losses in the studied crystalline multilayer stacks, which, to the best of our knowledge, has not yet been reported in the literature. Initial proof of principle calculations show that anisotropic strain can lead to polarization-dependent free-carrier absorption and a polarization-dependent refractive index. More detailed experimental and theoretical investigations of this effect are in progress to determine the root cause of this anisotropic strain relaxation.

Our measurements confirm record-low levels of excess optical losses (scatter plus absorption) below 10 ppm, with $A + S = 7 \pm 4$ ppm in these coatings. With such low levels of excess optical loss, we have now demonstrated mid-IR mirrors capable of optical performance on par with their near-IR counterparts. Although the stop band of any individual mirror is currently limited by the index contrast of the GaAs/AlGaAs material system, the technology presented here is readily scalable to all wavelengths in the GaAs/AlGaAs transparency window, from the near-IR to beyond 10 µm, while future efforts involving alternative epitaxial material systems can lead to drastically broader stop bands of individual mirrors. This offers a bright outlook for diverse applications in the mid-IR spectral region, e.g., in future cavity-enhanced spectroscopy applications covering the molecular fingerprint region, laser stabilization, fundamental physics experiments as well as many other applications. In follow-on efforts it should be possible to produce optical resonators with center wavelengths in the range of 2 µm to 5 µm and a cavity finesse exceeding 100,000, a significant milestone in the development of the first mid-IR "super mirrors." Such exceptional levels of performance can be achieved via a minor design alteration, specifically reducing the transmittance of the interference coating to below 10 ppm. TMM calculations show that a transmittance of 8 ppm can be achieved at 4.5 µm with a full mirror stack of ∼33 µm in thickness (45.5 periods of GaAs/$Al_{0.92}Ga_{0.08}As$). Using the stacking approach employed here, the thickness of individual half mirror stacks would be below 17 µm, with state-of-the-art MBE generating a surface quality sufficient for direct bonding. We also note that this process would yield a coating surface quality (post-substrate transfer) with an RMS surface roughness below 0.2 nm, rendering optical scatter negligible. The absorption should be unaffected also, as there would be no change in the level of background doping, nor in the optical penetration depth into the multilayer.

Funding

Austrian Federal Ministry for Digital and Economic Affairs; National Foundation for Research, Technology and Development; Christian Doppler Research Association; Austrian Research Promotion Agency (865556); National Institute of Standards and Technology; National Research Council Postdoctoral Research Associateship Program; Austrian Science Fund (M2561-N36).

Acknowledgment

We acknowledge support by the Faculty Center for Nano Structure Research at the University of Vienna in supplying the infrastructure for SEM imaging. A portion of this work was performed in the UCSB Nanofabrication Facility.

Disclosures

GW, LWP, ASM, JF, OHH, GZ, DMB, AJF: Thorlabs Inc. (F); GDC, GWT, DB, DF, PH, CD: Thorlabs Inc. (E). Certain commercial equipment is identified in this paper in order to specify the experimental procedure adequately. Such identification is not intended to imply recommendation or endorsement by the National Institute of Standards and Technology, nor is it intended to imply that the equipment identified is necessarily the best available for the purpose.

Data availability

Data underlying the results presented in this paper are not publicly available at this time but may be obtained from the authors upon reasonable request.

Supplemental document

See 2.5 for supporting content.

References

[1] A. D. Ludlow, M. M. Boyd, J. Ye, E. Peik, and P. O. Schmidt, "Optical atomic clocks", Rev. Modern Phys. **87**, 637 (2015).

[2] J. L. Hall, "Nobel Lecture: Defining and measuring optical frequencies", Rev. Modern Phys. **78**, 1279 (2006).

[3] T. W. Hänsch, "Nobel Lecture: Passion for precision", Rev. Modern Phys. **78**, 1297 (2006).

[4] O. Kapon, R. Yitzhari, A. Palatnik, and Y. R. Tischler, "Vibrational Strong Light–Matter Coupling Using a Wavelength-Tunable Mid-infrared Open Microcavity", J. Phys. Chem. C **121**, 18845 (2017).

[5] B. P. Abbott, R. Abbott, T. D. Abbott, M. R. Abernathy, F. Acernese, K. Ackley, C. Adams, T. Adams, P. Addesso, R. X. Adhikari, et al., "Observation of gravitational waves from a binary black hole merger", Phys. Rev. Lett. **116**, 061102 (2016).

[6] T. Jin, J. Zhou, Z. Wang, R. Gutierrez-Osuna, C. Ahn, W. Hwang, K. Park, and P. T. Lin, "Real-Time Gas Mixture Analysis Using Mid-Infrared Membrane Microcavities", Anal. Chem. **90**, 4348 (2018).

[7] T. P. Wrobel and R. Bhargava, "Infrared Spectroscopic Imaging Advances as an Analytical Technology for Biomedical Sciences", Anal. Chem. **90**, 1444 (2018).

[8] L. D. Carr, D. DeMille, R. V. Krems, and J. Ye, "Cold and ultracold molecules: science, technology and applications", New J. Phys. **11**, 055049 (2009).

[9] J. L. Bohn, A. M. Rey, and J. Ye, "Cold molecules: Progress in quantum engineering of chemistry and quantum matter", Science **357**, 1002 (2017).

[10] J.-P. Karr, L. Hilico, J. C. J. Koelemeij, and V. I. Korobov, "Hydrogen molecular ions for improved determination of fundamental constants", Phys. Rev. A **94**, 050501 (2016).

[11] A. Foltynowicz, P. Masłowski, A. J. Fleisher, B. J. Bjork, and J. Ye, "Cavity-enhanced optical frequency comb spectroscopy in the mid-infrared application to trace detection of hydrogen peroxide", Appl. Phys. B **110**, 163 (2013).

[12] G. Zhao, D. M. Bailey, A. J. Fleisher, J. T. Hodges, and K. K. Lehmann, "Doppler-free two-photon cavity ring-down spectroscopy of a nitrous oxide (N_2O) vibrational overtone transition", Phys. Rev. A **101**, 062509 (2020).

[13] A. Ueda, N. Uehara, K. Uchisawa, K.-i. Ueda, H. Sekiguchi, T. Mitake, K. Nakamura, N. Kitajima, and I. Kataoka, "Ultra-high quality cavity with 1.5 ppm loss at 1064 nm", Opt. Rev. **3**, 369 (1996).

[14] C. J. Hood, H. J. Kimble, and J. Ye, "Characterization of high-finesse mirrors: Loss, phase shifts, and mode structure in an optical cavity", Phys. Rev. A **64**, 033804 (2001).

[15] H. Huang and K. K. Lehmann, "Sensitivity Limits of Continuous Wave Cavity Ring-Down Spectroscopy", J. Phys. Chem. A **117**, 13399 (2013).

[16] K. K. Lehmann, "Resonance enhanced two-photon cavity ring-down spectroscopy of vibrational overtone bands: A proposal", J. Chem. Phys. **151**, 144201 (2019).

[17] G. Harry, T. P. Bodiya, and R. DeSalvo, eds., *Optical Coatings and Thermal Noise in Precision Measurement*, 1st ed. (Cambridge University Press, Cambridge, 2012).

[18] G. D. Cole, W. Zhang, M. J. Martin, J. Ye, and M. Aspelmeyer, "Tenfold reduction of Brownian noise in high-reflectivity optical coatings", Nat. Photonics **7**, 644 (2013).

[19] W. Heiss, T. Schwarzl, J. Roither, G. Springholz, M. Aigle, H. Pascher, K. Biermann, and K. Reimann, "Epitaxial Bragg mirrors for the mid-infrared and their applications", Prog. Quantum Electron. **25**, 193 (2001).

[20] J. Fan, X. Liu, L. Ouyang, R. E. Pimpinella, M. Dobrowolska, J. K. Furdyna, D. J. Smith, and Y.-H. Zhang, "Molecular beam epitaxial growth of high-reflectivity and broad-bandwidth ZnTe/GaSb distributed Bragg reflectors", J. Vac. Sci. Technol. B Nanotechnol. Microelectron.: Mater. Process. Meas. Phenom. **31**, 03C109 (2013).

[21] G. D. Cole, W. Zhang, B. J. Bjork, D. Follman, P. Heu, C. Deutsch, L. Sonderhouse, J. Robinson, C. Franz, A. Alexandrovski, et al., "High-performance near- and mid-infrared crystalline coatings", Optica **3**, 647 (2016).

[22] J. Cripe, N. Aggarwal, R. Lanza, A. Libson, R. Singh, P. Heu, D. Follman, G. D. Cole, N. Mavalvala, and T. Corbitt, "Measurement of quantum back action in the audio band at room temperature", Nature **568**, 364 (2019).

[23] N. Aggarwal, T. J. Cullen, J. Cripe, G. D. Cole, R. Lanza, A. Libson, D. Follman, P. Heu, T. Corbitt, and N. Mavalvala, "Room-temperature optomechanical squeezing", Nat. Phys. **16**, 784 (2020).

[24] M. J. Yap, J. Cripe, G. L. Mansell, T. G. McRae, R. L. Ward, B. J. J. Slagmolen, P. Heu, D. Follman, G. D. Cole, T. Corbitt, et al., "Broadband reduction of quantum radiation pressure noise via squeezed light injection", Nat. Photonics **14**, 19 (2020).

[25] B. J. Bjork, T. Q. Bui, O. H. Heckl, P. B. Changala, B. Spaun, P. Heu, D. Follman, C. Deutsch, G. D. Cole, M. Aspelmeyer, et al., "Direct frequency comb measurement of OD + CO → DOCO kinetics", Science **354**, 444 (2016).

[26] G. W. Truong, G. Winkler, T. Zederbauer, D. Bachmann, P. Heu, D. Follman, M. E. White, O. H. Heckl, and G. D. Cole, "Near-infrared scanning cavity ringdown for optical loss characterization of supermirrors", Opt. Express **27**, 19141 (2019).

[27] I. Galli, S. Bartalini, R. Ballerini, M. Barucci, P. Cancio, M. De Pas, G. Giusfredi, D. Mazzotti, N. Akikusa, and P. De Natale, "Spectroscopic detection of radiocarbon dioxide at parts-per-quadrillion sensitivity", Optica **3**, 385 (2016).

[28] G. Genoud, M. Vainio, H. Phillips, J. Dean, and M. Merimaa, "Radiocarbon dioxide detection based on cavity ring-down spectroscopy and a quantum cascade laser", Opt. Lett. **40**, 1342 (2015).

[29] A. D. McCartt, T. J. Ognibene, G. Bench, and K. W. Turteltaub, "Quantifying Carbon-14 for Biology Using Cavity Ring-Down Spectroscopy", Anal. Chem. **88**, 8714 (2016).

[30] A. J. Fleisher, D. A. Long, Q. Liu, L. Gameson, and J. T. Hodges, "Optical Measurement of Radiocarbon below Unity Fraction Modern by Linear Absorption Spectroscopy", J. Phys. Chem. Lett. **8**, 4550 (2017).

[31] G. Genoud, J. Lehmuskoski, S. Bell, V. Palonen, M. Oinonen, M.-L. Koskinen-Soivi, and M. Reinikainen, "Laser Spectroscopy for Monitoring of Radiocarbon in Atmospheric Samples", Anal. Chem. **91**, 12315 (2019).

[32] M. Fatima, T. Hausmaninger, T. Tomberg, T. Hieta, J. Karhu, M. Vainio, and G. Genoud, "Part-per-billion level radiocarbon dioxide detection using photoacoustic spectroscopy", in Conference on Lasers and Electro-Optics (2020), ATu3I.3.

[33] A. Alexandrovski, M. Fejer, A. Markosyan, and R. Route, "Photothermal common-path interferometry (PCI): new developments", in Solid State Lasers XVIII: Technology and Devices, Vol. 7193, edited by W. A. Clarkson, N. Hodgson, and R. K. Shori, Proceedings of SPIE (2009), p. 71930D.

[34] H. Davies, "The reflection of electromagnetic waves from a rough surface", Proc. IEE - IV: Inst. Monogr. **101**, 209 (1954).

[35] C. C. Katsidis and D. I. Siapkas, "General transfer-matrix method for optical multilayer systems with coherent, partially coherent, and incoherent interference", Appl. Opt. **41**, 3978 (2002).

[36] S. J. Byrnes, *Multilayer optical calculations*, (2020) arXiv:1603.02720v5, preprint.

[37] M. A. Afromowitz, "Refractive index of $Ga_{1-x}Al_xAs$", Solid State Commun. **15**, 59 (1974).

[38] C. Deutsch, G. D. Cole, D. Follman, P. Heu, B. J. Bjork, C. Franz, A. Alexandrovski, O. H. Heckl, J. Ye, and M. Aspelmeyer, "Mid-infrared crystalline mirrors with ultralow optical losses", in Proceedings 2017 European Conference on Lasers and Electro-Optics and European Quantum Electronics Conference (2017), CE_3_3.

[39] P. Koch, G. D. Cole, C. Deutsch, D. Follman, P. Heu, M. Kinley-Hanlon, R. Kirchhoff, S. Leavey, J. Lehmann, P. Oppermann, et al., "Thickness uniformity measurements and damage threshold tests of large-area GaAs/AlGaAs crystalline coatings for precision interferometry", Opt. Express **27**, 36731 (2019).

[40] D. Chandler-Horowitz and P. M. Amirtharaj, "High-accuracy, midinfrared (450 $cm^{-1} \leq \omega \leq$ 4000 cm^{-1}) refractive index values of silicon", J. Appl. Phys. **97**, 123526 (2005).

[41] D. Z. Anderson, J. C. Frisch, and C. S. Masser, "Mirror reflectometer based on optical cavity decay time", Appl. Opt. **23**, 1238 (1984).

[42] G.-W. Truong and G. Winkler, *Digital delay generator/gate based on the Teensy microcontroller*, 2019.

[43] Y. Chen, K. K. Lehmann, J. Kessler, B. S. Lollar, G. L. Couloume, and T. C. Onstott, "Measurement of the $^{13}C/^{12}C$ of Atmospheric CH_4 Using Near-Infrared (NIR) Cavity Ring-Down Spectroscopy", Anal. Chem. **85**, 11250 (2013).

[44] E. Theocharous, "Absolute linearity measurements on a PbSe detector in the infrared", Infrared Phys. Techn. **50**, 63 (2007).

[45] A. L. Alexandrovski, A. S. Markosyan, H. Cai, and M. M. Fejer, "Photothermal measurements of absorption in LBO with a "proxy pump" calibration technique", in Laser-Induced Damage in Optical Materials 2017, Vol. 10447, edited by G. J. Exarhos, V. E. Gruzdev, J. A. Menapace, D. Ristau, and M. J. Soileau, Proceedings of SPIE (2017), p. 104471D.

[46] A. J. Fleisher, D. A. Long, Q. Liu, and J. T. Hodges, "Precision interferometric measurements of mirror birefringence in high-finesse optical resonators", Phys. Rev. A **93**, 013833 (2016).

[47] M. Bückle, V. C. Hauber, G. D. Cole, C. Gärtner, U. Zeimer, J. Grenzer, and E. M. Weig, "Stress control of tensile-strained $In_{1-x}Ga_{1-x}P$ nanomechanical string resonators", Appl. Phys. Lett. **113**, 201903 (2018).

[48] J. P. Perdew, A. Ruzsinszky, G. I. Csonka, O. A. Vydrov, G. E. Scuseria, L. A. Constantin, X. Zhou, and K. Burke, "Restoring the Density-Gradient Expansion for Exchange in Solids and Surfaces", Phys. Rev. Lett. **100**, 136406 (2008).

[49] P. Giannozzi, S. Baroni, N. Bonini, M. Calandra, R. Car, C. Cavazzoni, D. Ceresoli, G. L. Chiarotti, M. Cococcioni, I. Dabo, et al., "QUANTUM ESPRESSO: a modular and open-source software project for quantum simulations of materials", J. Phys.: Condens. Matter **21**, 395502 (2009).

[50] H. Peelaers, E. Kioupakis, and C. G. Van De Walle, "Fundamental limits on optical transparency of transparent conducting oxides: Free-carrier absorption in SnO_2", Appl. Phys. Lett. **100**, 011914 (2012).

[51] H. Peelaers, E. Kioupakis, and C. G. Van De Walle, "Free-carrier absorption in transparent conducting oxides: Phonon and impurity scattering in SnO_2", Phys. Rev. B **92**, 235201 (2015).

[52] H. Peelaers, E. Kioupakis, and C. G. Van De Walle, "Limitations of In_2O_3 as a transparent conducting oxide", Appl. Phys. Lett. **115**, 082105 (2019).

[53] I. Souza, N. Marzari, and D. Vanderbilt, "Maximally localized Wannier functions for entangled energy bands", Phys. Rev. B **65**, 035109 (2001).

[54] A. A. Mostofi, J. R. Yates, Y.-S. Lee, I. Souza, D. Vanderbilt, and N. Marzari, "wannier90: a tool for obtaining maximally-localised wannier functions", Comput. Phys. Commun. **178**, 685 (2008).

[55] J. Heyd, G. E. Scuseria, and M. Ernzerhof, "Hybrid functionals based on a screened Coulomb potential", J. Chem. Phys. **118**, 8207 (2003).

[56] G. Kresse and J. Furthmüller, "Efficient iterative schemes for *ab initio* total-energy calculations using a plane-wave basis set", Phys. Rev. B **54**, 11169 (1996).

Mid-infrared interference coatings with excess optical loss below 10 ppm: Supplement

Bibliographical information

The contents of this section were originally published as

> G. Winkler et al., *Mid-infrared interference coatings with excess optical loss below 10 ppm: Supplement* (2021), DOI: 10.6084/M9.FIGSHARE.14271983.

including the following publication notes:

The contents of the supplement remain unchanged in this reprint. The formatting has been carefully adapted to the overall style of the doctoral thesis. Furthermore, the only citation in the supplement—now in Section 2.5—was pointing to the wrong reference of the main article. This will be reported to the journal as an erratum. The original title and authors correspond to the chapter title and authors. Author affiliations are given as they appear in the original publication.

2.5 Mid-infrared monocrystalline interference coatings with excess optical loss below 10 ppm: Supplemental document

Prevention of etaloning in swept-frequency cavity ring-down measurements

The external-cavity quantum cascade laser (EC-QCL) swept-frequency cavity ring-down instrument at the National Institute of Standards and Technology achieved single cavity-mode excitation, and therefore was capable of resolving stray etalons formed by spurious reflections involving one of the cavity mirrors. To reduce the influence of these coupled cavity effects [1], broader frequency scans of the EC-QCL were performed by increasing the intensity of the laser current dither to cover multiple longitudinal modes. Cavity decay signals were then triggered at each longitudinal mode and values of τ were recorded, searching for periodic modulation in the apparent optical losses which would indicate a coupled cavity. With the optical cavity aligned on-axis, the measured values of τ revealed one strong etalon with a characteristic frequency of $\nu_{\text{etalon}} \approx 6.4\nu_{\text{fsr}} = 6.1\,\text{GHz}$, as depicted in Fig. 2.10 (left). This value was in reasonable agreement with an etalon formed by the AR coated faces of the mirrors themselves, located on the opposite sides of their silicon substrate with $d = 0.635\,\text{cm}$ and material index $n \approx 3.42$. (i.e. 6.9 GHz).

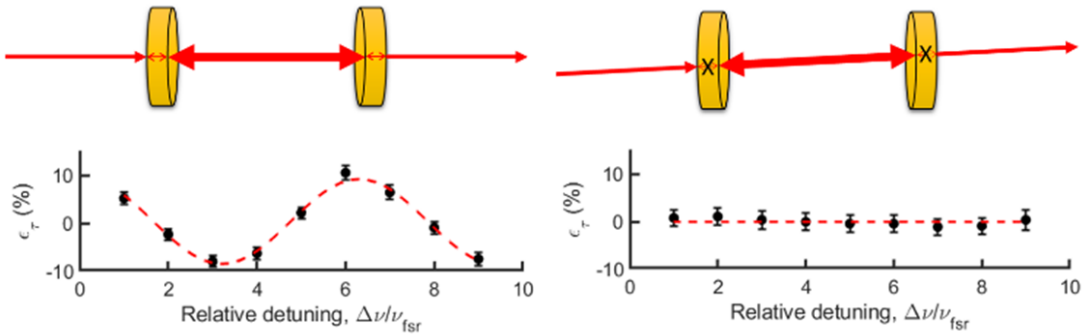

Fig. 2.10. Cavity alignment for the reduction of parasitic etalons. Left: Illustration of on-axis cavity alignment and observed etalon attributed to coupling of scattered light between the AR and HR mirror faces. Right: Equivalent depiction of new cavity alignment that reduced AR-HR face etalons. In both cases, $\epsilon_\tau = \tau/\bar{\tau} - 1$ is the fractional change in τ relative to the average value $\bar{\tau}$.

The absence of significant etaloning with those optical components was confirmed by the inclusion of additional neutral density filters before and after the cavity to reduce the coupled cavity finesse, a procedure which had no effect on the etalon shown in Fig. 3. We then performed the following additional cavity alignment steps which effectively eliminated the etalon. First, the photodetector position was translated in the plane of the optical table using a micrometer and linear optomechanical stage. With the new photodetector location acting as a fixed target, laser alignment to the cavity was adjusted until high throughput and good mode matching conditions were again achieved. The procedure forced the cavity alignment to slowly walk off the axis formed by the planar AR-coated faces, or off the radial center of the planar-concave mirror substrates, effectively creating a wedged substrate by reducing parallelism between the planar AR- and concave HR-faces as depicted in Fig. 2.10 (right). The procedure was repeated until the longitudinal mode frequency scan showed only minor variations in the relative fractional time constant $\epsilon_\tau = \tau/\bar{\tau} - 1$, where $\bar{\tau}$ is the average ringdown time over all longitudinal modes.

References

[1] J. Courtois and J. T. Hodges, “Coupled-cavity ring-down spectroscopy technique”, Opt. Lett. **37**, 3354 (2012).

3 Simultaneous measurement of mid-infrared refractive indices in thin-film heterostructures: Methodology and results for GaAs/AlGaAs

L. W. Perner[1,2], G.-W. Truong[3], D. Follman[3], M. Prinz[1,2], G. Winkler[1], S. Puchegger[4], G. D. Cole[3], O. H. Heckl[1]

[1]Christian Doppler Laboratory for Mid-IR Spectroscopy and Semiconductor Optics, Faculty Center for Nano Structure Research, Faculty of Physics, University of Vienna, Boltzmanngasse 5, 1090 Vienna, Austria

[2]Vienna Doctoral School in Physics, University of Vienna, Boltzmanngasse 5, 1090 Vienna, Austria

[3]Thorlabs Crystalline Solutions, 114 E Haley St., Suite G, Santa Barbara, California 93101, USA

[4]Faculty Center for Nano Structure Research, Faculty of Physics, University of Vienna, Boltzmanngasse 5, 1090 Vienna, Austria

> The first principle is that you must not fool yourself– and you are the easiest person to fool. So you have to be very careful about that. After you've not fooled yourself, it's easy not to fool other scientists. You just have to be honest in a conventional way after that.
>
> *(Richard P. Feynman, 1974)*

Bibliographic information

The contents of this chapter were originally published in *Physical Review Research* as

> L. W. Perner et al., "Simultaneous measurement of mid-infrared refractive indices in thin-film heterostructures: Methodology and results for GaAs/AlGaAs", Phys. Rev. Research **5**, 033048 (2023), DOI: 10.1103/PhysRevResearch.5.033048.

including the following publication notes:

> Received 17 January 2023; accepted 22 May 2023; published 25 July 2023

The contents of the article remain unchanged in this reprint. The formatting has been carefully adapted to the overall style of the doctoral thesis. The original title and authors correspond to the chapter title and authors. Author affiliations are given as they appear in the original publication.

Author contributions

For the here-presented results, I lead the development of the general method to measure refractive indices, with initial inputs from Georg Winkler. I then carried out the photometrically accurate Fourier-transform spectrometry, using crystalline multilayer samples provided by Garrett Cole, David Follman and Gar-Wing Truong. I then processed the crystalline samples following instructions by David Follman and Garrett Cole. Subsequently, I generated the final scanning-electron microscopy images, weighing on Stephan Puchegger's expertise to refine the process in previous measurements. Furthermore, supported by Maximilian Prinz, I wrote the scripts for data analysis, which I then used to generate the published results. I also lead the writing of the manuscript, contributing substantial parts and incorporating various comments from the co-authors.

Abstract

We present our results for simultaneous measurement of the refractive indices of gallium arsenide (GaAs) and aluminum gallium arsenide ($Al_xGa_{1-x}As$) in the spectral region from 2.0 µm to 7.1 µm (5000 cm^{-1} to 1400 cm^{-1}). We obtain these values from a monocrystalline superlattice Bragg mirror of excellent purity (background doping $\leq 1 \times 10^{-14}$ cm^{-3}), grown via molecular beam epitaxy. To recover the refractive indices over such a broad wavelength range, we fit a dispersion model for each material. In a novel combination of well-established methods, we measure both a photometrically accurate transmittance spectrum of the Bragg mirror via Fourier-transform infrared spectrometry and the individual physical layer thicknesses of the structure via scanning electron microscopy. To infer the uncertainty of the refractive index values, we estimate relevant measurement uncertainties and propagate them via a Monte Carlo method. This highly-adaptable approach conclusively yields propagated relative uncertainties on the order of 10^{-4} over the measured spectral range for both GaAs and $Al_{0.929}Ga_{0.071}As$. The fitted model can also approximate the refractive index for MBE-grown $Al_xGa_{1-x}As$ for $0 \leq x \leq 1$. Both these updated values and the measurement approach will be essential in the design, fabrication, and characterization of next-generation active and passive optical devices in a spectral region that is of high interest in many fields, e.g., laser design and cavity-enhanced spectroscopy in the mid-infrared.

3.1 Introduction

Heterostructures based on gallium arsenide (GaAs) and aluminum gallium arsenide ($Al_xGa_{1-x}As$, where x denotes the AlAs mole fraction) are paramount in the design and production of a multitude of active and passive (electro-)optical devices ranging from light sources, such as vertical-cavity surface-emitting lasers (VCSELs) [1], superluminescent diodes [2] and quantum cascade lasers (QCLs) [3], plus detection devices, such as quantum cascade detectors (QCDs), quantum-well infrared photodetectors (QWIPs) [4], and megapixel infrared camera sensors based on QWIP technology [5], to highly-reflective (HR) distributed Bragg reflectors (DBRs) [6–8], semiconductor saturable absorber mirrors (SESAMs) [9, 10], and HR optomechanical resonators [11]. Owing to mature fabrication technologies, notably molecular beam epitaxy (MBE) [12], $GaAs/Al_xGa_{1-x}As$-based devices find extensive applications in the near-infrared (NIR) and mid-infrared (MIR) wavelength range. For example, a recently-developed technology allows the transfer of MBE-grown $GaAs/Al_xGa_{1-x}As$ HR DBRs to curved optical substrates, making the material system relevant for applications from gravitational wave detection [13, 14] to ultranarrow linewidth laser stabilization in the NIR [15]. This substrate-transfer method was extended to the MIR wavelength range [16–18], enabling ultralow excess loss at MIR wavelengths up to 4.5 µm, making substrate-transferred $GaAs/Al_xGa_{1-x}As$-based DBRs a key technology for advances in cavity-enhanced MIR spectroscopy applications [19, 20].

Despite the extensive application of $GaAs/Al_xGa_{1-x}As$ in optical devices, there is a lack of recent accurate and precise data for its optical properties, especially refractive index n, in the MIR wavelength range (>2 µm). The existing literature values for these materials are largely based on the characterization of bulk samples rather than MBE-grown multilayers. Probing such samples, along with often incomplete reporting of measurement conditions, leads to substantial differences in refractive index, especially when comparing samples grown by different methods [21]. This discrepancy, likely due to variations in growth, background doping, and purity levels (see Fig. 3.6), calls for updated literature values for GaAs, $Al_xGa_{1-x}As$, among other materials [22].

For $Al_xGa_{1-x}As$, which is used with a wide variety of mole fractions x, the latest semiempirical model that allows for an arbitrary x was published in 1974 [23], where model parameters were obtained from a fit to measurement data obtained in the NIR range (approx. from 680 nm to 1030 nm) on samples grown via liquid-phase epitaxy (LPE) [24]. More recent studies for GaAs and $Al_xGa_{1-x}As$ exist [25–27]. However, these either focus on the NIR spectral region or are of insufficient accuracy for many of the above applications, which rely on MBE-grown $GaAs/Al_xGa_{1-x}As$, due to discrepancies in measurement conditions and sample material (e.g., when using n measured for bulk material in the design of thin-film heterostructures).

In this study, we introduce updated refractive index values for high-purity MBE-grown GaAs and $Al_xGa_{1-x}As$ in the spectral range from 2 µm to 7.1 µm, measured simultaneously via a versatile method (see Fig. 3.1). While the method is adaptable to different measurement devices, the presented results leverage two widely-available instruments, a Fourier-transform infrared (FTIR) spectrometer and a field-emission scanning electron microscope (SEM), to probe a state-of-the-art $GaAs/Al_xGa_{1-x}As$ DBR. This DBR, with a center wavelength of approx. 4.45 µm, has ultralow absorption and background doping [17, 18], making it an ideal specimen for probing material optical properties. A curve-fitting routine, based on the transmission matrix method (TMM), is used to infer both refractive indices, where each material's dispersion is captured by a semiempirical model [23]. Measurement uncertainties are propagated to the final n results using a Monte Carlo-type method.

3.2 Model and theory

3.2.1 Transmission matrix method

A well-established means of modeling the optical response (reflectance R and/or transmittance T) of an optical multilayer structure is the TMM [28–30]. In this approach, a 2×2 matrix represents each interface and the propagation through a given material of refractive index n [29], effectively relating the reflected/transmitted wave to the incoming wave via the complex reflection/transmission amplitude coefficients. The TMM calculates the optical response of a multilayer based on the individual physical layer thicknesses d_i and their respective refractive indices n_i.

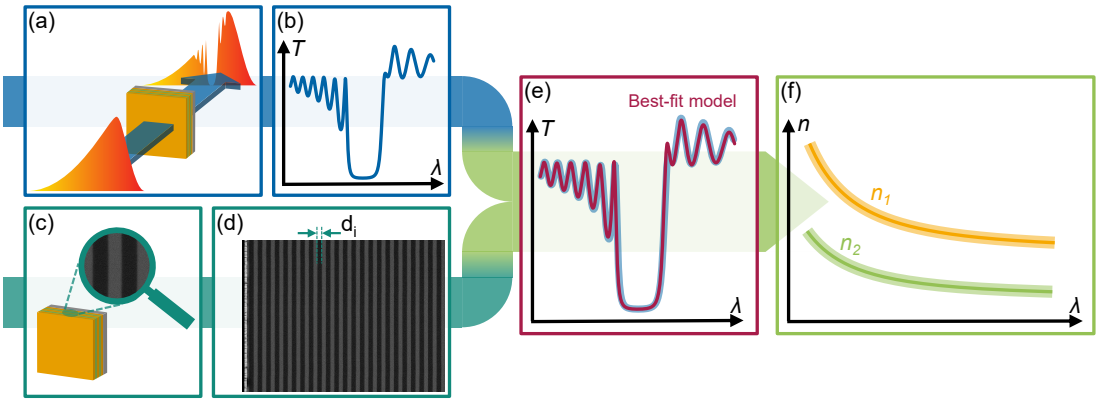

Fig. 3.1. Schematic outline of our approach, which relies on two measurements of a thin-film heterostructure: (a) First, a spectrometric transmittance (or reflectance, not depicted) measurement is carried out. (b) From this, we acquire the optical response of the sample. (c) Second, a cross-sectional SEM (or TEM/AFM, not depicted) micrograph. (d) From this, we extract the individual layer thicknesses d_i. (e) These two measurements are used for a TMM-based best-fit modeling approach. (f) Finally, from this fit, we infer both refractive indices, n_1 and n_2, as well as their respective uncertainties [using a Monte Carlo-type propagation of the measurement uncertainties from (a)–(d)].

In principle, the TMM can incorporate absorbance within the layers via the complex refractive index $\tilde{n} = n + ik$, with the extinction coefficient $k = \lambda_0\alpha/4\pi$ and α the absorption coefficient. However, previous studies have shown that the absorbance of our structure is <10 ppm (i.e., $<10 \times 10^{-6}$) [16–18], which is below both the observed uncertainty in FTIR imaging [see Fig. 3.2(b)] as well as our targeted propagated relative uncertainty of c. 10^{-4}. Hence, we model both materials as transparent (i.e., with $k = 0$).

Due to its reliance on matrix multiplications, numerical calculations based on the TMM can be implemented very efficiently. We use the recently-developed `tmm-fast` package [30], implemented in Python 3. This highly-optimized implementation allows for low computation times, even for many repeated calculations, as is necessary for the nonlinear least-squares curve fitting routines we use. We adapt the `tmm-fast` algorithm to accommodate the treatment of thick layers where interference can be neglected, such as in the case of the MBE seed wafer, following the method described in Ref. [29].

3.2.2 Refractive index model

As our method involves a nonlinear least-squares fit over a broad wavelength range (2 µm to 7.1 µm) dispersion, i.e., the change of the refractive index with respect to wavelength $dn/d\lambda$, must be taken into account. In principle, several different approaches to modeling refractive indices exist, roughly divided into empirical, semiempirical, and theoretical models. The choice of an appropriate model depends on several considerations. These include the electronic and optical properties of the material in the wavelength range of interest.

For GaAs/$Al_xGa_{1-x}As$, several models have been used to obtain $n(\lambda)$. Empirical models are predominantly derived from the well-known Sellmeier equation [31]. The latter was used, e.g., by Skauli *et al.*, together with another model by Pikhtin and Yas'kov, to obtain the refractive index of GaAs in a range 0.97–17 µm [25]. Owing to a high number of free parameters (e.g., seven parameters per material in the case of both models in [25]), these models can capture variations in measurement data well. While this is generally desired, there is a potential for overfitting, as many free parameters allow for the model fit to extract residual random and/or systematic variations in the data points used for regression analysis.

In this study, we use a semiempirical model developed specifically for GaAs and $Al_xGa_{1-x}As$ [23], given by the expression

$$n^2(E) - 1 = \frac{\eta}{\pi}\left[\frac{E_f^4 - E_\Gamma^4}{2} + \left(E_f^2 - E_\Gamma^2\right)E^2 + \ln\left(\frac{E_f^2 - E^2}{E_\Gamma^2 - E^2}\right)E^4\right] \tag{3.1}$$

where $E = hc/\lambda$ is the photon energy, E_Γ is the bandgap energy (used in units of eV throughout this work). E_f and η are to be determined empirically, effectively approximating the interband optical transitions as a function $\epsilon_2 = \eta E^4$ for $E_\Gamma < E < E_f$ ($\epsilon_2 = 0$ otherwise).

The lowest direct bandgap energy for pure GaAs

and AlAs are given by $E_{\Gamma,\mathrm{GaAs}} = 1.424(1)$ eV (measured at a temperature of 297 K) [21] and $E_{\Gamma,\mathrm{AlAs}} = 3.018$ eV (measured at room temperature, given without uncertainty) [32, pp. 192, 193], respectively. Aspnes *et al.* showed that for arbitrary x, E_Γ is well approximated by

$$E_\Gamma(x) = 1.424 + 1.721x - 1.437x^2 + 1.310x^3 \qquad (3.2)$$

which allows us to determine $E_\Gamma(x)$ based on an independent measurement of x. As shown in [23], the expression in (3.1) closely reproduced the refractive index of GaAs for wavelengths from 0.895 µm to 1.7 µm, with similar results for AlAs. We note that Ref. [23] also gives an interpolation scheme that can be used to approximate n for different x based on our results below.

In an effort to avoid bias introduced by the model selection, we compare these results to a fit using the so-called single effective oscillator (SEO) model [33], which, while not suited for the NIR, approximates n exceptionally well for $E \ll E_{\Gamma,\mathrm{GaAs}}$ ($\lambda \geq 2$ µm) [23, 26]. According to this model [33], the refractive index n of a crystalline material at a photon energy E far below the bandgap is well approximated by

$$n^2(E) - 1 = \frac{E_0 E_d}{E_0^2 - E^2} \qquad (3.3)$$

In this approximation, the interband optical transitions are considered as a single dipole transition at energy E_0, with an effective oscillator strength of $\pi E_d/2$. Hence, the dispersion of GaAs/Al_xGa_{1-x}As in the MIR range can be adequately modeled by fitting only two free parameters, E_0 and E_d, as was shown in Ref. [26].

3.2.3 Monte Carlo error propagation

We use a Monte Carlo-type routine to propagate the measured uncertainties to the best-fit model parameters. This approach is robust to common systematic measurement errors because the refractive indices are tightly constrained by the measured quantities.

For the purpose of uncertainty propagation, the model can be described as a function

$$T = \mathrm{TMM}(d_i, n_{\mathrm{Subst}}, n_{\mathrm{GaAs}}, n_{\mathrm{AlGaAs}}) \qquad (3.4)$$

denoting the transmittance T as a function of the layer thicknesses d_i and refractive indices n. The fitted parameters n_{GaAs} and n_{AlGaAs} are described according to Eqs. (3.1)–(3.3). Here, T, d_i, and n_{Subst} represent measured quantities with associated uncertainties. Hence, our method involves using measured quantities not only in the data the model is fit to (the T measured via FTIR), but also in the parameters used to seed the model (d_i and n_{Subst}). Since the TMM represents a complicated model function, and a nonlinear least-squares fit routine is used, error propagation to the best-fit parameters is not straightforward and no standardized procedure exists.

To overcome this challenge, we use a Monte Carlo approach to calculate the propagated uncertainty: For each run, we randomly pick a certain realization of the measurement values [layer thicknesses d_i and transmittance values $T(\lambda)$] from distributions based on their respective measurement uncertainties [as given in Figs. 3.5(b) and 3.2(b)]. We repeat this process many times, yielding slightly different sets of parameters that vary within the measurement uncertainties. We then use each set for the same curve-fitting exercise, in which the dispersion parameters for both materials are recorded. This results in datasets for each fit parameter that also show variation as a consequence of the uncertainty in the measurement data.

Finally, for each set of parameters, the refractive index $n(\lambda)$ is calculated for both materials. It is of note that the uncertainty in n is much smaller than what would result from Gaussian error propagation because the fitted parameters show appreciable covariance with the input parameters taken from measurement and literature values. This is best seen when comparing the uncertainties resulting from fitting Eq. (3.1) vs Eq. (3.3): The former requires literature and measurement values for E_Γ and x with associated additional uncertainties when compared to the latter. Still, this leads to a negligible difference in the observed standard uncertainty of n.

3.3 Experiment

The basic idea of our approach is the following: On the one hand, the optical response, in our case the transmittance T, of a transparent optical system can be accurately modeled via TMM if the physical structure (i.e., layer thicknesses) and the associated refractive indices are known. On the other hand, the transmittance is accessible to optical probing. As a result, knowing both the measured optical response as well

as the material composition and layer thicknesses of an optical structure allows us to determine the refractive indices. This means that the refractive indices can be uniquely defined for a two-material structure that exhibits a characteristic optical response in the wavelength range of interest.

While this paper details results for GaAs/$Al_xGa_{1-x}As$, the underlying measurement principle (combining knowledge of the optical response with measurements of the physical structure of a thin-film multilayer to simultaneously obtain the refractive indices of both materials) is much broader in its applicability, as is shown in Fig. 3.1. It can be adapted for different samples, measurement devices, and spectral ranges. In this study, data collection consists of two independent measurements:

(i) obtaining a photometrically accurate transmittance T spectrum via Fourier-transform infrared (FTIR) spectrometry and

(ii) measuring individual physical layer thicknesses d_i via calibrated SEM metrology.

As explained in Sec. 3.2.1, the TMM relates the optical layer thicknesses to the optical response of a layered system.

3.3.1 Fabrication and description of the GaAs/$Al_xGa_{1-x}As$ sample

We designed the sample under test to serve as half of a distributed Bragg reflector (DBR) structure centered at $\lambda_d = 4.5\,\mu m$. Nominally, this structure consists of 22.5 periods of $Al_xGa_{1-x}As$/GaAs layer pairs, with an optical layer thickness of $\lambda_d/4$, terminated by a single $\lambda_d/8$-thickness GaAs cap (46 layers total) to avoid exposure of $Al_xGa_{1-x}As$ to air, preventing oxidation. The target AlAs mole fraction in the $Al_xGa_{1-x}As$ layers was $x = 0.92$.

Based on the above design, a DBR specimen is deposited via MBE on a [001]-oriented semi-insulating (GaAs with As antisite defects) GaAs seed wafer with a diameter of 15 cm and a nominal thickness of $675 \pm 25\,\mu m$. From this as-grown structure (seed wafer plus MBE-deposited heterostructure), we cleave a rectangular die of $2 \times 2\,cm^2$, which serves as the sample for all parts of this study. After growth, the AlAs mole fraction x is estimated to be $92.9 \pm 3.0\%$ based on x-ray diffraction (XRD) measurements performed by the epitaxial material supplier. Here, the uncertainty represents a conservative estimate based on data from [34, 35]. In our analysis, we assume that the mole fraction x is the same for all $Al_xGa_{1-x}As$ layers and that interfaces between the layers are abrupt (i.e., that n changes over a distance $\ll \lambda$).

Recently, a two-mirror cavity using 44.5-period DBR mirrors fabricated with material from the same growth run demonstrated a finesse of 230 000, corresponding to a per-mirror excess loss (absorption plus scatter) of 4.27 ± 0.52 ppm. From this an average extinction coefficient $k < 10^{-6}$ was extracted, suggesting background doping levels of $\leq 10^{-14}\,cm^{-3}$ [18]. This high purity makes the multilayer structure an ideal specimen to extract the refractive index n of both materials from an optical measurement.

3.3.2 Transmission spectrum via Fourier-transform infrared spectrometry

We obtain transmittance T spectra using a commercially available vacuum FTIR spectrometer (Bruker Vertex 80v). As described below, the necessary photometric accuracy was obtained by thorough calibration and rigorous control of measurement conditions.

Measurement conditions and parameters

To achieve excellent photometric accuracy, we thoroughly characterize the FTIR device and optimize the measurement parameters. From these efforts, we find that a SiC globar-type light source with a 2-mm aperture is optimal. The aperture size is chosen to maximize throughput while obtaining a well-collimated beam (excluding influence on resolution due to a large source diameter). We use a standard KBr beamsplitter for optimal modulation efficiency over the wavelength region of interest. The scan speed of the moving interferometer mirror is set to 10 kHz (corresponding to a physical scan speed of c. $0.32\,cm\,s^{-1}$), limited by the RF-frequency bandwidth of the employed DLaTGS pyroelectric detector. We select this detector to minimize systematic errors due to nonlinear detector response, owing to its excellent linearity and flat detectivity $D^*(\lambda)$ over our measurement range [36, 37]. We verified the wavelength calibration of the FTIR by comparing the spectrum of a polystyrene filter with a manufacturer-supplied calibration curve. We perform all measurements after evacuation (2.21 mbar). We find that optimal stability and repeatability of the above configuration is achieved >10 h after starting evacuation and switch-

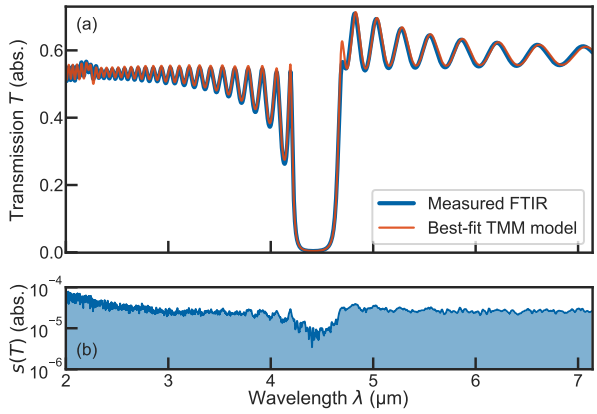

Fig. 3.2. (a) Transmittance spectra of the measured multilayer structure. As-measured in FTIR (blue) and the best-fitted model (orange) obtained when calculating a nonlinear least-squares regression with the TMM model based on the physical layer thicknesses extracted from SEM. (b) Statistical 1s standard uncertainty of the FTIR measurements.

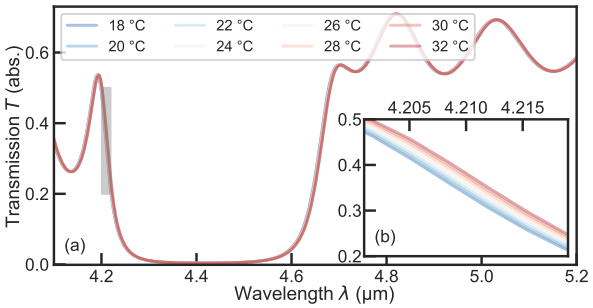

Fig. 3.3. (a) Temperature resolved measurements spanning 18 °C to 32 °C, including the measurement used for retrieving the refractive indices at 22 °C. (b) As systematic shifts are barely visible in the main figure, we show a zoom of the shaded area in (a). The shift of approx. 3 nm at 4210 nm due to changes in temperature is clearly visible.

ing on the light source. Possible causes for this are thermalization (light source, detector) or a gradual improvement in evacuation. It is of note that this is well above the stabilization time recommended by the manufacturer (4 h), which we attribute to the aging of our device. Because of the detector's moderate D^* and the resulting single shot signal-to-noise ratio (SNR), each individual measurement (duration of 15 min each) is the average of 256 individual interferograms.

We record all measurements as double-sided interferograms. That way, the phase spectrum is available at the same resolution as the power spectrum for the FT process, avoiding photometric errors from phase correction of single-sided interferograms [38]. Subsequently, we Fourier transform each measurement to a spectrum with 5 cm^{-1} resolution, using a Norton-Beer medium apodization and Mertz phase correction in the process, previously shown to yield optimal photometric accuracy [39]. To obtain the transmittance spectrum of the DBR, we ratio the sample spectrum against a background spectrum, which is measured and evaluated under identical conditions immediately before. We repeat the background (sample size $i = 14$) and sample ($i = 8$) measurements several times to estimate the associated type A uncertainties for each series over our entire measurement range 1400 cm^{-1} to 5000 cm^{-1} [see Fig. 3.2(b)].

We stabilize the sample temperature at $T_s = 22 \pm 1$ °C using a custom-built optomechanical mount with a single-stage TEC element to exclude fluctuations due to thermal drift. We carefully aligned the sample to normal incidence (overlapping the reflected light with the incident beam at the entrance of the sample chamber), with an estimated error of $<0.3°$.

Temperature-resolved measurements

The aforementioned TEC-stabilized mount allowed us to cool/heat the sample in a limited range (18 °C to 32 °C). The temperature stability is better than ±0.1 K, while the accuracy is limited by the thermistor (including calibration error) to ±1 K. Temperature readings are given in Fig. 3.3. As discussed in [25], such temperature-dependent measurements can be used to extract dn/dT_s and d^2n/dT_s^2, as the linear thermal expansion coefficient of GaAs/Al_xGa_{1-x}As is well known [25]. Accurate extraction of these parameters would require a wider range of temperatures, beyond the capabilities of our custom-built mount.

3.3.3 Scanning electron microscope measurements

We measure the individual thickness of each GaAs/Al_xGa_{1-x}As layer using a scanning electron microscope (Zeiss Supra 55 VP) providing a cross section of the same sample used in FTIR measurements.

The described routine takes direct advantage of the excellent thickness uniformity of epitaxial DBRs, which was demonstrated to be less than 0.41±0.05 nm RMS over a 4-cm-diameter sample in [40]. This allows us to extract individual measurements from several thousand high-resolution line scans to calculate sample statistics, drastically reducing the standard uncertainty.

Sample preparation

Prior to preparing the cross section, we deposit a gold layer on top of the heterostructure using a table-top sputtering device (Leica EM SCD050 with EM QSG100) to avoid contrast issues at the air-GaAs boundary in SEM metrology (see Fig. 3.4). To reveal the cross section of the multilayer, we cleave the die within the c. 2 mm spot probed in FTIR spectrometry using a standard diamond scribe. As we use a monocrystalline superlattice structure this results in a cross section perpendicular to the front surface (flatness was confirmed using a secondary electron detector in SEM). We mount the sample on a 90° sample holder to exclude systematic errors (tilt angle and vibration).

As $Al_xGa_{1-x}As$ is known to form oxide layers, we take care that the sample is exposed to the atmosphere prior to SEM imaging for no more than 15 min. According to prior studies [41], this will cause an oxide layer of c. 1 nm thickness for our sample. We find this to be negligible compared to the mean interaction depth of backscattered electrons, simulated to be $\gg$1 nm at 10 keV (using CASINO v2.51 [42]). Hence, this thin oxide film does not affect SEM imaging using a backscattered electron detector.

Cross-sectional measurement

We load the mounted sample on the SEM's multisample holder together with a certified calibration standard (EM-TEC MCS-0.1CF). After evacuation of the system (c. 5×10^{-5} mbar), we perform all measurements at a beam energy of 10 keV. All images used in this evaluation were obtained at a working distance of c. 9.5 mm. Prior to calibration and measurement, we set a nominal magnification of c. 6600, so that the complete superlattice structure is captured in a single image. We use the standard's 1 µm grid (17 lines with 1 µm pitch, certified total length of 16.0100 ± 0.0048 µm) to calibrate the SEM at the chosen magnification. We image the standard with the above settings after optimizing the stigmator and focus to obtain an undistorted micrograph [see Fig. 3.4(a)]. Following the calibration step, we use the translation stage of the SEM to position the cross-section of our heterostructure below the electron gun. In this step, we also corrected for a slight height difference between the standard and sample by moving the cross-section into focus (at identical working distance etc.). Thereby, the heterostructure is imaged under identical conditions as the standard at four distinct positions.

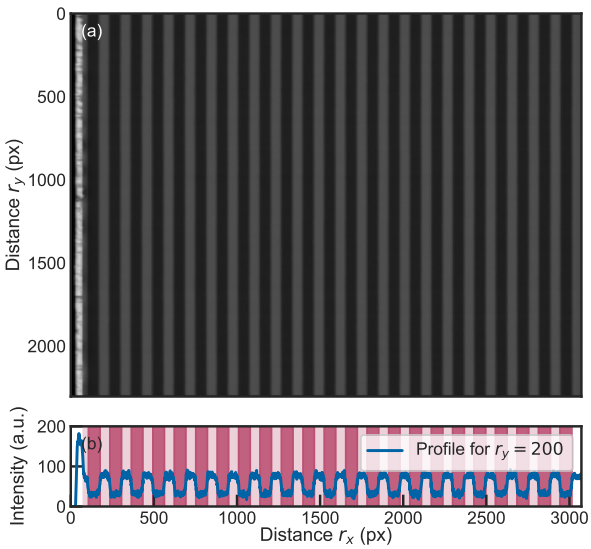

Fig. 3.4. (a) One of a total of four SEM images of the DBR under test. The leftmost layer is gold, coated after FTIR to exclude boundary effects in SEM metrology. The size of this micrograph is c. 17.3 µm × 12.9 µm, resulting from a calibrated pitch of 5.6278 ± 0.0017 nm px^{-1}. (b) The typical profile of a single row (blue) with extracted layer thicknesses (red).

Evaluation

For both the standard and the sample, we use a custom Python 3 script to extract the interface positions according to the following steps:

(i) loading the picture as a 2D array, where every entry is assigned the 8-bit gray-scale value of the corresponding pixel,

(ii) slicing the image row-by-row to get a line profile [see Fig. 3.4(b)],

(iii) estimating the interface positions by finding the extrema of the first derivative of the rowwise profile,

(iv) dividing each single-row profile into smaller intervals around the estimated interface positions so that each interval contains a single interface,

(v) for each interface, fitting an error function and using the inflection point of the fitted curve as our estimate for the interface position (using the error function is justified by the fact that it is the convolution of an electron beam, approximated by a Gaussian profile, and the abrupt material interface, approximated by a step function),

(vi) layer thicknesses are obtained by subtracting subsequent estimates for the interface positions from each other, and

(vii) repeating the above procedure for all rows in

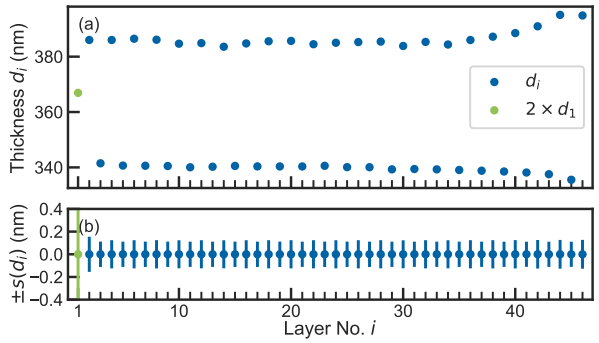

Fig. 3.5. (a) Measured layer thicknesses, resulting from averaging row-wise measurements. Note that the thickness of the 1/8-wave cap d_1 (green) was multiplied by a factor of 2. (b) Error bars showing 1s standard uncertainty for the mean values given in (a).

Table 3.1. Parameters to calculate the refractive indices for both materials according to our results for models given by Eq. (3.1) and Eq. (3.3).

Material	Model	Variable	Value
GaAs	Eq. (3.2)	x	0
	Eq. (3.1)	η	0.170481
		E_f	4.36144
	Eq. (3.3)	E_0	3.21318
		E_d	31.1845
$Al_{0.929}Ga_{0.071}As$	Eq. (3.2)	x	0.929
	Eq. (3.1)	η	0.0393107
		E_f	5.90697
	Eq. (3.3)	E_0	4.64100
		E_d	33.4811

the image, we find the mean and 1s standard uncertainty of the mean for each layer $s(d_i)$.

In the case of the sample, we repeat these steps for all four images. In this procedure, we exclude significant systematic errors due to sample tilt by testing for systematic changes in extracted interface positions.

From the evaluation of the reference standard, we establish a calibrated distance per imaged pixel. For that, we measure the certified distance of the standard to be 2844.807 ± 0.010 px. This results in a calibrated pitch of $5.6278 \pm 0.0017\,\mathrm{nm\,px^{-1}}$. The propagated uncertainty of 0.03% is dominated by the certified uncertainty of the standard, as the relative statistical uncertainty is <4 ppm.

From four SEM images of the GaAs/Al_xGa_{1-x}As heterostructure, we extract the mean and standard uncertainty of the individual layer thicknesses in units of pixels. We multiply these values by the calibrated pitch to assign physical layer thicknesses in units of nanometers, as summarized in Fig. 3.5.

The propagated relative uncertainty ($<4 \times 10^{-4}$ for all $\lambda_\mathrm{d}/4$ layers) is dominated by the uncertainty of the calibration standard, except for the topmost $\lambda_\mathrm{d}/8$ GaAs layer, which exhibits a relative uncertainty of 2.2×10^{-3}. This is caused by the Au/GaAs interface, where the data quality suffers from remaining structures in the Au cross section that could not be eliminated.

3.4 Results

To obtain the refractive indices of GaAs/Al_xGa_{1-x}As from the above measurements, we use a nonlinear least-squares fitting approach. In that process, we seed a TMM model based on the layer thicknesses obtained via SEM and model the refractive indices according to the models in Eqs. (3.1) and (3.3). We then fit the resulting curve to the photometrically-accurate FTIR transmittance T spectrum [see Fig. 3.2(a)] to obtain values for the free parameters, effectively resulting in values for the refractive indices of GaAs/Al_xGa_{1-x}As.

To infer accurate mean values and standard uncertainties for both refractive indices, we use the described Monte Carlo-type uncertainty propagation. This involves running the fit routine 1000 times for each model. Before each fit, we randomly pick the transmittance values $T(\lambda)$, the individual layer thicknesses d_i, and, in the case of Eq. (3.1), the AlAs content x and literature values for E_Γ, from normal distributions representing their respective propagated uncertainty. The resulting distributions, which give the mean and standard uncertainty for n, also closely follow a normal distribution. Subsequently, we use each set of Monte Carlo parameters to calculate the refractive index, where the variation of these calculations results in mean values and standard uncertainties for both indices $n(\lambda)$, which we show in Fig. 3.6. We report model parameters reproducing our results in Table 3.1 for ease of computation. The largest relative standard uncertainty is observed at the lower-wavelength end of our spectrum. Using Eq. (3.1) with Eq. (3.2), these values are $s(n_\mathrm{GaAs})/n_\mathrm{GaAs} \leq 3.2 \times 10^{-4}$ and $s(n_\mathrm{AlGaAs})/n_\mathrm{AlGaAs} \leq 2.8 \times 10^{-4}$, whereas uncertainties for Eq. (3.3) are $\leq 3.3 \times 10^{-4}$ and $\leq 2.9 \times 10^{-4}$ for GaAs and $Al_{0.929}Ga_{0.071}As$, respectively. We report these as the uncertainty for n when calculated with parameters in Table 3.1 over the whole wavelength range.

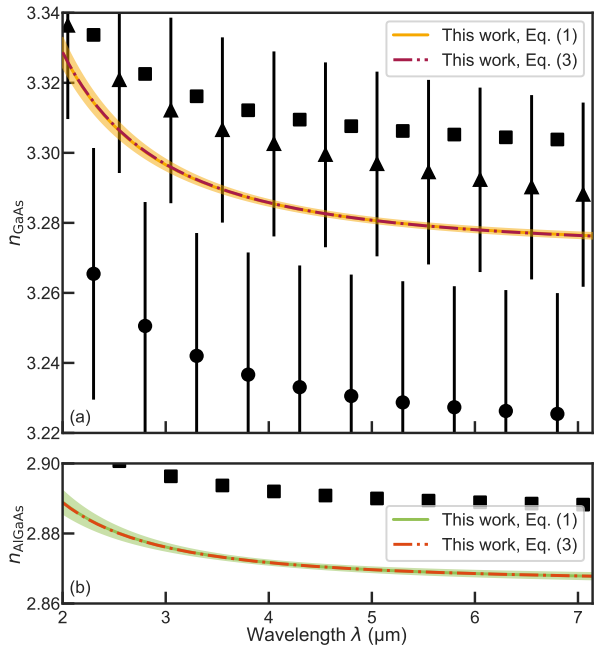

Fig. 3.6. Final results for the refractive indices, compared to values from literature. Error bands/bars for our results obtained from fitting Eq. (3.1) and for values from Ref. [25] (triangles, Pikhtin model) are given as fourfold standard uncertainty $4s(n)$, while the error bars for Ref. [26] (circles) are given as $1s(n)$. Values for Ref. [23] (squares) represent an extrapolation from the NIR with unknown uncertainty. Error bands for our fit of Eq. (3.3) are omitted because they are almost identical to those for Eq. (3.1). (a) Refractive index of GaAs. (b) Refractive index of $Al_{0.929}Ga_{0.071}As$.

3.5 Conclusions and outlook

In summary, we report the simultaneous measurement of refractive index n values for both pure GaAs and $Al_{0.929}Ga_{0.071}As$ in the spectral range 2–7.1 µm at room temperature ($T_s = 22 \pm 1\,°C$), probing a superlattice DBR, grown via MBE with exceptionally low background doping [18].

We obtain these measurements via a general, highly-adaptable method, that allows us to measure the refractive indices of two materials simultaneously by probing a thin-film heterostructure. The approach can be used with crystalline and amorphous dielectric multilayers. These multilayers bear the advantage that one of the materials is not exposed to the atmosphere, easing the characterization of oxidizing materials such as $Al_xGa_{1-x}As$, avoiding complicated schemes [27, 41].

This enables routine refractive index measurements of current and future optical materials in their transparent range. As outlined in Fig. 3.1, the individual steps involve acquiring the optical response and accurately measuring the layer thicknesses. In our process, we accurately measure the thickness of each layer. Consequently, the sample does not have to be a DBR, provided that the transmittance spectrum has broadband characteristics, which remain undistorted by the resolution of the spectrometer in use. Many multilayer structures, such as antireflection (AR) or broadband high-reflectivity (BBHR) coatings, typically meet this criterion. A subsequent nonlinear least-squares fit results in accurate refractive index values over a broad wavelength range, capturing material dispersion with suitable empirical, semiempirical, or theoretical models for both refractive indices. Compared to other approaches, the presented routine realizes high levels of accuracy and precision, while reducing experimental complexity and relying on widely-available devices. We do not require specialized and cost-intensive optical setups, such as spectroscopic ellipsometers [43]. The evaluation step avoids intricate extrapolation routines, which are needed in the fringe pattern analysis used for FTIR refractometry [22, 25].

In the present study, we acquire a photometrically-accurate transmittance spectrum via FTIR spectrometry and an accurate measurement of individual layer thicknesses via calibrated SEM metrology. For both measurements, control of systematic errors was necessary but achieved by simple means such as careful alignment and temperature stabilization. Subsequently, we perform a nonlinear least-squares fitting routine based on TMM, where the dispersion $dn/d\lambda$ was captured according to two different models for each refractive index. Finally, we use the best-fit results to obtain the refractive indices for GaAs/$Al_{0.929}Ga_{0.071}As$ over the entire wavelength range. Propagation of measurement uncertainties via a Monte Carlo approach suggests relative uncertainties on the order of 10^{-4} for both materials, achieving good agreement with previously-published results. Differences to the values published in [23] are explained by the fact that this data represents an extrapolation from a fit to NIR measurements. Notably, the data by Palmer *et al.* [26] shows the largest discrepancy, likely caused by a systematic offset due to the incorrect assumption of perfectly uniform high- and low-index layers. The discrepancy with regards to the results by Skauli *et al.* [25], which were used to model the GaAs wafer in the present study, is likely caused by different material properties, such as free-carrier concentrations [21] when comparing MBE-grown GaAs with LEC/VGF-grown GaAs wafers.

We believe that both the proposed method and the updated values for GaAs/$Al_{0.929}Ga_{0.071}As$ should find use in the design, fabrication, and characterization of active and passive optical devices. This is of special importance for the MIR, which is of high interest for applications in spectroscopy, but also a region where the optical properties of many materials are still poorly studied.

Acknowledgments

We thank Dr. Stefan Eichler at Freiberger Compound Materials GmbH for GaAs wafer characterization data, Prof. Thomas Pichler for access to his group's FTIR device, Dr. Valentina Shumakova for her help with Fig. 3.1, and Dr. Adam J. Fleisher at NIST Gaithersburg for in-depth discussions and helpful advice.

We acknowledge support from the Faculty Center for Nano Structure Research at the University of Vienna, providing the SEM. The financial support by the Austrian Federal Ministry for Digital and Economic Affairs, the National Foundation for Research, Technology and Development and the Christian Doppler Research Association is gratefully acknowledged.

References

[1] C. W. Wilmsen, H. Temkin, and L. A. Coldren, eds., *Vertical cavity surface emitting lasers: design, fabrication, characterization, and applications*, 1st ed., Cambridge Studies in Modern Optics (Cambridge University Press, Cambridge, 2001).

[2] C.-F. Lin and B.-L. Lee, "Extremely broadband AlGaAs/GaAs superluminescent diodes", Appl. Phys. Lett. **71**, 1598 (1997).

[3] C. Sirtori, P. Kruck, S. Barbieri, P. Collot, J. Nagle, M. Beck, J. Faist, and U. Oesterle, "GaAs/$Al_xGa_{1-x}As$ quantum cascade lasers", Appl. Phys. Lett. **73**, 3486 (1998).

[4] D. Hofstetter, F. R. Giorgetta, E. Baumann, Q. Yang, C. Manz, and K. Köhler, "Mid-infrared quantum cascade detectors for applications in spectroscopy and pyrometry", Appl. Phys. B **100**, 313 (2010).

[5] S. Gunapala, S. Bandara, J. Liu, C. Hill, S. Rafol, J. Mumolo, J. Trinh, M. Tidrow, and P. LeVan, "Development of mid-wavelength and long-wavelength megapixel portable QWIP imaging cameras", Infrared Phys. Techn. **47**, 67 (2005).

[6] J. P. van der Ziel and M. Ilegems, "Multilayer GaAs-$Al_{0.3}Ga_{0.7}As$ dielectric quarter wave stacks grown by molecular beam epitaxy", Appl. Opt. **14**, 2627 (1975).

[7] J. P. van der Ziel and M. Ilegems, "Interference filters: single crystal multilayer AlAs–GaAs", Appl. Opt. **15**, 1256 (1976).

[8] W. Heiss, T. Schwarzl, J. Roither, G. Springholz, M. Aigle, H. Pascher, K. Biermann, and K. Reimann, "Epitaxial Bragg mirrors for the mid-infrared and their applications", Prog. Quantum Electron. **25**, 193 (2001).

[9] U. Keller, K. J. Weingarten, F. X. Kärtner, D. Kopf, B. Braun, I. D. Jung, R. Fluck, C. Hönninger, N. Matuschek, and J. Aus der Au, "Semiconductor saturable absorber mirrors (SESAM's) for femtosecond to nanosecond pulse generation in solid-state lasers", IEEE J. Sel. Top. Quantum Electron. **2**, 435 (1996).

[10] U. Keller, "Ultrafast solid-state laser oscillators: A success story for the last 20 years with no end in sight", Appl. Phys. B **100**, 15 (2010).

[11] G. D. Cole, S. Gröblacher, K. Gugler, S. Gigan, and M. Aspelmeyer, "Monocrystalline $Al_xGa_{1-x}As$ heterostructures for high-reflectivity high-Q micromechanical resonators in the megahertz regime", Appl. Phys. Lett. **92**, 261108 (2008).

[12] U. W. Pohl, *Epitaxy of Semiconductors: Physics and Fabrication of Heterostructures*, 2nd ed., Graduate Texts in Physics (Springer International Publishing, Cham, 2020).

[13] B. Barr, A. Bell, C. Bell, C. Bond, D. Brown, F. Brueckner, L. Carbone, K. Craig, A. Cumming, S. Danilishin, et al., *LIGO 3 Strawman Design, Team Red (T1200046-v1)* (LIGO, 2012).

[14] G. D. Cole, S. W. Ballmer, G. Billingsley, S. B. Cataño-Lopez, M. Fejer, P. Fritschel, A. M. Gretarsson, G. M. Harry, D. Kedar, T. Legero, et al., "Substrate-transferred GaAs/AlGaAs crystalline coatings for gravitational-wave detectors", Appl. Phys. Lett. **122**, 110502 (2023).

[15] G. D. Cole, W. Zhang, M. J. Martin, J. Ye, and M. Aspelmeyer, "Tenfold reduction of Brownian noise in high-reflectivity optical coatings", Nat. Photonics **7**, 644 (2013).

[16] G. D. Cole, W. Zhang, B. J. Bjork, D. Follman, P. Heu, C. Deutsch, L. Sonderhouse, J. Robinson, C. Franz, A. Alexandrovski, et al., "High-performance near- and mid-infrared crystalline coatings", Optica **3**, 647 (2016).

[17] G. Winkler, L. W. Perner, G.-W. Truong, G. Zhao, D. Bachmann, A. S. Mayer, J. Fellinger, D. Follman, P. Heu, C. Deutsch, et al., "Mid-infrared interference coatings with excess optical loss below 10 ppm", Optica **8**, 686 (2021).

[18] G.-W. Truong, L. W. Perner, G. Winkler, S. B. Cataño-Lopez, C. Nguyen, D. Follman, O. H. Heckl, and G. D. Cole, *Transmission-dominated mid-infrared supermirrors with finesse exceeding 200 000*, (2022) arXiv:2209.09902v2, preprint.

[19] G. Gagliardi and H.-P. Loock, eds., *Cavity-Enhanced Spectroscopy and Sensing*, Vol. 179, Springer Series in Optical Sciences (Springer, Berlin, Heidelberg, 2014).

[20] B. J. Bjork, T. Q. Bui, O. H. Heckl, P. B. Changala, B. Spaun, P. Heu, D. Follman, C. Deutsch, G. D. Cole, M. Aspelmeyer, et al., "Direct frequency comb measurement of OD + CO → DOCO kinetics", Science **354**, 444 (2016).

[21] D. D. Sell, H. C. Casey, and K. W. Wecht, "Concentration dependence of the refractive index for *n*- and *p*-type GaAs between 1.2 and 1.8 eV", J. Appl. Phys. **45**, 2650 (1974).

[22] S. G. Kaplan, L. M. Hanssen, U. Griesmann, and R. Gupta, "Fourier transform refractometry", in Optical Diagnostic Methods for Inorganic Transmissive Materials, Vol. 3425, edited by R. V. Datla and L. M. Hanssen, Proceedings of SPIE (1998), pp. 203–212.

[23] M. A. Afromowitz, "Refractive index of $Ga_{1-x}Al_xAs$", Solid State Commun. **15**, 59 (1974).

[24] H. C. Casey, D. D. Sell, and M. B. Panish, "Refractive index of $Al_xGa_{1-x}As$ between 1.2 and 1.8 eV", Appl. Phys. Lett. **24**, 63 (1974).

[25] T. Skauli, P. S. Kuo, K. L. Vodopyanov, T. J. Pinguet, O. Levi, L. A. Eyres, J. S. Harris, M. M. Fejer, B. Gerard, L. Becouarn, et al., "Improved dispersion relations for GaAs and applications to nonlinear optics", J. Appl. Phys. **94**, 6447 (2003).

[26] C. Palmer, P. N. Stavrinou, M. Whitehead, and C. C. Phillips, "Mid-infrared (λ~2–6 μm) measurements of the refractive indices of GaAs and AlAs", Semicond. Sci. Technol. **17**, 1189 (2002).

[27] K. Papatryfonos, T. Angelova, A. Brimont, B. Reid, S. Guldin, P. R. Smith, M. Tang, K. Li, A. J. Seeds, H. Liu, et al., "Refractive indices of MBE-grown $Al_xGa_{(1-x)}As$ ternary alloys in the transparent wavelength region", AIP Adv. **11**, 025327 (2021).

[28] M. Born and E. Wolf, *Principles of Optics*, 7th ed., 60th anniversary edition (Cambridge University Press, Cambridge, 2019).

[29] S. J. Byrnes, *Multilayer optical calculations*, (2020) arXiv:1603.02720v5, preprint.

[30] A. Luce, A. Mahdavi, F. Marquardt, and H. Wankerl, "TMM-Fast, a transfer matrix computation package for multilayer thin-film optimization: tutorial", J. Opt. Soc. Am. A **39**, 1007 (2022).

[31] W. von Sellmeier, "Zur Erklärung der abnormen Farbenfolge im Spectrum einiger Substanzen", Ann. Phys. Chem. **219**, 272 (1871).

[32] H. C. Casey and M. B. Panish, *Heterostructure Lasers: Part A, Fundamental Principles*, red. by Y.-H. Pao and P. Kelley, Quantum Electronics — Principles and Applications (Academic Press, New York, 1978).

[33] S. H. Wemple and M. DiDomenico, "Behavior of the Electronic Dielectric Constant in Covalent and Ionic Materials", Phys. Rev. B **3**, 1338 (1971).

[34] K. Bertness, J. Armstrong, R. Marinenko, L. Robins, A. Paul, J. Pellegrino, P. Amirtharaj, and D. Chandler-Horowitz, "AlGaAs composition measurements from in situ optical reflectance", in 2000 Digest of the LEOS Summer Topical Meetings. Electronic-Enhanced Optics. Optical Sensing in Semiconductor Manufacturing. Electro-Optics in Space. Broadband Optical Networks (Cat. No.00TH8497) (2000), pp. II21–II22.

[35] K. A. Bertness, T. E. Harvey, C.-M. Wang, A. J. Paul, and L. H. Robins, *Standard Reference Materials 2840 to 2482 Composition standards for AlGaAs epitaxial layers*, NIST SP 260-163 (NIST, Gaithersburg, MD, United States, 2006), NIST SP 260–163.

[36] E. Theocharous and J. Birch, "Detectors for Mid- and Far-Infrared Spectrometry: Selection and Use", in *Handbook of Vibrational Spectroscopy*, Vol. 1, edited by J. M. Chalmers and P. R. Griffiths, 1st ed. (Wiley, Chichester, UK, 2002).

[37] E. Theocharous, "Absolute linearity measurements on a gold-black-coated deuterated L-alanine-doped triglycine sulfate pyroelectric detector", Appl. Opt. **47**, 3731 (2008).

[38] D. B. Chase, "Phase Correction in FT-IR", Appl. Spectrosc. **36**, 240 (1982).

[39] P. R. Griffiths and J. A. De Haseth, *Fourier Transform Infrared Spectrometry*, 2nd ed., Chemical Analysis 83 (Wiley, Hoboken, NJ, USA, 2007).

[40] P. Koch, G. D. Cole, C. Deutsch, D. Follman, P. Heu, M. Kinley-Hanlon, R. Kirchhoff, S. Leavey, J. Lehmann, P. Oppermann, et al., "Thickness uniformity measurements and damage threshold tests of large-area GaAs/AlGaAs crystalline

coatings for precision interferometry", Opt. Express **27**, 36731 (2019).

[41] F. Reinhardt, B. Dwir, and E. Kapon, "Oxidation of GaAs/AlGaAs heterostructures studied by atomic force microscopy in air", Appl. Phys. Lett. **68**, 3168 (1996).

[42] D. Drouin, A. R. Couture, D. Joly, X. Tastet, V. Aimez, and R. Gauvin, "CASINO V2.42—A Fast and Easy-to-use Modeling Tool for Scanning Electron Microscopy and Microanalysis Users", Scanning **29**, 92 (2007).

[43] H. Fujiwara, *Spectroscopic Ellipsometry: Principles and Applications*, 1st ed. (Wiley, Chichester, UK, 2007).

4 Mid-infrared supermirrors with finesse exceeding 400 000

G.-W. Truong[1,a], **L. W. Perner**[2,3,a], D. M. Bailey[4], G. Winkler[2], S. B. Cataño-Lopez[1], V. J. Wittwer[5], T. Südmeyer[5], C. Nguyen[1], D. Follman[1], A. J. Fleisher[4], O. H. Heckl[2], G. D. Cole[1]

[1]Thorlabs Crystalline Solutions, 114 E Haley St., Suite G, Santa Barbara, California 93101, USA

[2]Christian Doppler Laboratory for Mid-IR Spectroscopy and Semiconductor Optics, Faculty Center for Nano Structure Research, Faculty of Physics, University of Vienna, Boltzmanngasse 5, 1090 Vienna, Austria

[3]Vienna Doctoral School in Physics, University of Vienna, Boltzmanngasse 5, 1090 Vienna, Austria

[4]National Institute of Standards and Technology, 100 Bureau Drive, Gaithersburg, Maryland 20899, USA

[5]Laboratoire Temps-Fréquence, Institut de Physique, Université de Neuchâtel, Avenue de Bellevaux 51, 2000 Neuchâtel, Switzerland

[a]These authors contributed equally to this work.

Everything transitory—the knower and the known.

(Marcus Aurelius, Meditations 4.35)

Bibliographical information

The contents of this chapter correspond to the current version of a manuscript resubmitted to *Nature Communications* after peer-review including a supplementary document (see Section 4.6). This revised and extended version was received by the journal on 11 September 2023 and sent to the referees on 12 September 2023 for confirmation.

Minor typographical errors were silently corrected and the formatting has been carefully adapted for the purpose of this thesis, while the results remain unchanged. The original title and authors correspond to the chapter title and authors. Author affiliations are given as they appear in the original manuscript.

An earlier version of this manuscript (received by the journal on 21 July 2023 and sent for peer-review on 24 July 2024) is available on the arXiv as

> G.-W. Truong et al., *Mid-infrared supermirrors with finesse exceeding 400 000,* (2023) arXiv:2209.09902v3, preprint.

The initial version of this manuscript was submitted to *Nature Communications* on 21 October 2022. This version is also available on the arXiv as

> G.-W. Truong et al., *Transmission-dominated mid-infrared supermirrors with finesse exceeding 200 000,* (2022) arXiv:2209.09902v2, preprint.

Author contributions

For the here-presented results, I am a co-inventor of a patent for the hybrid coating paradigm, combining an amorphous multilayer structure with a crystalline heterostructure. Together with Gar-Wing Truong and Seth Cataño-Lopez, I co-developed the cavity ringdown reflectometer in Santa Barbara, CA, during a visit at Thorlabs Crystalline Solutions. This included custom-built diagnostics (hardware and software for an Fourier-transform spectrometer to monitor the laser spectrum, software for the monochromator-based solution to obtain spectrally resolved ringdown curves) and the ringdown cavity itself. Furthermore, I lead the efforts to characterize the transmittance of the all-crystalline mirrors, measuring transmittance spectra of completed mirrors via precision Fourier-transform spectrometry in Vienna. I also was in charge of the subsequent data analysis to obtain accurate transmittance values, partly based on results obtained in Chapter 3. Together with Valentin Wittwer, co-inventor of the hybrid mirrors, I co-characterized the amorphous heterostructures used in the hybrid mirrors, using both complete stacks and single-layer samples and various techniques (spectroscopic ellipsometry, Fourier-transform spectrometry, and spectrophotometry). We collaborated intensely on the experimental part during a research visit in Switzerland. We co-lead the ensuing data analysis with support from Gar-Wing Truong. Gar-Wing and I organized the writing of the manuscript, writing substantial parts and incorporating the various contributions of the other co-authors.

Abstract

For trace gas sensing and precision spectroscopy, optical cavities incorporating low-loss mirrors are indispensable for path length and optical intensity enhancement. Optical interference coatings in the visible and near-infrared (NIR) spectral regions have achieved total optical losses below 2 parts per million (ppm), enabling a cavity finesse in excess of 1 million. However, such advancements have been lacking in the mid-infrared (MIR), despite substantial scientific interest. Here, we demonstrate a significant breakthrough in high-performance MIR mirrors, reporting substrate-transferred single-crystal interference coatings capable of cavity finesse values from 200 000 to 400 000 near 4.5 μm, with excess optical losses (scatter and absorption) below 5 ppm. In a first proof-of-concept demonstration, we achieve the lowest noise-equivalent absorption in a linear cavity ring-down spectrometer normalized by cavity length. This substantial improvement in performance will unlock a rich variety of MIR applications for atmospheric transport and environmental sciences, detection of fugitive emissions, process gas monitoring, breath-gas analysis, and verification of biogenic fuels and plastics.

4.1 Introduction

High-performance resonators integrating low-optical-loss mirrors are used in a wide variety of applications, ranging from time-and-frequency metrology, quantum electrodynamics and optomechanics, to trace gas sensing and detection. Rempe *et al.* [1] reported an ion-beam sputtered (IBS) coating at 850 nm on conventionally-polished substrates with transmittance $T = 0.5$ ppm and excess loss (consisting of scatter, S, and absorption, A) of $S + A = 1.1$ ppm. More recently, IBS coatings on micro-fabricated mirrors have shown even lower excess losses of $S + A = 0.74$ ppm (with $T = 1.9$ ppm) at 1550 nm [2, 3]. In the MIR, only modest coating advancements have been realized and this technology significantly lags what is readily achievable in the NIR. The lowest reported excess loss for traditional amorphous MIR mirrors is $S + A = 30$ ppm with $T = 120$ ppm at 4.53 µm, resulting in a cavity finesse of $\mathcal{F} = \pi\sqrt{R}/(1-R) = 20\,900$ [4], where $R = 1 - T - S - A$ is the reflectivity. Similar mirrors with reduced transmission values have yielded increased finesse values from 52 000 to 67 700 [5–7], though the component losses (T vs. $S + A$) in these systems are unknown. In contrast, substrate-transferred monocrystalline GaAs/AlGaAs Bragg mirrors at 4.54 µm, have shown the lowest levels of excess loss to date ($S + A = 7$ ppm) [8]. In that work, the transmission was high compared to the mirror losses, with $T = 144$ ppm, leading to a cavity finesse of 20 800, but with much greater on-resonance cavity transmission of $(T/(T + S + A))^2 = 91\%$ compared with 64% for previous results [4].

Here, we report on the realization of ultrahigh-finesse MIR mirrors using two coatings methods. The first method extends the recently-reported "all-crystalline" architecture [8] [Fig. 4.1(a)] to produce a transmission-loss-dominated cavity finesse of 231 000 at 4.5 µm (on-resonance transmission >48%). A second "hybrid" approach yields even higher finesse, exceeding 400 000 (on-resonance transmission of 11%). This new hybrid coating paradigm [Fig. 4.1(b)] combines two different coating processes – an amorphous sub-stack deposition is followed bonding a crystalline multilayer on top. Owing to the minimal field penetration depth in quarter-wave reflective interference coatings (Fig. 4.2), these mirrors exhibit excess losses at least a factor of six lower than the previous best results obtained with all-amorphous interference coatings. This represents simultaneously the highest finesse and lowest excess losses yet achieved in this spectral region. The finesse and cavity transmission improvements enabled by these mirrors lead to compounding advantages for spectroscopy, resulting in record-low levels of noise-equivalent absorption. As a proof-of-concept demonstration, we present trace gas detection in ultra-high purity nitrogen.

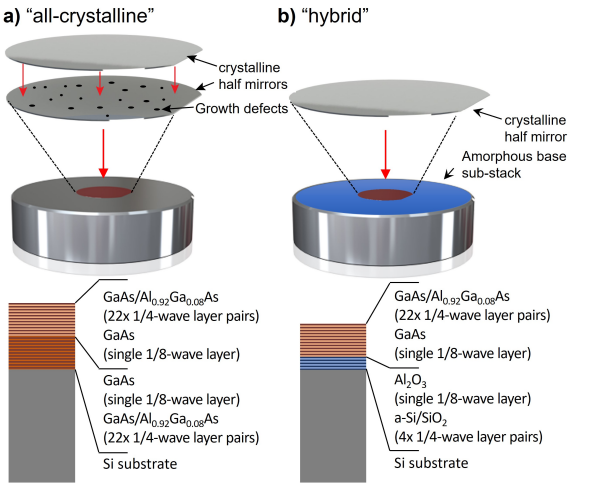

Fig. 4.1. Schematic description of the manufacturing process and coating structure for the (a) all-crystalline and (b) hybrid designs. These ultralow-loss mirrors leverage the low scatter and absorption losses of substrate-transferred MBE-grown GaAs/AlGaAs multilayers.

4.2 Design, fabrication, and optical validation

Figure 4.1 schematically shows the two low-loss mirror designs investigated in this manuscript. The double-bonded all-crystalline structure consists of alternating high refractive index GaAs and low refractive index $Al_{0.92}Ga_{0.08}As$ layers. We additionally pursue the development of a novel hybrid mirror design that combines the same GaAs/AlGaAs multilayer with an IBS-deposited amorphous sub-stack. All mirrors use super-polished single-crystal Si substrates with a concave radius of curvature of 1 m, with the backside wedged at 0.5° and IBS-coated with a broadband 4–5 µm anti-reflection coating.

As described above, both mirror designs use a common crystalline "half-stack" multilayer grown via molecular beam epitaxy (MBE), comprising 22.25 periods of $GaAs/Al_{0.92}Ga_{0.08}As$ ($22 \times 1/4$-wave layer pairs, in terms of optical thickness, terminating with a 1/8-wave layer of high index GaAs). The epitaxial half-

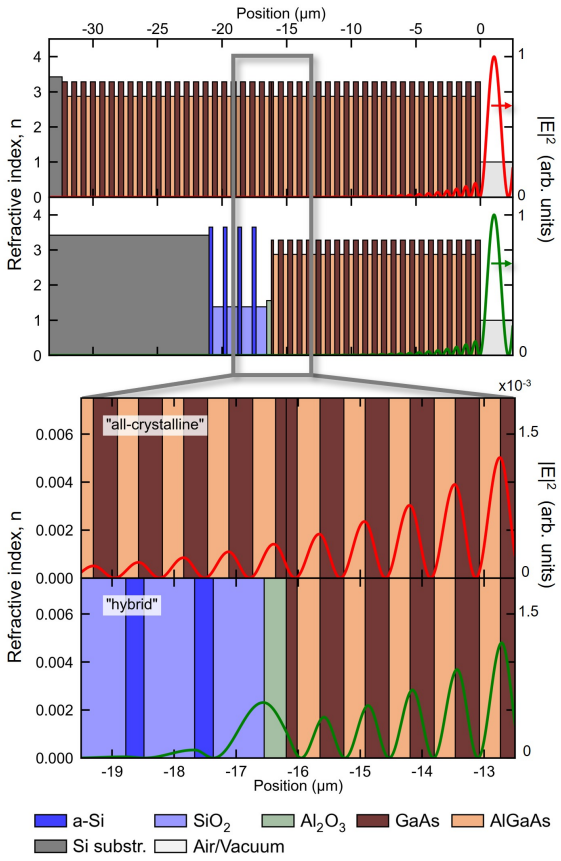

Fig. 4.2. Simulated decay of the electric fields (red and green traces) as a function of depth into the all-crystalline and hybrid coatings. The multilayer designs and material indices at 4.45 µm are provided. Replacement of one crystalline half-mirror with an amorphous stack has little impact on optical absorption if the crystalline layers remain the first reflection surfaces. Comparing the electric fields, the optical field penetration depth of 878 nm is identical for both the all-crystalline and hybrid coatings (for details see main text).

stack reduces the total physical thickness of the as-grown multilayer, minimizing the defect density and ultimately the optical losses of the crystalline coating. Deposition is carried out on a lattice-matched 15 cm diameter [001]-oriented semi-insulating GaAs wafer. Following the crystal growth process, individual crystalline mirror die are defined via lithography and etching.

For the all-crystalline mirrors, two crystalline half-stack die are directly bonded to realize the full mirror stack, now 44.5 periods of $GaAs/Al_{0.92}Ga_{0.08}As$ with a nominal T of 10 ppm at a target center wavelength of 4.5 µm. Next, the stacked epitaxial multilayer is transferred to the Si optical substrate, again using direct bonding with no adhesives or interlayers [9, 10].

In the case of the hybrid mirrors, the base Si substrates are initially coated with an amorphous partial mirror structure via IBS. Amorphous Si (a-Si) is used for the high refractive index layers, with silica (SiO_2) as the low index component, with four periods of a-Si/SiO_2 deposited before a 1/8-wave terminating alumina (Al_2O_3) layer. This termination layer was intended to aid bonding, but subsequent designs ending the amorphous stack with a-Si were found to behave identically. An annealing process at 300 °C for 24 hours minimizes internal stresses and reduces the optical absorption of the IBS films. Following the IBS deposition and annealing processes, we directly bond a GaAs/AlGaAs half mirror die to the capping Al_2O_3 layer to complete the hybrid mirror stack.

We explore both mirror designs to present the trade-offs between the all-crystalline mirrors (offering the lowest possible absorption loss) and the advantages of the hybrid approach (scalable manufacturing and access to longer center wavelengths). Given the optical field penetration depth of 878 nm for both the all-crystalline and hybrid coatings [11] compared to a total coating thickness of 32 µm and 21 µm for the respective designs, it is clear that the optical mode primarily samples the losses from the surface crystalline layers. A small amount of additional absorption of less than 5 ppm, conservatively estimated from worst-case material parameters, is expected from the more lossy amorphous stack due to the slightly enhanced field in the first couple of amorphous layers (Al_2O_3 and SiO_2) near the crystal-amorphous interface (Fig. 4.2). The hybrid coating approach also offers a wider stop-band (due to the higher refractive index contrast of the amorphous layers), and the ability to extend the achievable center wavelengths, nominally to 12 µm and beyond.

In the hybrid mirror design, the epitaxial stack can be limited to a maximum physical thickness that maintains high structural perfection with limited growth-induced defects. A thinner crystalline multilayer (exhibiting minimal defects) enables ppm-level losses at wavelengths longer than that which can be achieved with the all-crystalline structure by avoiding excessively thick epilayers or successive bonding steps to push to wavelengths beyond 5 µm. Additional details of the manufacturing process and limitations are discussed in the Methods section.

High precision optical characterization of the completed mirrors to decompose the total loss into transmission and excess losses is possible with the all-crystalline coating since sample preparation required only cleaving of the epi structure. We followed the

prescription given in [12]: i) X-ray diffraction (XRD) of the as-grown crystalline multilayer to determine the Al composition of the ternary $Al_xGa_{1-x}As$ layers; ii) cross-sectional scanning-electron microscopy (SEM) to probe the individual layer thicknesses for all materials; iii) Fourier-transform spectrometry (FTS) for the broadband transmittance spectra of the completed mirrors; iv) transmission matrix modeling (TMM) using the known refractive indices [12], layer thicknesses, and broadband transmittance spectra to determine the transmittance within the stopband, where FTS provides insufficient dynamic range; v) finally, cavity ring-down gives the total loss, from which the transmittance can be subtracted to determine $S + A$. The uncertainty of T at the stopband center (T_0) is estimated with a Monte-Carlo-style model, varying the measured TMM input parameters within their respective error bounds. Using the approach outlined above, calculations are performed for the all-crystalline mirror stack and the individual mirror transmission is found to be $T_0 = 9.33 \pm 0.17$ ppm at 4449.5 ± 0.5 nm. A similar procedure was followed to derive the transmission of the hybrid coating by separately sectioning the amorphous sub-stack. We find $T_0 = 2.53$ ppm at 4450 nm, with the evaluation of uncertainties left to a future study due to the increased difficulty in sample preparation of the insulating materials, as well as the appreciably higher complexity of the modeling for a 6-material system, rather than a 3-material system for the all-crystalline mirrors. Further information is provided in the Methods section.

The total loss measurements were performed using a cavity ring-down reflectometer implemented in a scheme based on that described in [8] with added spectral and spatial scanning capabilities [13]. A broadband Fabry-Perot quantum cascade laser (FP-QCL) was mode matched to the cavity under test with the mirrors separated by 145 ± 2 mm (calculated spot size of 629 µm on each mirror). Optical feedback from a grating in the Littrow configuration tunes the QCL, while a 35-dB optical isolator reduced unwanted optical feedback from the cavity that would dominate the laser behavior. The power transmitted through the resonant cavity was filtered via a monochromator with a passband of 18 nm to provide spectrally resolved ring-down curves (admitting a weighted combination of up to ~260 longitudinal TEM_{00} modes). During testing, the mirrors are held under vacuum (<1 mPa) to avoid intracavity atmospheric absorption.

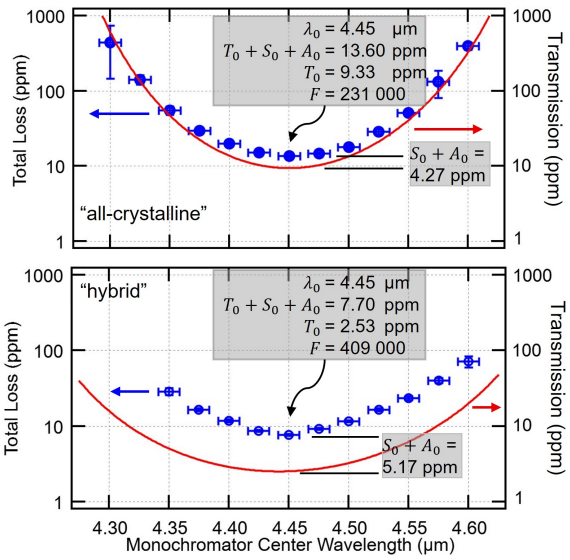

Fig. 4.3. Spectrally resolved measurements of optical losses. Vertical error bars represent the standard deviation of the ensemble of ring-downs taken at a particular wavelength, whereas the horizontal error bars indicate the monochromator bandwidth of ±9 nm. Wavelengths at extremes of the laser tuning range resulted in lower source power and larger uncertainty in loss. Both mirror designs yield record optical performance, with the all-crystalline mirrors achieving a transmission-dominated finesse >200 000, while the hybrid mirrors exceed 400 000 owing to a reduced transmission. Blue circles: measured total loss. Solid red: as-grown transmission (T_{calc}).

Figure 4.3 shows the measured total loss near the region of minimum transmission for pairs of the all-crystalline and hybrid mirrors. For each data point, the center wavelength of the monochromator was set to the desired value and the Littrow grating angle was optimized for maximum optical transmission through the cavity and monochromator. Fewer valid ring-downs were obtainable towards the extremes of the laser tuning range, and the uncertainties increased due to lower signal-to-noise. Due to the free-running nature of the laser, we do not have an estimate of the statistical uncertainty of the laser wavelength.

The lowest total losses of 13.60 ± 0.49 ppm were observed with the monochromator set to 4.45 µm for the all-crystalline mirrors, corresponding to a finesse of $231\,000 \pm 8400$. These prototype mirrors typically showed a region of ~2 mm diameter over which these extreme levels of performance are maintained (see Fig. 4.4). Subtracting T_0, as determined by the TMM fit and XRD characterization of the stack, we infer an excess loss of 4.27 ± 0.52 ppm. If we assume scatter to be negligible and assign all excess losses in the GaAs/AlGaAs multilayer to absorption, this corresponds to an absorption coefficient, α_{coat}, of

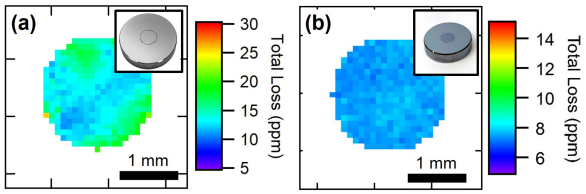

Fig. 4.4. Spatially resolved measurements of optical losses for the central 2 mm of a) an all-crystalline mirror, and b) hybrid mirror. The value at each point was taken to be the median value of 10 consecutive measurements. Sample pitch was 0.1 mm. This measurement reveals a significant enhancement in uniformity (smaller range of loss values) for the hybrid mirrors, likely given the reduced defect density from the single bonding step. Photos of example mirrors are shown in the insets.

$0.0246\,\mathrm{cm}^{-1} \pm 0.0030\,\mathrm{cm}^{-1}$, and an extinction coefficient of $k_{\mathrm{coat}} = (8.7 \pm 1.1) \times 10^{-7}$ for the coating.

The lowest losses observed for the hybrid mirrors was 7.70 ± 0.27 ppm, corresponding to an even higher finesse of $409\,000 \pm 14\,000$, which represents nearly an order of magnitude increase over any reported conventional coating in the MIR. Again, subtracting T_0 (determined for the hybrid coating structure), we observe a similar level of $S + A = 5.17$ ppm. This is consistent with the all-crystalline results given that the field penetration depth is substantially shallower than the thickness of the epitaxial multilayer.

It is known from [8] that MIR crystalline coatings can exhibit polarization-dependent absorption. We performed an empirical verification by rotating both the laser polarization as well as the coating axes. Within the precision of our ring-down spectrometer, we observed no change in loss with laser and mirror rotation for both types of mirrors. It is not yet clear why these stacked coatings show little to no orientation-dependent losses and further investigations are ongoing.

By successively repositioning the mirrors (and realigning to ensure the curved surface of the mirrors remain normal to the laser), it was possible to map the optical losses across the coating [13]. Figure 4.4 shows the measured losses in the central 2 mm for a representative unit of each mirror type. Variations are obvious on the all-crystalline mirror, and we attribute these to the combined imperfections from the double-bonding process. It is evident that the hybrid mirror greatly improves uniformity by avoiding the additional epitaxial growth defects from a second half-stack, as well as from the reduced complexity of the single bonding step.

Given their improved uniformity and low losses, we explored the performance of the hybrid mirrors in a cavity ring-down apparatus at NIST, Gaithersburg, optimized for trace gas sensing and quantification.

4.3 Applications in gas sensing and spectroscopy

A MIR cavity of unprecedented finesse offers intriguing possibilities for improving the sensitivity of instruments that are widely used for quantitative trace gas sensing. Here, we present a proof-of-concept demonstration of cavity ringdown spectroscopy using a pair of hybrid mirrors forming a 79-cm long cavity. To search for trace amounts of molecular absorption, we flowed a sample of ultra-high purity nitrogen (N_2; 99.999%) through the cavity at a pressure of 13 kPa and a temperature of 297 K. Similar ultra-high purity gases are used in precision gas mixing as balance gases and as feed gases in the semiconductor industry, where purity is of paramount importance in achieving high yield. Figure 4.5(a) shows an isolated absorption line from residual nitrous oxide (N_2O), detected at an amount fraction of 141 ppt $\pm$ 3 ppt. In a nearby spectral window, Fig. 4.5(b) shows an absorption line from residual carbon monoxide (CO), detected at an amount fraction of $37.78\,\mathrm{ppb} \pm 0.12\,\mathrm{ppb}$ (N_2O also makes a minor contribution). These observed amounts are two to three orders-of-magnitude below atmospheric abundances for N_2O and CO.

Separately, we measured the Allan deviation of the empty-cavity absorption coefficient (α_0) at a fixed wavelength of 4.527 µm [Fig. 4.5(c)] and determined a minimum absorption coefficient of $\alpha_{\mathrm{min}} = 2.5 \times 10^{-11}\,\mathrm{cm}^{-1}$ achieved at 8 s. For timescales below 8 s, the Allan deviation approximately follows a $t^{-1/2}$ dependency (dashed trendline), indicating that measurements were dominated by white noise, before being affected by drifts. The value of α_{min} corresponds to a noise-equivalent concentration for N_2O and CO of 0.3 ppt and 2.2 ppt, respectively. These projected limits—established here by proof-of-principle spectroscopy using mirrors fabricated with our breakthrough hybrid MIR coating technology—are substantially better than the sensitivity metrics of existing commercial optical analyzers that operate at similar pressures and temperatures in the same wavelength region (e.g., $\geq$25 ppt N_2O-in-air at 8 s for a sample of

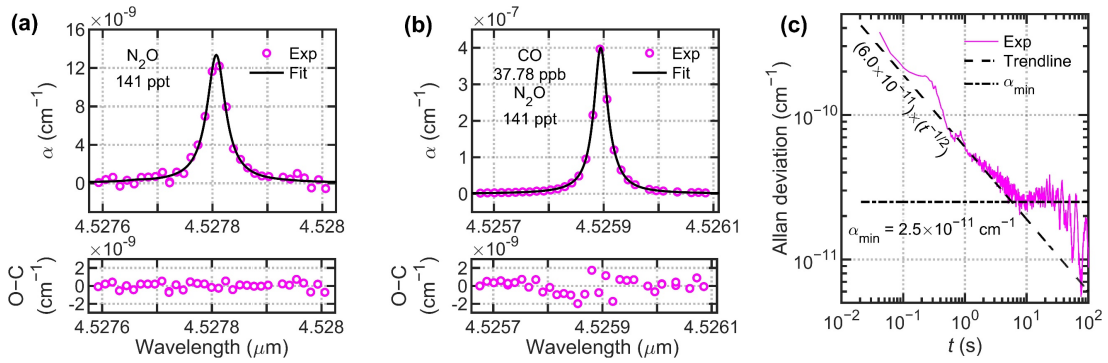

Fig. 4.5. Cavity ring-down spectroscopy reveals trace impurities in ultra-high purity nitrogen (N_2) (a) Nitrous oxide (N_2O) present at 141 ppt. (b) Carbon monoxide (CO) present at 37.66 ppb (with a minor contribution from N_2O). Abbreviation: O − C, observed minus calculated. (c) Allan deviation of empty-cavity time constants (τ_0).

326.5 ppb N_2O-in-air; estimated from data in Table 1, Table 6, and Fig. 3 of [14]). The 4.5 µm spectral region is also of great interest to optical detection of radiocarbon dioxide ($^{14}CO_2$) [5, 15–18], where increased cavity performance can also be of benefit.

In Table 4.1 we compare our Allan deviation results at 1 s from Fig. 4.5(c) to other values found in the literature [16, 19–23]. We compare across similar realizations of linear-absorption cavity ringdown spectroscopy at wavelengths near 4.5 µm where the laser and the cavity are passively coupled, e.g., excluding results that leverage optical feedback self-locking [24] to substantially increase throughput [21]. Also not included are comparisons to non-linear cavity ringdown spectroscopy techniques [7, 15, 17, 25, 26]. To level the comparison with respect to at least one instrumental variable, we normalize the literature values to a common cavity length of 10 cm (assuming that photodetection is detector-noise limited [27] so that the noise equivalent absorption, α at 1 s, is inversely proportional to the square of the cavity length according to $\alpha_0 = (1/(c\tau_0^2))\sigma_{\tau_0}$, where c is the speed of light, $\tau_0 = \mathcal{F}L/(c\pi)$ is the empty cavity decay time, $\mathcal{F}$ is the empty cavity finesse, and σ_{τ_0} is the standard error on τ_0 at 1 s). While some of the groups whose results appear in Table 4.1 have published more recent papers that report modified or applied instrumentation, to the best of our knowledge, we list here the lowest MIR (4.5 µm) 1-s absorption coefficients published to date.

Table 4.1. Performance of comparable cavity ring-down spectrometers operating near 4.5 µm. Here the absorption coefficient (at 1 s integration), cavity length, and normalized performance for each system are shown. The ultralow optical loss of our crystalline coatings yields the lowest normalized noise-equivalent absorption.

Reference	α_0 at 1 s (cm$\sqrt{\text{Hz}}$)	L (m)	α_0 at 1 s for $L = 10$ cm (cm$\sqrt{\text{Hz}}$)
INO-CNR [19]	5.0×10^{-9}	1	5.0×10^{-7}
VTT [20]	2.1×10^{-9}	0.4	3.4×10^{-8}
Nagoya [21]	1.1×10^{-8}	0.11	1.3×10^{-8}
NIST [22]	2.6×10^{-11}	1.5	5.9×10^{-9}
LLNL [16, 23]	1.2×10^{-10}	0.67	5.3×10^{-9}
This work	6.0×10^{-11}	0.79	3.7×10^{-9}

4.4 Outlook

The MIR region has been recognized as a rich portion of the optical spectrum where many species of interest absorb strongly and characteristically. Relative to the rapid maturation of laser source technology (such as QCLs), low loss interference coatings based on conventional deposition techniques have now become the performance-limiting elements of instruments such as cavity ring-down spectrometers. Here we demonstrate a new paradigm for MIR coatings by using two related, but both novel methods. These fundamentally new ultra-high reflectivity coatings are shown to achieve record levels of finesse values in a linear cavity configuration. These ultrahigh finesse values have been achieved with record low excess losses, in combination with comparable transmission values (and being transmission-loss dominated in the case of the all-crystalline mirrors). These metrics are key for applications in which cavity transmission and contrast are paramount.

While the all-crystalline mirrors yield phenomenal results, the double-bonding of the half stacks is a challenging process that introduces roadblocks to scalability in terms of manufacturing and access of longer center wavelengths. As a promising alternative, we demonstrate a novel hybrid mirror structure combin-

ing amorphous multilayers deposited with traditional physical vapor deposition (PVD) processes, capped with a substrate-transferred single-crystal stack. This platform allows for easier fabrication of low-loss MIR mirrors and further extends the operating wavelength of these coatings to the long wavelength limit set by optical phonon absorption in the reststrahlen band beyond approximately 20 µm in GaAs [28, p. 316]. This platform should allow us to realize ppm-levels of excess losses ($<$10 ppm) out to $\sim$7000 nm and $<$50 ppm for wavelengths approaching 11 µm (enabling, for the first time, high-performance CO_2laser optics). Long-wavelength interference coatings capable of ppm-levels of optical losses have the potential to advance capabilities in laser-based manufacturing, including extreme UV lithography.

We anticipate that such coatings will enable spectroscopy at sensitivity levels previously unattainable with existing technologies, furthering tabletop radiocarbon spectrometry [4–6], compact and fieldable atmospheric trace gas detection devices, and chemical sensing instruments [29–31]. Furthermore, the presented mirrors have the potential to significantly advance the capability of high damage threshold [32, 33] and low-loss optics for long-wavelength laser-based manufacturing systems.

4.5 Methods

The ultralow-loss all-crystalline MIR mirrors presented here were fabricated using a process similar to that described in Ref. [8]. Here, a single epi wafer was used for the interference coating, with direct bonding of two half-stack multilayer structures carried out at the die level to build-up the Bragg mirror. This initial bonding step is employed to minimize the density of growth defects in these relatively thick MIR coatings. The advantage is two-fold: i) the shorter growth process for the half mirror minimizes defect incorporation and lowers the overall defect density in the thin films, and ii) defects terminating at the surface of the as-grown crystal are mitigated as they are buried at the bond interface in the middle of the combined stack. Following the initial bonding process, a substrate and etch stop removal process is carried out via selective wet chemical etching, exposing the back surface of one of the half mirror stacks. This exposed face of the epi structure is then directly bonded to a super-polished silicon optical substrate 1 m concave radius of curvature, 6.35 mm thick with a 25.4 mm outer diameter, backside wedged at 0.5°) using a room temperature plasma-activated bonding process. To complete the all-crystalline MIR supermirrors, a second substrate and etch stop removal process is carried out, leaving the stacked crystalline coating transferred to the Si base substrate. Given the need for very thick layers in the all-crystalline approach, mirrors with a transmission below 10 ppm would require additional stacking/bonding steps for wavelengths beyond $\sim$5.5 µm (assuming a maximum epitaxial growth thickness of $\sim$16 µm for maintaining a suitably low defect density below 1000 cm^{-2}). Typical RMS surface roughness below $\sigma = 0.2$ nm is achieved [8], which leads to negligible expected scatter levels of order $1 - \mathrm{Exp}(-(4\pi\sigma/\lambda)^2) \approx 0.3$ ppm [34].

With the hybrid approach, the epitaxial stack can be limited to this maximum thickness value and the underlying amorphous structure can be tailored to tune the transmission. The die level "stacking" process is skipped and the GaAs/AlGaAs disk is instead directly bonded to the surface of a pre-coated Si base wafer. The pre-coating is a partial high reflectivity stack consisting of the amorphous a-Si/SiO_2 layers terminated with a 1/8-wave Al_2O_3 layer. These amorphous films are generated via IBS in a Navigator 1100 (CEC GmbH) coating system using xenon as a sputtering gas. The oxides (SiO_2 and Al_2O_3) are formed by oxidation of metallic Al ($>$99.999% purity) and Si (p-doped $>$99.9999% purity) released from the sputtering targets and adding 70 sccm oxygen to the process chamber for SiO_2 and 90 sccm for Al_2O_3. The a-Si was deposited from a Si (undoped, 99.9999% purity) target without adding any oxygen to the chamber. Before deposition, the vacuum chamber is evacuated to approximately 1×10^{-5} Pa. During deposition, the vacuum pressure did not exceed 0.2 Pa and the substrate holder was heated and temperature controlled to 150 °C. In a first run the a-Si/SiO_2 layers were deposited followed by Al_2O_3 deposition without breaking the vacuum or turning off the plasma source. The entire coating run was controlled and monitored with a broadband optical monitoring system (wavelength range of 250 nm to 2200 nm) on an IR fused silica monitoring glass. After deposition, the films are annealed for 24 hours at 300 °C in an oven at ambient atmosphere (stainless steel hot air oven, Memmert GmbH).

These prototype MIR mirrors employ 8 mm diameter epitaxial coating discs. This small crystalline coat-

ing area was used to conserve material during test mirror production. It is important to note that we can routinely produce much larger crystalline mirrors, with high-performance 10-cm diameter crystalline coatings recently demonstrated [35].

To accurately determine the minimum transmission value for each mirror, we must determine the refractive indices and physical thicknesses of each layer. As the all-crystalline mirrors consist of only two materials, the process is simpler. In this case, we first determine the exact alloy composition of the low index $Al_xGa_{1-x}As$ layers, then extract the thicknesses of the films in the as-grown multilayer structure. XRD is employed to determine the AlAs mole fraction, x, in the ternary $Al_xGa_{1-x}As$ alloy as $x = 92.9\%$ in the as-grown 22.25-period epitaxial half-stack material. Individual layer thicknesses were determined via SEM imaging of a cleaved sample of the MBE-grown multilayer. These were evaluated line-by-line, resulting in a large sample size that drastically improved the statistical uncertainty of the thickness determinations (the exact process is described in [12]). However, it is known that deposition rate variations across the MBE platen will lead to modest differences in the absolute layer thicknesses across the wafer (or across various wafers dependent on the growth configuration), while the ratio of thicknesses are maintained [36]. That is, we expect the layer thicknesses in our mirrors to be related to the cleaved sample by a single rescaling parameter, i.e., by multiplying the obtained thickness values by a single factor d_{scale}.

These unavoidable variations in alloy fractions and thickness in the MBE growth process led to a deviation of the actual transmittance spectrum from the design target. To obtain an accurate transmittance T spectrum over the stopband region, including the region of lowest losses around the mirror center wavelength λ_0, we employed an improved variant of the approach presented in [8]. We recorded a transmission spectrum of the all-crystalline mirrors with a Fourier-transform Spectrometer (FTS, Bruker VERTEX 80v). An example spectrum is shown in Fig. 4.6. These broadband measurements were recorded in vacuum (220 Pa) with a resolution of $0.5\,\mathrm{cm}^{-1}$. Due to the limited sensitivity and low signal-to-noise ratio (SNR) in the spectral region around λ_0, the transmittance cannot be directly probed. However, the width of the stopband and the characteristic structure of the sidelobes allow for a precise interpolation if the layer thicknesses of the layers are accurately known. Knowing both, the broadband transmittance spectrum and the physical layer thicknesses allows us to fit a transfer-matrix method (TMM) model to the FTS data to obtain accurate transmittance values in the stopband region. In this curve-fitting exercise, we modeled the layer structure using refractive index values measured in-house for the GaAs and AlGaAs layers using the cleaved sample of epitaxial material grown in the same run as for the completed mirrors (see [12] for details), while for the Si substrate we used values from [37], and $n = 1$ for incidence and exit media. Note that we assumed abrupt interfaces and no variation in AlAs mole fraction throughout the structure, as well as a perfect AR coating on the back surface of the substrate.

The subsequent fit routine had three free parameters: The aforementioned multiplicative scaling factor d_{scale} on layer thicknesses, a global scaling parameter T_{scale} to counteract photometric inaccuracies in FTS imaging due to geometric effects (mostly caused by the relatively thick, wedged, and highly refractive Si substrate), and finally a single scaling parameter for the middle GaAs layer (formed of the two 1/8-wave caps of the half-mirrors) to counteract a systematic error in SEM imaging. The measured film parameters were varied within their respective error bounds using a Monte-Carlo-style approach to obtain an estimate of the uncertainty of the transmittance at the stopband center T_0.

For the hybrid mirrors, the crystalline stack came from the same epi wafer as employed for the all-crystalline mirrors, thus those findings (in terms of physical thicknesses and refractive indices) can be directly used. The challenge in the case of these structures, now consisting of five materials instead of two, is the fact that the amorphous materials have less well-defined refractive index values. Thus, we undertake a similar systematic study of the amorphous materials, including ellipsometry (SENresearch 4.0 and SENDIRA, SENTECH Instruments GmbH) on single films deposited and processed under identical conditions, photometric measurements in the NIR and MIR (Agilent Cary5000, ThermoFisher Nicolet iS50) on witness pieces and single films, etc. in order to estimate the transmission of the completed hybrid mirror. In this case, larger error bounds remain for the refractive indices and physical thicknesses of the amorphous films and we will pursue more in-depth analysis

of these materials in follow-on work. Additionally, advances in epitaxy exploiting alternative material platforms could enable wider bandwidth mirrors via enhanced index contrast [38], however, it remains to be seen whether such material systems will be capable of sufficiently low optical loss.

The higher index contrast achievable with the amorphous sub-stack resulted in a wider stopband than the all-crystalline coating, as determined by the wavelength range over which the calculated transmission increased by a factor of two (approximately 180 nm and 130 nm for the hybrid and all-crystalline coatings, respectively).

To perform spectroscopy, a continuous-wave distributed feedback quantum cascade laser (DFB-QCL) is tuned in steps of 0.013 nm (equal to the cavity free-spectral range, $\nu_{\mathrm{fsr}} = 189\,\mathrm{MHz}$) around 4.52 µm and cavity transmission is measured on a cryogen-cooled InSb detector, amplified, and digitized for analysis. An acousto-optic switch is used to shutter the laser pumping of the cavity when a predetermined transmission threshold is met and then the optical decay is recorded. The empty-cavity time constant was $\tau_0 = 128\,\mu\mathrm{s}$ which, for a cavity length of 79 cm, equates to a round-trip loss of $1 - R = 21$ ppm—a value consistent with the data plotted in Fig. 4.3. An example of a raw time-domain optical decays is shown in Fig. 4.7.

The cavity construction rigidly mounted the hybrid mirrors within a flow cell, using Invar rods to mitigate against drifts in cavity length due to variations in laboratory temperature. The gas sample is introduced as a continuous flow at a nominal rate of 20 standard cubic centimeters per minute (sccm) and pressure of 13 kPa. The pressure is stabilized using a back pressure controller and monitored by pressure gauges calibrated to NIST secondary standards. The temperature of the outer walls of the flow cell—assumed equal to the temperature of the sample gas—is measured by two NIST-calibrated platinum resistance thermometers to be 297 K.

The amount fractions of molecular impurities found in the ultra-high purity N_2 gas sample are determined by fitting Voigt line shape functions to the measured spectra using parameters from the HITRAN2020 database [39] as initial guesses. The temperature and pressure of the gas sample are fixed to the measured experimental values and the following parameters are floated in each fit: an absolute frequency offset, N_2O or CO amount fraction and a linear baseline model for τ_0. For the spectrum containing CO absorption, the N_2O amount fraction is fixed to the fitted value determined from the isolated line, and the following two additional parameters are floated: pressure-broadening coefficient for CO and relative frequency between the CO (strong) and N_2O (weak) transitions.

The calculation of noise-equivalent amount fractions for N_2O and CO is done for the transitions shown in Fig. 4.5(a–b) using the HITRAN2020 database [39] and a Voigt line shape function modeled at a pressure of 5 kPa and a temperature of 296 K—pressure and temperature conditions commonly used in commercial sensors like those reported in [14].

Acknowledgments

We thank C. Manning, A. Helbers, and M. Philippou for an inhouse FP-QCL monitoring solution; Y. Dikmelik for the FP-QCL source; J.T. Hodges for early manuscript review. A portion of this work was performed in the UCSB Nanofabrication Facility, an open access laboratory, and at the Faculty Center for Nano Structure Research at the University of Vienna. Funding sources: Thorlabs internal; NIST internal; National Foundation for Research, Technology and Development; Austrian Science Fund, FWF, (P 36040); Schweizerischer Nationalfonds zur Förderung der Wissenschaftlichen Forschung (SNSF) (206021_198176). The financial support by the Austrian Federal Ministry for Labour and Economy and the National Foundation for Research, Technology and Development and the Christian Doppler Research Association is gratefully acknowledged.

Author contributions

GWT and LWP contributed equally to this work. GWT, LWP, GW, and SBCL measured the mirror performance. GWT, LWP, and VW characterized and modeled the crystalline and amorphous mirror materials. GDC designed the interference coatings and CN, GDC, and DF performed the crystalline coating process. VW co-designed the hybrid mirrors and deposited the amorphous multilayer structures via IBS under the supervision of TS. DMB and AJF performed the spectroscopic measurements. OHH and GDC provided technical oversight and experimental design. All authors contributed to the manuscript.

Competing interests

LWP, GW, and OHH are partially funded by Thorlabs, Inc; Thorlabs, Inc holds patents related to this work Certain instruments are identified in this paper in order to specify the experimental procedure adequately. Such identification is not intended to imply recommendation or endorsement by NIST, nor is it intended to imply that the instruments identified are necessarily the best available for the purpose.

Materials and correspondence

Data generated in this study are available from the corresponding authors and data.nist.gov upon reasonable request.

References

[1] G. Rempe, R. Lalezari, R. J. Thompson, and H. J. Kimble, "Measurement of ultralow losses in an optical interferometer", Opt. Lett. **17**, 363 (1992).

[2] N. Jin, C. A. McLemore, D. Mason, J. P. Hendrie, Y. Luo, M. L. Kelleher, P. Kharel, F. Quinlan, S. A. Diddams, and P. T. Rakich, "Microfabricated mirrors with finesse exceeding one million", Optica **9**, 965 (2022).

[3] C. A. McLemore, N. Jin, M. L. Kelleher, J. P. Hendrie, D. Mason, Y. Luo, D. Lee, P. Rakich, S. A. Diddams, and F. Quinlan, *Thermal noise-limited laser stabilization to an 8 mL volume Fabry-Pérot reference cavity with microfabricated mirrors*, (2022) arXiv:2203.15915v1, preprint.

[4] M. G. Delli Santi, S. Bartalini, P. Cancio, I. Galli, G. Giusfredi, C. Haraldsson, D. Mazzotti, A. Pesonen, and P. De Natale, "Biogenic Fraction Determination in Fuel Blends by Laser-Based $^{14}CO_2$ Detection", Adv. Photonics Res. **2**, 2000069 (2021).

[5] A. J. Fleisher, D. A. Long, Q. Liu, L. Gameson, and J. T. Hodges, "Optical Measurement of Radiocarbon below Unity Fraction Modern by Linear Absorption Spectroscopy", J. Phys. Chem. Lett. **8**, 4550 (2017).

[6] R. Terabayashi, V. Sonnenschein, H. Tomita, N. Hayashi, S. Kato, L. Jin, M. Yamanaka, N. Nishizawa, A. Sato, K. Nozawa, et al., "Optical feedback in dfb quantum cascade laser for mid-infrared cavity ring-down spectroscopy", Hyperfine Interact. **238**, 10 (2017).

[7] A. D. McCartt and J. Jiang, "Room-Temperature Optical Detection of $^{14}CO_2$ below the Natural Abundance with Two-Color Cavity Ring-Down Spectroscopy", ACS Sens. **7**, 3258 (2022).

[8] G. Winkler, L. W. Perner, G.-W. Truong, G. Zhao, D. Bachmann, A. S. Mayer, J. Fellinger, D. Follman, P. Heu, C. Deutsch, et al., "Mid-infrared interference coatings with excess optical loss below 10 ppm", Optica **8**, 686 (2021).

[9] G. D. Cole, W. Zhang, M. J. Martin, J. Ye, and M. Aspelmeyer, "Tenfold reduction of Brownian noise in high-reflectivity optical coatings", Nat. Photonics **7**, 644 (2013).

[10] G. D. Cole, W. Zhang, B. J. Bjork, D. Follman, P. Heu, C. Deutsch, L. Sonderhouse, J. Robinson, C. Franz, A. Alexandrovski, et al., "High-performance near- and mid-infrared crystalline coatings", Optica **3**, 647 (2016).

[11] D. Babic and S. Corzine, "Analytic expressions for the reflection delay, penetration depth, and absorptance of quarter-wave dielectric mirrors", IEEE J. Quantum Electron. **28**, 514 (1992).

[12] L. W. Perner, G.-W. Truong, D. Follman, M. Prinz, G. Winkler, S. Puchegger, G. D. Cole, and O. H. Heckl, "Simultaneous measurement of mid-infrared refractive indices in thin-film heterostructures: Methodology and results for GaAs/AlGaAs", Phys. Rev. Research **5**, 033048 (2023).

[13] G. W. Truong, G. Winkler, T. Zederbauer, D. Bachmann, P. Heu, D. Follman, M. E. White, O. H. Heckl, and G. D. Cole, "Near-infrared scanning cavity ringdown for optical loss characterization of supermirrors", Opt. Express **27**, 19141 (2019).

[14] S. J. Harris, J. Liisberg, L. Xia, J. Wei, K. Zeyer, L. Yu, M. Barthel, B. Wolf, B. F. J. Kelly, D. I. Cendón, et al., "N_2O isotopocule measurements using laser spectroscopy: Analyzer characterization and intercomparison", Atmos. Meas. Tech. **13**, 2797 (2020).

[15] I. Galli, S. Bartalini, S. Borri, P. Cancio, D. Mazzotti, P. De Natale, and G. Giusfredi, "Molecular Gas Sensing Below Parts Per Trillion: Radiocarbon-Dioxide Optical Detection", Phys. Rev. Lett. **107**, 270802 (2011).

[16] A. D. McCartt, T. J. Ognibene, G. Bench, and K. W. Turteltaub, "Quantifying Carbon-14 for Biology Using Cavity Ring-Down Spectroscopy", Anal. Chem. **88**, 8714 (2016).

[17] I. Galli, S. Bartalini, R. Ballerini, M. Barucci, P. Cancio, M. De Pas, G. Giusfredi, D. Mazzotti, N. Akikusa, and P. De Natale, "Spectroscopic detection of radiocarbon dioxide at parts-per-quadrillion sensitivity", Optica **3**, 385 (2016).

[18] V. Sonnenschein, R. Terabayashi, H. Tomita, S. Kato, N. Hayashi, S. Takeda, L. Jin, M. Yamanaka, N. Nishizawa, A. Sato, et al., "A cavity ring-down spectrometer for study of biomedi-

cal radiocarbon-labeled samples", J. Appl. Phys. **124**, 033101 (2018).

[19] P. Cancio, S. Bartalini, S. Borri, I. Galli, G. Gagliardi, G. Giusfredi, P. Maddaloni, P. Malara, D. Mazzotti, and P. De Natale, "Frequency-comb-referenced mid-IR sources for next-generation environmental sensors", Appl. Phys. B **102**, 255 (2011).

[20] G. Genoud, M. Vainio, H. Phillips, J. Dean, and M. Merimaa, "Radiocarbon dioxide detection based on cavity ring-down spectroscopy and a quantum cascade laser", Opt. Lett. **40**, 1342 (2015).

[21] R. Terabayashi, K. Saito, V. Sonnenschein, Y. Okuyama, K. Iwamoto, K. Mano, Y. Kawashima, T. Furumiya, K. Tojo, S. Ninomiya, et al., "V-cavity stabilized quantum cascade laser-based cavity ringdown spectroscopy for rapid detection of radiocarbon below natural abundance", J. Appl. Phys. **132**, 083102 (2022).

[22] D. A. Long, A. J. Fleisher, Q. Liu, and J. T. Hodges, "Ultra-sensitive cavity ring-down spectroscopy in the mid-infrared spectral region", Opt. Lett. **41**, 1612 (2016).

[23] A. D. McCartt, "Development of a low-temperature cavity ring-down spectrometer for the detection of carbon-14", PhD thesis (Stanford University, Stanford, CA, United States, 2014).

[24] G. Maisons, P. G. Carbajo, M. Carras, and D. Romanini, "Optical-feedback cavity-enhanced absorption spectroscopy with a quantum cascade laser", Opt. Lett. **35**, 3607 (2010).

[25] G. Zhao, D. M. Bailey, A. J. Fleisher, J. T. Hodges, and K. K. Lehmann, "Doppler-free two-photon cavity ring-down spectroscopy of a nitrous oxide (N_2O) vibrational overtone transition", Phys. Rev. A **101**, 062509 (2020).

[26] J. Jiang and A. D. McCartt, "Two-color, intracavity pump–probe, cavity ringdown spectroscopy", J. Chem. Phys. **155**, 104201 (2021).

[27] H. Huang and K. K. Lehmann, "Sensitivity Limits of Continuous Wave Cavity Ring-Down Spectroscopy", J. Phys. Chem. A **117**, 13399 (2013).

[28] S. Adachi, *Properties of Semiconductor Alloys*, red. by P. Capper, S. Kasap, and A. Willoughby, Wiley Series in Materials for Electronic & Optoelectronic Applications (John Wiley & Sons, Ltd, Chichester, UK, 2009).

[29] B. J. Bjork, T. Q. Bui, O. H. Heckl, P. B. Changala, B. Spaun, P. Heu, D. Follman, C. Deutsch, G. D. Cole, M. Aspelmeyer, et al., "Direct frequency comb measurement of OD + CO → DOCO kinetics", Science **354**, 444 (2016).

[30] M. Yumoto, Y. Kawata, and S. Wada, "Mid-infrared-scanning cavity ring-down CH_2F_2 detection using electronically tuned Cr:ZnSe laser", Sci. Rep. **12**, 7879 (2022).

[31] C. Kloss, V. Tan, J. B. Leen, G. L. Madsen, A. Gardner, X. Du, T. Kulessa, J. Schillings, H. Schneider, S. Schrade, et al., "Airborne Mid-Infrared Cavity enhanced Absorption spectrometer (AMICA)", Atmos. Meas. Tech. **14**, 5271 (2021).

[32] G. D. Cole, D. Follman, P. Heu, G.-W. Truong, C. Deutsch, C. Franz, A. L. Alexandrovski, B. Ma, and X. Cheng, "Laser-induced damage measurements of crystalline coatings (Conference Presentation)", in Laser-Induced Damage in Optical Materials 2018: 50th Anniversary Conference, Vol. 10805, edited by C. W. Carr, G. J. Exarhos, V. E. Gruzdev, D. Ristau, and M. Soileau, Proceedings of SPIE (2018).

[33] G. D. Cole, C. Nguyen, D. Follman, G.-W. Truong, E. Krause, and T. Böhme, "A high-power-handling deformable mirror system employing crystalline coatings", in Laser-Induced Damage in Optical Materials 2022, Vol. 12300, edited by C. W. Carr, D. Ristau, and C. S. Menoni, Proceedings of SPIE (2022), p. 123000D.

[34] H. Davies, "The reflection of electromagnetic waves from a rough surface", Proc. IEE - IV: Inst. Monogr. **101**, 209 (1954).

[35] G. D. Cole, S. W. Ballmer, G. Billingsley, S. B. Cataño-Lopez, M. Fejer, P. Fritschel, A. M. Gretarsson, G. M. Harry, D. Kedar, T. Legero, et al., "Substrate-transferred GaAs/AlGaAs crystalline coatings for gravitational-wave detectors", Appl. Phys. Lett. **122**, 110502 (2023).

[36] P. Koch, G. D. Cole, C. Deutsch, D. Follman, P. Heu, M. Kinley-Hanlon, R. Kirchhoff, S. Leavey, J. Lehmann, P. Oppermann, et al., "Thickness uniformity measurements and damage threshold tests of large-area GaAs/AlGaAs crystalline coatings for precision interferometry", Opt. Express **27**, 36731 (2019).

[37] D. Chandler-Horowitz and P. M. Amirtharaj, "High-accuracy, midinfrared (450 $cm^{-1} \leq \omega \leq$ 4000 cm^{-1}) refractive index values of silicon", J. Appl. Phys. **97**, 123526 (2005).

[38] S. Schön, M. Haiml, and U. Keller, "Ultrabroadband AIGaAs/CaF_2 semiconductor saturable absorber mirrors", Appl. Phys. Lett. **77**, 782 (2000).

[39] I. Gordon, L. Rothman, R. Hargreaves, R. Hashemi, E. Karlovets, F. Skinner, E. Conway, C. Hill, R. Kochanov, Y. Tan, et al., "The HITRAN2020 molecular spectroscopic database", J. Quant. Spectrosc. Radiat. Transfer **277**, 107949 (2022).

Mid-infrared supermirrors with finesse exceeding 400 000: Supplement

Bibliographical information

The contents of this section were submitted together with the current version of the manuscript in Chapter 4 after peer-review. This version was received by the journal on 11 September 2023 and sent to the referees on 12 September 2023 for confirmation.

Minor typographical errors were silently corrected and the formatting has been carefully adapted for the purpose of this thesis, while the results remain unchanged. The original title and authors correspond to the chapter title and authors. Author affiliations are given as they appear in the original publication.

4.6 Mid-infrared supermirrors with finesse exceeding 400 000: Supplemental document

As described in the Methods section, we estimate mirror transmittance T based on a best-fit transmission matrix model (TMM) seeded with measurements of both a broadband transmittance spectrum via Fourier-transform spectrometer (FTS) and Bragg-mirror layer thicknesses via scanning-electron microscope (SEM). Figure 4.6(top) shows the data and best-fit TMM model in a broader spectral range, while Fig. 4.6(bottom) illustrates how we overcome SNR-limitations in FTS transmittance measurements using our approach.

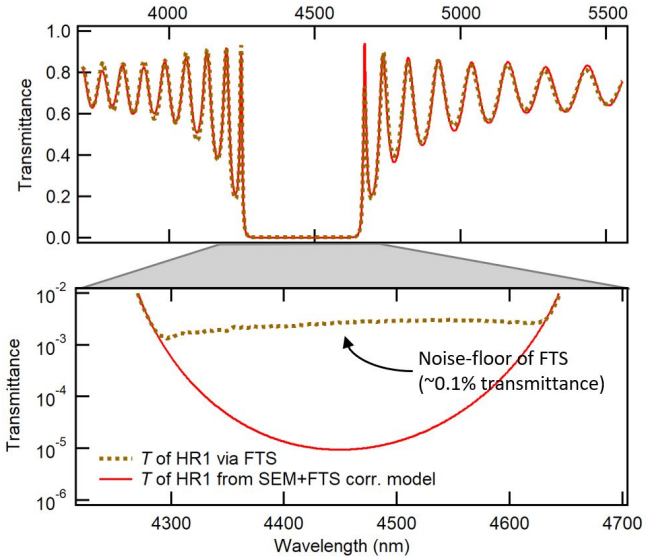

Fig. 4.6. (top) Broadband FTS transmittance of HR1, one of the all-crystalline supermirrors, compared to a TMM computation pinned to SEM and FTS measurements, as well as known refractive indices. (bottom) Zoomed-in view near the transmittance minimum, showing that the FTS lacks sufficient transmittance accuracy within the stop band.

Figure 4.7(a–h) show typical time-domain optical decay signals, fit residuals, and the distribution of measured time constants for measurements using our lossmeter (cavity length of 145 mm), which was used to determine mirror performance. Figure 4.7(i–j) shows a typical ring-down curve and fit residuals for the ring-down spectrometer (cavity length of 79 cm), which was used for our proof-of-principle spectroscopy measurements.

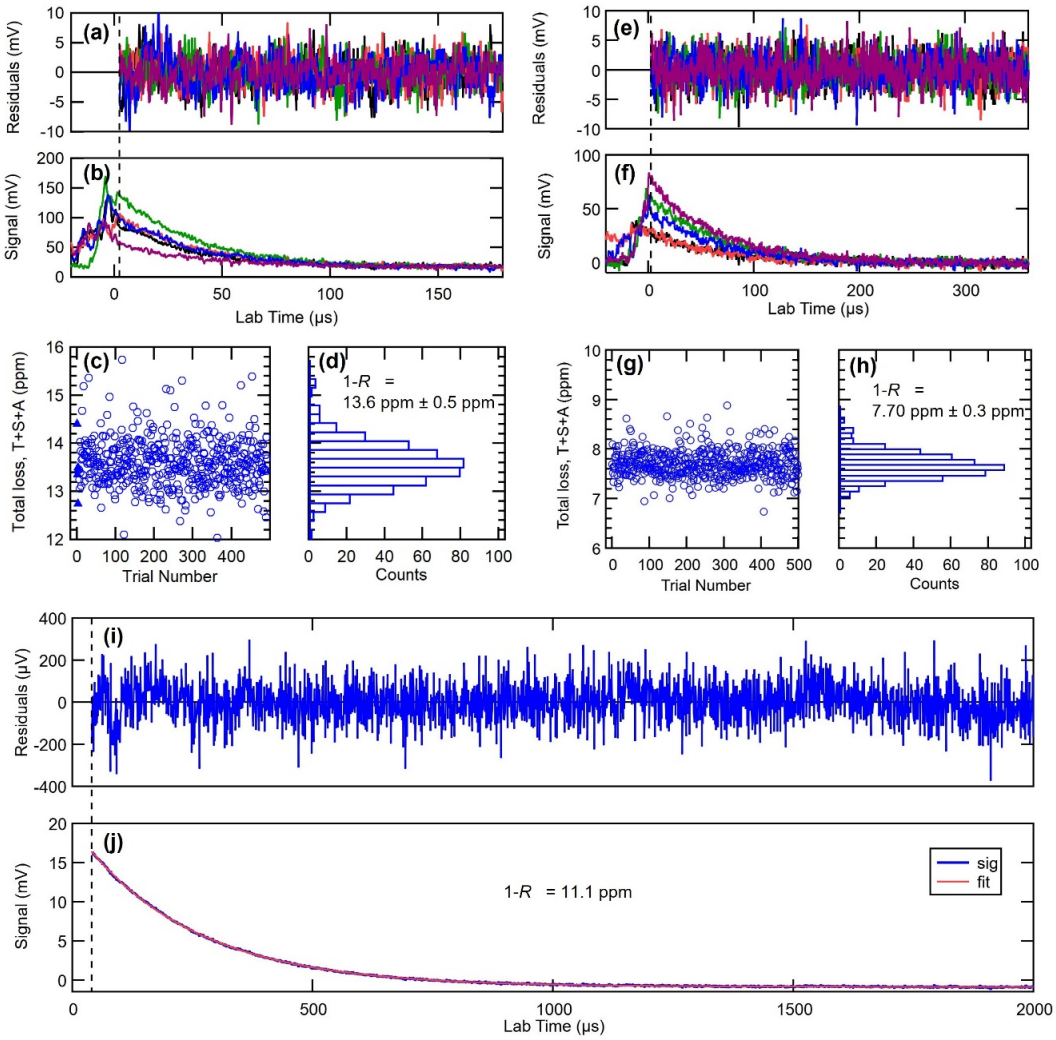

Fig. 4.7. (a–d): Consecutive ring-downs taken at a particular location on the all-crystalline mirrors. SNR $\sim$ 40, depending on trace. (e–h): Consecutive ring-downs taken at a particular location on the hybrid mirrors. SNR $\sim$ 20. (i–j): a single ring-down measurement taken at a particular location on the hybrid mirrors using the evacuated 79-cm cavity spectrometer. The small difference in the measured reflectivity of the hybrid mirrors taken from the 145-mm coating lossmeter and in the 79-cm spectrometer is due to difference in experimental conditions (such as spot size and location). All ring-downs were taken at $\lambda = 4.45\,\mu$m.

5 Conclusions and outlook

This thesis chronicles a structured progression in the research and development of substrate-transferred crystalline supermirrors, particularly tailored for the mid-infrared range. The journey began with the study presented in Chapter 2, which sought to improve on first results on substrate-transferred crystalline coatings at 3310 nm and 3730 nm in Cole et al. [1]. In the course of this study, we demonstrated the first mid-infrared HR coatings with total loss $1 - R$ of 151 ± 3 ppm and excess loss (absorption plus scatter $A + S$) on the single-ppm level at a central wavelength of 4535 nm. This constituted a five-fold improvement in reflectivity over the mirrors presented in [1]. In the course of this effort, we also developed several setups, adapting well-established measurement techniques for the specific requirements of mid-infrared mirror coatings. Importantly, we also gained valuable theoretical understanding necessary for our subsequent research endeavors, partly chronicled in Chapters 3 and 4. This study highlighted the complexities of developing crystalline mid-infrared interference coatings—including a newly-observed polarization-dependent loss in GaAs/$Al_xGa_{1-x}As$—with minimized optical losses. This emphasized the need for advanced fabrication methodologies and a deeper understanding of material behavior.

Transitioning to the work in Chapter 3, the focus shifted to foundational research, simultaneously measuring the refractive index of GaAs and $Al_xGa_{1-x}As$ by directly probing as-grown crystalline heterostructures (also used to produce the mirrors presented in Chapter 4). In the course of this work, which required precision metrology, we developed a general method to accurately and precisely characterize relevant optical materials directly in thin-film multilayers. This approach allowed us to extract both refractive indices from a single structure with a relative standard uncertainty of ca. 3×10^{-4} for both materials. This study delved into the fundamental properties of the materials used in substrate-transferred crystalline optical coatings. The goal was to optimize the design and production process for future optical coatings for the mid-infrared range, where precise knowledge of basic material parameters is paramount to minimize deviations from design targets. The challenges identified in Chapter 2 were catalysts for this endeavour, driving us to explore the basic properties of GaAs and $Al_xGa_{1-x}As$ in greater depth.

Chapter 4, in particular, was the culmination of efforts in advancing pure crystalline technology at mid-infrared wavelengths. The presented results are a significant milestone in the development of all-crystalline substrate-transferred coatings, obtaining a record-high finesse of $231\,000 \pm 8400$ (corresponding to a single-mirror total loss $1-R$ of 13.60 ± 0.49 ppm) in a two-mirror optical cavity while maintaining the ppm-level excess loss we demonstrated for lower-reflectivity mirrors in Chapter 2. This showcased the improvements in all-crystalline technology, pushing it to its current limits. However, the standout achievement was the

development of hybrid mirrors. These HR coatings achieved a finesse of 409 000 ± 14 000 ($1 - R$ of 7.70 ± 0.27 ppm) by combining state-of-the-art crystalline and amorphous thin-film heterostructures. Using these hybrid mirrors, we achieved one of the lowest noise-equivalent absorption values to date in first spectroscopic measurements. The comparison with traditional mirrors produced by physical vapor deposition techniques, as discussed in Sections 2.1 and 4.1, provides insights into the current performance of these all-amorphous Bragg mirrors, highlighting the advantages of the crystalline and hybrid approaches. Furthermore, the combination of amorphous IBS-deposited base structures with substrate-transferred crystalline coatings overcomes the current limitations of all-crystalline mirrors. Hence, the hybrid mirrors not only showcased enhanced reflectivity but also signified the potential for extending the technology to even longer wavelengths.

5.1 Implications for the field

The advancements in substrate-transferred crystalline mirrors, both pure and hybrid, have profound implications for the broader fields of optical technology and photonics. In general, low-loss optical devices based on thin-film heterostructures were key in various breakthrough advancements, from semiconductor saturable-absorber mirrors (SESAMs) [2, 3] and gravitational wave detection [4, 5] to chemical kinetics [6]. In the mid-infrared in particular, the performance of crystalline and hybrid coatings has now surpassed current all-amorphous coatings by a substantial amount (see Chapter 4). This enhanced performance in the mid-infrared range opens up new avenues for various applications.

As mentioned in Chapter 1, one of the immediate uses of the advanced mirrors is precision spectroscopy and trace gas sensing around 4.5 µm. Section 4.3 already demonstrates the importance of high-reflectivity mirrors in this domain, that is largely dominated by cavity-enhanced techniques [7]. As outlined there, this wavelength range is of particular interest for the detection of radiocarbon dioxide $^{14}CO_2$ [8–12]. For example, this is of paramount importance in differentiating carbon compounds from biogenic and petrogenic sources, with important applications related to climate change, such as precision measurement of bio-fossil fuel blends [13]. The enhanced reflectivity and minimized absorption loss of the here-presented mirrors can significantly improve the sensitivity of such spectroscopic measurements, paving the way for various applications in trace-gas sensing.

Since hybrid coatings allow for a expansion to even longer wavelengths, another promising avenue is the development of high-performance thin-film coatings for CO_2-laser applications around 10.6 µm, which are widely used in medicine [14] and industry [15, 16]. The advancements presented in Chapter 4 should allow the development up to ca. 11 µm, surpassing damage thresholds and optical losses of current mirrors for CO_2-laser applications substantially [17, 18], as mentioned in Section 4.4.

On the other hand, the results presented in Chapter 3 have immediate implications for the design and manufacturing of many active and passive optical devices, some of which

are mentioned in Section 3.1. The refractive index n is a fundamental material property that influences important specifications, such as the central wavelength of Bragg mirrors or quantum cascade lasers (QCLs). Hence, the development and fabrication of optical devices in the MIR will benefit from the presented updated values. Additionally, our own characterization efforts for hybrid mirrors in Section 4.5 are testament to the fact that many materials used in thin-film heterostructures remain poorly characterized at MIR wavelengths. Hence, we anticipate that the method presented in Chapter 3 itself will prove useful in the characterization of many other crystalline and amorphous materials, especially in the MIR. This will be necessary for hybrid mirror technology, among many other optical devices, such as superluminiscent diodes [19] or QCLs [20].

5.2 The future of mid-infrared optical coatings

The research presented in this thesis represents only a point in the ongoing advancement of mid-infrared optical coatings and the future holds promise for further innovations and applications.

As already mentioned in Chapter 4 and Section 5.1, one of the immediate research trajectories is the extension of the hybrid mirror technology to even longer wavelengths, with a significant milestone at the application-rich wavelength range around 10.6 µm. With efforts to manufacture hybrid mirrors at 7.8 µm already underway, there is potential to push the boundaries further with successive iterations. The combination of crystalline technology with amorphous thin films offers a versatile platform that can be tailored to specific wavelength requirements, as replacing part of an all-crystalline design allows to grow thinner structures during molecular beam epitaxy. That way, the thickness limitations during growth and substrate transfer (discussed, e.g., in Chapters 1 and 4, as well as Ref. [1]) are relaxed compared to all-crystalline designs.

This push for longer wavelengths has various implications. One of the most immediate necessities is to find suitable substrate materials for wavelengths above ca. 6 µm, as crystalline silicon starts to exhibit excess loss at this wavelength. In addition, super-polished substrates are required to allow for the adhesive-free bonding of crystalline coatings, germanium is a promising candidate. This is due its similarities with silicon, availability, and applicability at wavelengths up to 11.5 µm.

In parallel to the research on materials and coatings, technological advancements in fabrication and characterization techniques will play a pivotal role. The progression of heterostructures to longer wavelengths will be a major challenge. To meet the demands of cutting-edge optical coatings beyond 5 µm, particularly existing PCI and CRD setups (see Chapters 2 and 4) will need to be extended to exceedingly longer wavelengths.

As the technology matures, a plethora of other applications could emerge. The immediate implications for spectroscopy and CO_2 laser applications have been discussed in Section 5.1, but the enhanced performance of these mirrors could find utility in other domains as well.

As outlined in Chapter 1 and Section 4.4, some potential fields include environmental monitoring, biomedical applications, and even future spaceborne experiments could benefit from the advancements in mid-infrared optical coatings.

As also emphasized in Chapter 1, future advancements will likely emerge from collaborative efforts. This already happened in the case of the hybrid coatings, where the combination of know-how on crystalline mirrors, amorphous coatings, and precision spectroscopy led to the advent of hybrid amorphous-crystalline coatings and their first application in trace gas sensing. Future interdisciplinary research—combining insights from materials science, optical device development, and photonics applications—will be instrumental in driving innovation in mid-infrared optical coatings.

Particularly, a possible strand of research could be the characterization and tailoring of mirror dispersion to manufacture so-called *chirped mirrors* [21–24]. For example, these chirped mirrors would allow for more efficient use of high-reflectivity mirrors in combination with broadband stabilized frequency-comb sources in cavity-enhanced spectroscopy [7], maximizing the simultaneous bandwidth of these devices. This will also require the development of efficient characterization setups capable of measuring the group delay dispersion over a broad bandwidth in the MIR.

5.3 Final thoughts

Scientific research is inherently iterative, characterized by cycles of observation, hypothesis formulation, further experimentation, data analysis, and theory refinement [25]. The present thesis exemplifies this process, with each study building upon the findings of the previous, leading to continuous refinement of fundamental understanding and technology in the dynamic and evolving realm of mid-infrared optical coatings. The initial challenges identified in Ref. [1] and Chapter 2 served as catalysts for the foundational research presented in Chapter 3, all of which, in turn, paved the way for the advancements in Chapter 4.

Fleck [25] also emphasized the collective nature of scientific discovery. The advancements in all-crystalline and especially hybrid mid-infrared optical coatings, as presented in Chapters 2 to 4, are a testament to collaborative efforts, with interdisciplinary insights driving innovation. While not exactly a paradigm shift in the Kuhnian sense [26], the combination of crystalline and amorphous thin films in a single hybrid structure bridges the performance gap of mid-infrared mirrors with regards to their counterparts in the near-infrared and visible ranges.

Still, the significance of substrate-transferred mirrors, both all-crystalline and hybrid crystalline-amorphous, extends beyond their immediate applications. Their potential to advance fields such as environmental sensing, broadband spectroscopy, and laser-based applications is profound. As the technology continues to expand—towards longer wavelengths and better performance—the boundaries of what is possible will undoubtedly evolve, driven by the confluence of innovation, determination, and especially collaborative effort.

While the studies in this thesis represent important milestones, they are points in an ongoing journey. The field of mid-infrared optical coatings stands at the cusp of further innovations, with each innovation driving the next one. As researchers continue to push the boundaries, the future holds promise for even more transformative advancements.

In closing, the work presented in this thesis serves not only as a testament to the latest achievements in the field of mid-infrared optical coatings but also emphasizes the importance of perseverance, collaboration, and a deep-rooted curiosity as a driver for scientific innovation.

References

[1] G. D. Cole, W. Zhang, B. J. Bjork, D. Follman, P. Heu, C. Deutsch, L. Sonderhouse, J. Robinson, C. Franz, A. Alexandrovski, et al., "High-performance near- and mid-infrared crystalline coatings", Optica **3**, 647 (2016).

[2] U. Keller, K. J. Weingarten, F. X. Kärtner, D. Kopf, B. Braun, I. D. Jung, R. Fluck, C. Hönninger, N. Matuschek, and J. Aus der Au, "Semiconductor saturable absorber mirrors (SESAM's) for femtosecond to nanosecond pulse generation in solid-state lasers", IEEE J. Sel. Top. Quantum Electron. **2**, 435 (1996).

[3] U. Keller, "Ultrafast solid-state laser oscillators: A success story for the last 20 years with no end in sight", Appl. Phys. B **100**, 15 (2010).

[4] A. Abramovici, W. E. Althouse, R. W. P. Drever, Y. Gürsel, S. Kawamura, F. J. Raab, D. Shoemaker, L. Sievers, R. E. Spero, K. S. Thorne, et al., "LIGO: The laser interferometer gravitational-wave observatory", Science **256**, 325 (1992).

[5] L. Barsotti, S. Gras, M. Evans, and P. Fritschel, *The updated Advanced LIGO design curve (T1800044-v5)* (LIGO, 2018).

[6] B. J. Bjork, T. Q. Bui, O. H. Heckl, P. B. Changala, B. Spaun, P. Heu, D. Follman, C. Deutsch, G. D. Cole, M. Aspelmeyer, et al., "Direct frequency comb measurement of OD + CO → DOCO kinetics", Science **354**, 444 (2016).

[7] G. Gagliardi and H.-P. Loock, eds., *Cavity-Enhanced Spectroscopy and Sensing*, Vol. 179, Springer Series in Optical Sciences (Springer, Berlin, Heidelberg, 2014).

[8] A. J. Fleisher, D. A. Long, Q. Liu, L. Gameson, and J. T. Hodges, "Optical Measurement of Radiocarbon below Unity Fraction Modern by Linear Absorption Spectroscopy", J. Phys. Chem. Lett. **8**, 4550 (2017).

[9] I. Galli, S. Bartalini, S. Borri, P. Cancio, D. Mazzotti, P. De Natale, and G. Giusfredi, "Molecular Gas Sensing Below Parts Per Trillion: Radiocarbon-Dioxide Optical Detection", Phys. Rev. Lett. **107**, 270802 (2011).

[10] A. D. McCartt, T. J. Ognibene, G. Bench, and K. W. Turteltaub, "Quantifying Carbon-14 for Biology Using Cavity Ring-Down Spectroscopy", Anal. Chem. **88**, 8714 (2016).

[11] I. Galli, S. Bartalini, R. Ballerini, M. Barucci, P. Cancio, M. De Pas, G. Giusfredi, D. Mazzotti, N. Akikusa, and P. De Natale, "Spectroscopic detection of radiocarbon dioxide at parts-per-quadrillion sensitivity", Optica **3**, 385 (2016).

[12] V. Sonnenschein, R. Terabayashi, H. Tomita, S. Kato, N. Hayashi, S. Takeda, L. Jin, M. Yamanaka, N. Nishizawa, A. Sato, et al., "A cavity ring-down spectrometer for study of biomedical radiocarbon-labeled samples", J. Appl. Phys. **124**, 033101 (2018).

[13] M. G. Delli Santi, S. Bartalini, P. Cancio, I. Galli, G. Giusfredi, C. Haraldsson, D. Mazzotti, A. Pesonen, and P. De Natale, "Biogenic Fraction Determination in Fuel Blends by Laser-Based $^{14}CO_2$ Detection", Adv. Photonics Res. **2**, 2000069 (2021).

[14] B. Azadgoli and R. Y. Baker, "Laser applications in surgery", Ann. Transl. Med. **4**, 452 (2016).

[15] B. Umroh, A. Ginting, and M. N. A. Rahman, "CO_2 laser machining on alumina ceramic: a review", IOP Conf. Ser.: Mater. Sci. Eng. **1003**, 012131 (2020).

[16] R. T. Mushtaq, Y. Wang, M. Rehman, A. M. Khan, and M. Mia, "State-of-the-art and trends in CO_2 laser cutting of polymeric materials—a review", Materials **13**, 3839 (2020).

[17] G. D. Cole, D. Follman, P. Heu, G.-W. Truong, C. Deutsch, C. Franz, A. L. Alexandrovski, B. Ma, and X. Cheng, "Laser-induced damage measurements of crystalline coatings (Conference Presentation)", in Laser-Induced Damage in Optical Materials 2018: 50th Anniversary Conference, Vol. 10805, edited by C. W. Carr, G. J. Exarhos, V. E. Gruzdev, D. Ristau, and M. Soileau, Proceedings of SPIE (2018).

[18] G. D. Cole, C. Nguyen, D. Follman, G.-W. Truong, E. Krause, and T. Böhme, "A high-power-handling deformable mirror system employing crystalline coatings", in Laser-Induced Damage in Optical Materials 2022, Vol. 12300, edited by C. W. Carr, D. Ristau, and C. S. Menoni, Proceedings of SPIE (2022), p. 123000D.

[19] C.-F. Lin and B.-L. Lee, "Extremely broadband AlGaAs/GaAs superluminescent diodes", Appl. Phys. Lett. **71**, 1598 (1997).

[20] C. Sirtori, P. Kruck, S. Barbieri, P. Collot, J. Nagle, M. Beck, J. Faist, and U. Oesterle, "GaAs/Al_xGa_{1-x}As quantum cascade lasers", Appl. Phys. Lett. **73**, 3486 (1998).

[21] V. Pervak, S. Naumov, F. Krausz, and A. Apolonski, "Chirped mirrors with low dispersion ripple", Opt. Express **15**, 13768 (2007).

[22] S. Diddams and J.-C. Diels, "Dispersion measurements with white-light interferometry", J. Opt. Soc. Am. B **13**, 1120 (1996).

[23] T. V. Amotchkina, A. V. Tikhonravov, M. K. Trubetskov, D. Grupe, A. Apolonski, and V. Pervak, "Measurement of group delay of dispersive mirrors with white-light interferometer", Appl. Opt. **48**, 949 (2009).

[24] K. Naganuma, K. Mogi, and H. Yamada, "Group-delay measurement using the Fourier transform of an interferometric cross correlation generated by white light", Opt. Lett. **15**, 393 (1990).

[25] L. Fleck, *Entstehung und Entwicklung einer wissenschaftlichen Tatsache. Einführung in die Lehre vom Denkstil und Denkkollektiv*, 9th ed., Suhrkamp Taschenbuch Wissenschaft 312 (Suhrkamp, Frankfurt am Main, 2012).

[26] T. S. Kuhn, *The structure of scientific revolutions*, 4th ed. (University of Chicago Press, Chicago, 2012).

Abstract

This cumulative doctoral thesis presents a comprehensive investigation into the development, characterization, and application of substrate-transferred crystalline Bragg mirrors based on gallium arsenide (GaAs) and aluminum gallium arsenide (AlGaAs), specifically tailored for the mid-infrared spectral region. We develop and characterize the first highly reflective substrate-transferred crystalline mirrors with a center wavelength above 4 µm. These coatings achieve an excess optical loss (absorption and scatter $A + S$) of 7 parts per million (ppm) and a per-mirror transmittance T of 144 ppm at a center wavelength of 4.54 µm. The study also identifies a unique polarization-orientation-dependent loss mechanism, attributed to the elastic anisotropy of strained epitaxial multilayers. We also give a thorough description of the devices and methodology used for the characterization of these mirrors. Furthermore, we provide a general, innovative, and highly adaptable approach to measuring the refractive indices of two materials simultaneously by probing a thin film heterostructure. Using this methodology, we measure the refractive indices of GaAs and AlGaAs over a broad spectral range from 2.0 µm to 7.1 µm. Utilizing a combination of Fourier-transform infrared spectrometry and scanning electron microscopy, this methodology conclusively yields refractive index values with propagated relative uncertainties on the order of 10^{-4}. These updated values are crucial for the design, fabrication, and characterization of next-generation active and passive optical devices, including substrate-transferred crystalline mirrors. Finally, we report on another milestone in the development of mid-infrared supermirrors. On the one hand, we demonstrate all-crystalline GaAs/AlGaAs-based Bragg mirrors with a center wavelength of 4.45 µm, capable of achieving finesse values of 231 000 (corresponding to $T = 9.33$ ppm and $A + S = 4.27$ ppm) in a two-mirror optical cavity. On the other hand, we introduce the concept of crystalline-amorphous hybrid mirrors, combining an ion-beam-sputtered base multilayer with a substrate-transferred crystalline heterostructure. These hybrid mirrors achieve a two-mirror cavity finesse of 409 000 at 4.45 µm ($T = 2.53$ ppm, $A + S = 5.17$ ppm). We also describe the methods used to demonstrate these results. Both technologies unlock a wide array of mid-infrared applications, including environmental sciences, detection of fugitive emissions, and breath-gas analysis, as demonstrated in a proof-of-principle spectroscopic measurement conducted as part of this study.

Kurzfassung

Diese kumulative Dissertation stellt eine umfassende Untersuchung der Entwicklung, Charakterisierung und Anwendung von substratübertragenen kristallinen Bragg-Spiegeln auf der Basis von Galliumarsenid (GaAs) und Aluminiumgalliumarsenid (AlGaAs) vor, die speziell für den mittleren Infrarot-Spektralbereich entwickelt wurden. Wir entwickeln und charakterisieren die ersten hochreflektierenden substrat-transferierten kristallinen Spiegel mit einer Zentralwellenlänge oberhalb von 4 µm. Diese Coatings erreichen einen optischen Verlust (Absorption und Streuung $A + S$) von 7 Parts per million (ppm) und eine Transmission T pro Spiegel von 144 ppm bei einer Zentralwellenlänge von 4.54 µm. Die Studie identifiziert auch einen einzigartigen, von der Polarisationsorientierung abhängigen Verlustmechanismus, der auf die elastische Anisotropie von verspannten epitaktischen Multischichten zurückzuführen ist. Wir geben auch eine gründliche Beschreibung der Geräte und der Methodik, die für die Charakterisierung dieser Spiegel verwendet wurden. Darüber hinaus beschreiben wir einen allgemeinen, innovativen und äußerst anpassungsfähigen Ansatz zur gleichzeitigen Messung der Brechungsindizes von zwei Materialien durch die Untersuchung einer Dünnschicht-Heterostruktur. Mit dieser Methode messen wir die Brechungsindizes von GaAs und AlGaAs über einen breiten Spektralbereich von 2.0 µm bis 7.1 µm. Durch eine Kombination von Fourier-Transform-Infrarotspektrometrie und Rasterelektronenmikroskopie liefert diese Methode schlüssig Brechungsindexwerte mit relativen Unsicherheiten in der Größenordnung von 10^{-4}. Diese aktualisierten Werte sind von entscheidender Bedeutung für das Design, die Herstellung und die Charakterisierung von zukünftigen aktiven und passiven optischen Geräten, einschließlich substrat-transferierter kristalliner Spiegel. Schließlich berichten wir über einen weiteren Meilenstein in der Entwicklung von Superspiegeln im mittleren Infrarotbereich. Zum einen demonstrieren wir komplett kristalline GaAs/AlGaAs-basierte Bragg-Spiegel mit einer Zentralwellenlänge von 4.45 µm, die in der Lage sind, Finesse-Werte von 231 000 (entsprechend $T = 9.33$ ppm und $A + S = 4.27$ ppm) in einem optischen Resonator mit zwei Spiegeln zu erreichen. Zum anderen stellen wir das Konzept der kristallin-amorphen Hybridspiegel vor, die einen ionenstrahlgesputterte Basis-Multilayer mit einer substratübertragenen kristallinen Heterostruktur kombinieren. Diese Hybridspiegel erreichen eine Finesse von 409 000 bei 4.45 µm ($T = 2.53$ ppm, $A + S = 5.17$ ppm) in einem Zwei-Spiegel-Resonator. Wir beschreiben auch die Methoden, die zur Demonstration dieser Ergebnisse verwendet werden. Wie eine im Rahmen dieser Studie durchgeführte spektroskopische Proof-Of-Principle-Messung gezeigt hat, eröffnen beide Technologien eine breite Palette von Anwendungen im mittleren Infrarotbereich, einschließlich Umweltwissenschaften, Erkennung von flüchtigen Emissionen und Atemgasanalyse.